NACA

RESEARCH MEMORANDUM

AN EXPERIMENTAL STUDY OF FIVE ANNULAR AIR INLET CONFIGURATIONS AT SUBSONIC AND TRANSONIC SPEEDS

By Robert E. Pendley, Joseph R. Milillo,
Frank F. Fleming, and Carroll R. Bryan

Langley Aeronautical Laboratory
Langley Field, Va.

NATIONAL ADVISORY COMMITTEE
FOR AERONAUTICS

WASHINGTON

August 19, 1953

[redacted]

[redacted]

NATIONAL ADVISORY COMMITTEE FOR AERONAUTICS

RESEARCH MEMORANDUM

AN EXPERIMENTAL STUDY OF FIVE ANNULAR AIR INLET CONFIGURATIONS AT SUBSONIC AND TRANSONIC SPEEDS

By Robert E. Pendley, Joseph R. Milillo,
Frank F. Fleming, and Carroll R. Bryan

SUMMARY

An investigation of an NACA 1-80-100 nose inlet fitted alternately with an elliptical, a parabolic, a 14°-conical, and a 22°-conical central body was conducted at subsonic and transonic speeds in the Langley 8-foot transonic tunnel. Drag, surface-pressure, and pressure-recovery measurements were obtained at an angle of attack of 0° through a Mach number range of 0.6 to 1.1. Surface-pressure and pressure-recovery measurements were made at angles of attack of 4°, 7°, and 10°. The pressure-recovery measurements were made after the entering flow had passed through a short, rapidly diverging diffuser. Additional measurements were made of the drag of an NACA 1-80-300 nose inlet fitted with the elliptical central body at an angle of attack of 0° for a Mach number of 1.1.

Test results indicated that, although there was very little effect of central-body profile on the external drag at subsonic Mach numbers, prominent effects were observed above a Mach number of 1.0. At the higher values of the ratio of the entering stream-tube area to the body frontal area, the minimum external drag of the NACA 1-80-300 nose-inlet-central-body combination was as low as the minimum drag measured to date for an NACA 1-series open-nose inlet. There was considerable effect of central-body profile on the pressure recovery of the inlet, with the conical-central-body configurations having decidedly better pressure-recovery characteristics. The pressure recovery of these configurations was also relatively insensitive to changes in angle of attack, whereas the curved-central-body configurations showed significant losses in pressure recovery due to angle of attack in the mass-flow-ratio range of practical interest. Changes in angle of attack generally caused only small changes in the maximum mass-flow ratio. Reductions in external drag, obtained by utilizing the configurations with lower pressures over the central-body

[redacted]

[redacted]

surface, were accompanied by resultant losses in pressure recovery. The sensitivity of the propulsive thrust to changes in central-body shape was therefore reduced.

INTRODUCTION

Transonic air-inlet research programs have so far been largely directed toward the investigation of the effects of those design parameters adjudged to be of primary importance. The effects of large changes in the lip proportions of nose inlets utilizing the NACA 1-series profile (ref. 1) are indicated by an aggregation of several papers (refs. 2 to 8) which describe investigations at subsonic and transonic Mach numbers. Two papers have been published which treat briefly of the effects of inlet profile on subsonic and transonic nose-inlet performance (refs. 9 and 10). The investigations reported in references 1 to 10 show that both inlet proportions and inlet profile are important factors to be considered in the design of transonic aircraft.

An air-inlet research program utilizing 8-inch-diameter models at subsonic and transonic speeds is underway in the Langley 8-foot transonic tunnel. This program includes a family of NACA 1-series nose inlets of proportions which extend beyond the range of those which have been previously investigated. The study of the first three nose inlets of the program is reported in reference 6. Included in this program are several annular-inlet configurations comprised of central bodies installed in NACA 1-series nose inlets of relatively large inlet diameter. Drag, loads data in the form of surface-pressure distributions, and pressure-recovery characteristics of four of these annular-inlet configurations have been investigated at subsonic and transonic speeds, and the drag of a fifth annular inlet has been measured at a Mach number of 1.1. The purpose of this paper is to present an analysis of the results obtained in this investigation and to compare the annular-inlet characteristics with those observed for the nose inlets previously studied.

The configurations investigated may be of interest in those designs where the installation of equipment ahead of the inlet ducting is desired and, although the central bodies were relatively large, in the design of propeller spinners. The results will be of interest also to the designer of fuselage-side air inlets, since the flow over the central bodies tends to simulate the flow over the fuselage nose.

The four configurations for which pressure-recovery data were obtained consisted of four different central-body shapes fitted alternately to a common ducted body. The entering flow passed through a short, rapidly diverging diffuser such as might be considered in cases where it is desirable to minimize the longitudinal dimensions of the engine ducting.

The rate of the diffuser-area growth was variable and increased with distance in the flow direction. The over-all equivalent conical angle of the diffuser was 22.5°, a value which would lead one to expect separation at some point in the diffuser throughout the useful mass-flow range.

Drag, surface-pressure, and pressure-recovery measurements were made at an angle of attack of 0°, and surface-pressure and pressure-recovery measurements were made at the additional angles of attack of 4°, 7°, and 10°. The test Mach number range extended from approximately 0.6 to 1.1, whereas the test Reynolds number range, based on maximum diameter, extended from 2.3×10^6 to 2.7×10^6.

SYMBOLS

A	duct or stream-tube cross-sectional area
B	base area, sting fairing
C	mass-flow coefficient, $\frac{m}{\rho_o V_o F}$
C_D	drag coefficient, based on area F
C_{D_a}	additive drag coefficient
C_{D_f}	skin-friction drag coefficient
C_{D_t}	total drag coefficient, $\frac{G_a}{q_o F} + P_B \frac{B}{F}$
C_{D_e}	external drag coefficient, $C_{D_t} + C_{F_n}$
C_{D_p}	pressure drag coefficient
C_{F_n}	net-thrust coefficient (internal drag coefficient when negative), $\frac{1}{q_o F}\left[\left(V_3 - V_o\right)m + \left(p_3 - p_o\right)A_3\right]$
d	diameter
D	maximum body diameter (8.000 inches)

[redacted]

F	maximum body cross-sectional area
G_a	axial force indicated by strain gage
H	total pressure
$\overline{H}$	average total pressure, area weighted, $\int H \frac{dA}{A}$
m	internal mass-flow rate
m/m_o	mass-flow ratio, $\frac{m}{\rho_o V_o A_1} = \frac{A_o}{A_1}$
m/m_s	relative mass-flow ratio, $\frac{m}{\rho_{sonic} V_{sonic} A_1} = \frac{A_o}{A_1} \frac{A_{sonic}}{A_o}$
M	Mach number
p	static pressure
P	static-pressure coefficient, $\frac{p - p_o}{q_o}$
q	dynamic pressure, $\rho V^2/2$
r	radius
R	body maximum radius, $\frac{D}{2}$
V	velocity
x	axial distance, positive downstream
α	angle of attack
θ	angular position measured from top of annulus, positive counterclockwise looking downstream.
ρ	air density

Subscripts:

o	free-stream station
1	minimum-area station just inside inlet lip
2	pressure-recovery measuring station
3	duct-exit station

K stagnation point at inlet lip

B sting-fairing base

c central body

d downstream of shock

u upstream of shock

l inner lip surface between stagnation point on inlet lip and minimum area station

f external surface of entering stream tube and external model surface between inlet-lip stagnation point and maximum-diameter station

s external model surface between inlet-lip stagnation point and maximum-diameter station

sonic condition corresponding to local Mach number of 1 for isentropic flow

APPARATUS AND TESTS

Tunnel.- The investigation was conducted in the Langley 8-foot transonic tunnel utilizing a 1/9-open slotted test section. The geometry and aerodynamic properties of this test section are described in references 11 and 12. Figure 1 is a drawing of the model support system used in this investigation and in the prior investigation reported in reference 6.

Models.- A drawing of the five annular-inlet configurations studied is presented in figure 2. A photograph of some of the components of these configurations is given as figure 3. The two 8-inch-diameter nose inlets used in this investigation were the NACA 1-80-100, which was fitted alternately with four interchangeable 4.7-inch-diameter central bodies (an elliptical, a parabolic, a 14°-conical, and a 22°-conical) and the NACA 1-80-300, which was fitted with the elliptical central body.

In the design of the conical central bodies, the curved region of transition between the conical surface and the surface of zero slope was fixed inside the inlet lip so that the pressure on this portion of the central body would tend to be fixed by the mass-flow ratio. The presence of such a region of curvature ahead of the inlet was avoided because of the possibility of the detrimental effect of a pressure peak. The

[redacted]

variation of the duct cross-sectional area between the inlet and the pressure-recovery survey station is presented in figure 4, which includes for comparison the area variation of a 22.5° cone.

Nondimensional coordinates for the outer profile of the inlets appear in reference 1. The design of the internal lip shapes is specified as a function of the inlet proportions by an arbitrary equation stated in reference 6. Coordinates of the inner lip fairing and the elliptical and parabolic central bodies are presented in tables I and II, respectively. The surface contours of the conical central bodies are completely defined by figure 2. Ordinates for the afterbody are given in reference 13. The nose inlets (that is, the cowlings forward of the maximum-diameter station) were of spun-aluminum construction and were designed to be easily interchangeable on a common afterbody similarly constructed.

Instrumentation.- Each nose inlet was provided with a row of surface-pressure orifices which extended the entire length of the inlet along the center line of the upper surface. Orifices were also located on both the upper and the lower inner lips of the inlets, on the upper and the lower surfaces of the central bodies, and along the upper surface of the afterbody.

The afterbody assembly, which was used in the investigations of references 6 and 13, was attached to the sting through a flexure-type three-component strain-gage balance. The pressure recovery of the internal flow was surveyed by six rakes of total- and static-pressure tubes located near the maximum-diameter station. The internal flow was also surveyed at the exit annulus by a sting-supported cruciform rake. The entire instrumentation system is more completely described in reference 6.

Tests.- Drag data for the 1-80-100 configurations were obtained at zero angle of attack through a Mach number range extending from about 0.6 to 1.1. Drag measurements were not made at angles of attack other than zero because of erratic interference between the pressure leads and the sting. Pressure-recovery measurements were made for the same Mach number range at angles of attack of 0°, 4°, 7°, and 10°. The only data obtained with the 1-80-300 configuration were external drag data at a Mach number of 1.1. The procedure during tests consisted of holding the angle of attack and stream Mach number constant and recording data at various mass-flow ratios.

At angle of attack of 0°, drag data from the strain gage were manually recorded and all pressure readings were recorded simultaneously on film from a multitube manometer board. The angle of attack of the model was set and checked during runs by means of a cathetometer.

The Reynolds number of the tests ranged from approximately 2.3×10^6 to 2.7×10^6, based on the maximum diameter.

METHODS

External drag coefficient.- The external drag is defined in this paper, as in reference 6, as the total drag (strain-gage reading corrected for the sting-fairing force) minus the internal drag:

$$C_{D_e} = \frac{G_a}{q_o F} + P_B \frac{B}{F} + C_{F_n}$$

The physical meaning of this definition of external drag for open-nose inlets was shown in reference 6 to be equal to the friction drag and the gage-pressure force acting on the external surface of the entering stream tube (the additive drag) and on the external body surface. It can be similarly shown that the external drag defined as above becomes in the case of the annular inlet the friction force and the gage-pressure force acting on the external surface of the entering stream tube and on the external surface between the stagnation point at the inlet lip and the exit. Thus,

$$C_{D_e} = \int_K^3 P \, d\left(\frac{r}{R}\right)^2 + C_{D_{f_{K-3}}} + C_{D_a}$$

The friction force on the external surface of the entering stream tube is negligible.

Additive drag.- A trial calculation showed that the flow at the inlet station of the annular inlets precluded the assumption of one-dimensional isentropic flow between the free stream and station 1 in the calculation of the additive drag. The additive drag was therefore estimated from the measured static pressure on the inner and outer duct surfaces at station 1, from graphical integration of the pressure distributions on the central body and the inner lip surface between the stagnation point and station 1, and with an assumed total-pressure distribution at the inlet. The maximum ordinate of the assumed total-pressure profiles was fixed equal to free-stream total pressure, and the construction of the shape of the profile was guided by reference to the shape of the one-seventh-power velocity distribution. The resulting profiles appeared to be reasonable ones since the mass-flow ratios calculated from these profiles agreed well with those calculated from the exit-rake data. This method of estimating the additive drag is expected to be less useful for conditions of asymmetric or separated flow at the inlet.

[redacted]

By writing the momentum equation between the free-stream and inlet stations, the additive drag coefficient was calculated as

$$C_{D_a} = 2\int_{\text{Annulus}} \frac{\rho_1 V_1}{\rho_o V_o}\left(\frac{V_1}{V_o} - 1\right) d\left(\frac{r_1}{R}\right)^2 + \int_{\text{Annulus}} P_1\, d\left(\frac{r_1}{R}\right)^2 +$$

$$\int_1^K P\, d\left(\frac{r}{R}\right)^2 + \int_{\text{Central body}} P\, d\left(\frac{r}{R}\right)^2$$

In calculating the force on the central body and inner lip, friction forces were neglected.

Other variables.- The pressure drag coefficient of any specified body was obtained by graphically integrating the measured pressure distributions:

$$C_{D_p} = \int P\, d\left(\frac{r}{R}\right)^2$$

The pressure recovery was calculated by numerically integrating the pressure-recovery-rake data:

$$\frac{\bar{H}}{H_o} = \frac{1}{A_2}\int \frac{H_2}{H_o}\, dA_2$$

The mass-flow ratio was obtained from numerical integration of the exit rake data.

PRECISION

With the exception of the method of calculating the additive drag coefficient, the measurements and calculations of the present investigations were subject to the same type of errors which were present in reference 6. The maximum probable errors in the measurements and calculations are estimated as follows:

Free-stream Mach number	±0.003
Mass-flow ratio:	
Low mass-flow ratio - low Mach number	±0.06
High mass-flow ratio	±0.03
Pressure-drag coefficient	±0.015
External drag coefficient	±0.01
Integrated pressure-recovery ratio	±0.01

Because of the shorter length of the NACA 1-80-100 annular-inlet configurations, these inlets occupied a region in the test section which had smaller variations in the tunnel-empty Mach number distribution. The maximum variation in this distribution in the test-section region occupied by these inlets is 0.009.

RESULTS AND DISCUSSION

Tunnel Boundary Interference

Tests reported in reference 13 showed that, in the Langley 8-foot transonic tunnel, there was no important tunnel-boundary interference at subsonic Mach numbers on a 66-inch-long body of revolution of maximum diameter equal to that of the inlets of the present investigation. A qualitative indication of the magnitude of the differences in the subsonic tunnel interference acting on the inlets tested and on the solid body of reference 13 was established by a study of tunnel-wall Mach number distributions.

A comparison of the distributions obtained during the present tests with those of reference 13 showed that the magnitude of model-induced disturbances at the wall were, for the inlet configurations, equal to or less than those of the solid body at Mach numbers of about 0.95 and below. At a Mach number of about 1.0, the irregularities in the tunnel-wall Mach number distribution caused by the inlet configurations were only slightly greater than those caused by the solid body. It therefore seems reasonable to assume, as was assumed in the case of the nose inlets of reference 6 that there was no large subsonic tunnel-boundary interference acting on the inlets.

It is believed that there was no important effect of boundary interference on pressure recovery throughout the Mach number range, since, at most supersonic Mach numbers, the reflected bow shock struck the model downstream of the inlet plane, and at lower speeds the shock is believed to have been so weak as to cause negligible interference on the central-body flow.

[redacted]

As discussed in reference 13 and as shown by the surface-pressure distributions of figures 5 to 12, reflected compression and expansion waves were expected to have introduced appreciable interference in the drag measurements at supersonic speeds. Where this interference may have been present, the drag curves were faired with dashed lines. The presentation of interference-subject drag data in the figures is considered desirable, since the interference is not expected to have affected to an important degree the variation of drag coefficient with mass-flow ratio; furthermore, the interference is not expected to have precluded an indication of the effects of inlet configuration on the external drag.

Surface-Pressure Distribution

Mach number effects.- Surface-pressure distributions over the inlet configurations at zero angle of attack are shown in figures 5 to 12. These pressure distributions indicate the formation of a region of supersonic flow at low mass-flow ratios over a portion of the body for all test speeds higher than a Mach number of 0.6. These regions of supersonic flow, which originated at or immediately behind the inlet lip, became more extensive with increasing stream Mach number and, at a Mach number of 0.95, were terminated by a rapid compression to subsonic velocities immediately behind the body maximum-diameter station (figs. 6, 8, 10, and 12). It will be shown later that this Mach number corresponds to the inception of the drag rise of these inlets. At Mach numbers of about 1.0 and 1.02, the compression to subsonic velocities tended to be more gradual.

In the test Mach number range extending from about 0.90 to 1.05, there were a number of instances where a reduction in mass-flow ratio caused a pressure increase over a region of the external surface between those regions at the inlet lip and exit where the pressures were reduced (see, for example, figs. 8(c), to 8(g)). In some of these instances (for example, figs. 8(c) or 8(d)), the resultant crossover of the curves would be expected from the higher compression which would result from the higher local supersonic velocities generated at the inlet lip at low mass-flow ratios. In other instances, however (for example, figs. 6(h) or 8(f)), this explanation does not seem to apply, and the possibility of tunnel boundary interference was considered. A study of the tunnel-wall Mach number distributions, however, failed to provide an explanation of this phenomenon.

At a Mach number of 1.1, the flow over the entire body was supersonic downstream from the lip stagnation region for all four configurations.

Attitude of flow at inlet lip.- A primary factor affecting the static-pressure distributions on the external surface between the inlet lip and the maximum-diameter station is the angle of the flow approaching the

inlet lip. This angle is increased by reducing the mass-flow ratio or by increasing the slope of the central-body surface in the region of the inlet plane. Where this angle was low, for instance at high mass-flow ratios with the curved central bodies (figs. 5 and 7), the pressure distribution was fairly uniform. As this angle was increased, low-pressure peaks followed by rapid compressions appeared in the immediate region of the inlet lip (figs. 5(a), 5(b), 7(a), and 7(b)). These peaks became more pronounced as the incidence angle was increased until, at very low mass-flow ratios for the conical central bodies, the regions of low pressure changed character and became more extensive (figs. 9 and 11) so that the possibility of boundary-layer separation from the external surface was indicated (ref. 5). This change in the shape of the pressure peak did not occur at the two lowest test Mach numbers for the elliptical and parabolic central bodies. It is suspected that the sharply localized low-pressure regions having rounded peaks were due to a type of "bubble" separation (figs. 9(a) and 9(b)). This type of separation is generally followed by immediate reattachment (ref. 14). In the absence of external flow separation, the effects of mass-flow ratio variation on the external-surface pressure distribution forward of the maximum-diameter station were limited to the region at or immediately behind the inlet lip $(\frac{X}{D} \approx 0)$.

The pressure distributions of figures 5 to 12 show, in general, that the difference in the shape of the elliptical and parabolic central bodies did not effect large changes in the external flow, but the much higher slopes of the surfaces of the two conical central bodies induced considerable change. At the lower test Mach numbers (figs. 11(a) and 11(b)), the 22°-conical central body induced a sharp pressure peak even at the highest test mass-flow ratio.

Mass-flow-ratio effects on the pressures near the jet were presumably a result of variations in the jet-tube area that caused a variation in the turning around the model trailing edge.

Central-body pressure distributions.- In general, the pressures obtained on the cones forward of the inlet plane were much higher than those obtained on the curved bodies. The lower pressures on the elliptical and parabolic central bodies were a result of the curvature of these bodies. As the mass-flow ratio was reduced, the pressure rise acting on the entering boundary layer steepened and finally caused separation from the cental body surface ahead of the inlet. At the lowest test mass-flow ratios, the presence of this separation is shown by the prominent increase in the extent of the central body surface under appreciable influence of the mass-flow ratio, by the general increase of the pressure level on the central body, and by the indication of little or no pressure rise in the diffuser (for example, figs. 9(c) and 9(d)).

[redacted]

Effects of angle of attack on pressure distribution.- Surface-pressure distributions over the models forward of the body maximum diameter are presented for two angles of attack and for Mach numbers of 0.6 and 1.10 in figures 13 to 16. Because of the limited number of pressure orifices on the models, only limited indications of the nature of the flow about the inlets at angle of attack are available.

In general, the effect of angle of attack on the flow over the forward portion of the central bodies was to increase the velocities on the upper surface and to reduce the velocities on the lower surface. Near the inlet station, the converse was true and, at the higher mass-flow ratios, the pressures on the top and bottom of the central bodies were quite different, with more flow passing into the bottom of the inlet.

At angles of attack and at high mass-flow ratios, the internal flow performance of an inlet is susceptible to losses originating at the inside of the bottom lip. Among the four central bodies tested, the surface slopes of the elliptical and parabolic central bodies in the region of the inlet were the least favorable in this respect. At the high mass-flow ratios, $M_o \approx 0.6$, figures 13(b) and 14(b) show that sharp pressure peaks were induced on the inner surface of the lower lip at an angle of attack of 10°. At the maximum test Mach number $(M_o \approx 1.1)$ (figs. 13(a) and 14(a)), sonic velocity was exceeded by an appreciable margin on this surface at the high mass-flow-ratio angle-of-attack condition.

Increases in angle of attack caused the velocities over the external surface of the upper inlet lip to be greater and increased the tendency toward separation of the external flow at that point.

External Drag

Effect of mass-flow ratio.- The drag data obtained for the NACA 1-80-100 nose-inlet central-body combinations are presented in figures 17 to 20. The minimum drag of any inlet at any particular Mach number occurred at the maximum mass-flow ratio. Reference to the pressure distributions (figs. 5, 7, 9, and 11) indicates that the inlets were choked at the maximum mass-flow ratios for Mach numbers above 0.8 for the elliptical and parabolic central bodies, and above 0.9 for the two conical central bodies. Although inlet choked data were not obtained at these lower test Mach numbers, it can be seen from the slope of the drag curves (figs. 17 to 20) that little change in drag would result upon extending the curves to the choking values of mass-flow ratio.

As stated in the section entitled "Methods," the external drag is the sum of the additive drag and the viscous and gage-pressure forces acting on the external surface between the inlet lip and the jet. Since

the additive drag coefficient would be expected to increase rapidly with reductions in mass-flow ratio from the choking value, the moderate slope of the external-drag curve indicates that a large part of the compensating effect of lowered pressures on the external lip surface was obtained. The pressure distributions of figures 5, 7, 9, and 11 show the successive reductions in lip pressures which accompanied mass-flow decreases.

Effects of Mach number and central-body profile.- The effect of increasing the Mach number from 0.6 to 1.1 was to increase the slope of the curves of drag against m/m_o and, at these Mach number limits, the slopes were lowest for the inlet with the elliptical central body and were consecutively higher for the parabolic, 14°-conical, and 22°-conical central bodies.

The Mach number effect on the external drag coefficients for the four NACA 1-80-100 inlet configurations is presented in figure 21 for the maximum mass-flow case. As previously stated, the maximum mass-flow ratios corresponded to the choked case except at the lower Mach numbers, but no appreciable change in the curves of figure 21 would be expected upon increasing the mass-flow ratios for the unchoked cases to the choking values. At subsonic Mach numbers, there were only small differences in the external-drag coefficients of the inlet configurations. The subsonic drag of the inlet with the 22°-conical central body was consistently higher by a small amount than that of the other three inlets, but the subsonic-drag rises were very similar for all four inlets. When comparison of the inlet drags is made with the drag of the solid body of reference 13, it appears that the lesser wetted area of the inlets resulted in a lesser drag at Mach numbers below the drag rise. The drag rise of the inlets was larger, however. This result would be expected from an application of the basic idea of the transonic drag-rise rule of reference 15. This rule states that the transonic drag rise of a configuration is determined principally by the shape of the longitudinal variation of the total cross-sectional area. If, for the inlet bodies, the developments of the cross-sectional areas of the entering stream-tube surfaces and the external body surfaces (actual cross-sectional area less A_o) are reduced to equivalent solid bodies, it will be seen that the fineness ratios of these equivalent bodies are much lower than that of the solid body.

At the supersonic Mach numbers, appreciable effects of central-body shape were observed. The drag of the solid body was lower than that of the four inlets at the highest test Mach number, and the inlets with the central bodies of curved profile had substantially less drag than those with the conical profiles.

As previously explained, the external-drag data at the highest test Mach number was subject to some tunnel boundary interference acting on the afterbody. The belief that this interference should not invalidate comparison of the external-drag data is substantiated by calculation for

the inlet-choked condition of the pressure drag on the external surface of the entering stream tube (additive drag) and on the external surface between the lip stagnation point and the maximum-diameter station. This drag, denoted $\left(C_{D_p}\right)_f$ in coefficient form, was free of interference at $M_o \approx 1.1$, and is tabulated as follows:

Type of central body	M_o	C_{D_a}	$\left(C_{D_p}\right)_s$	$\left(C_{D_p}\right)_f$
Ellipse	1.108	0.0698	0.0236	0.0934
Parabola	1.107	.0860	.0328	.1188
14° cone	1.104	.1635	-.0192	.1443
22° cone	1.105	.2199	-.0316	.1883

Although the pressure drag coefficients $\left(C_{D_p}\right)_f$ were calculated with an assumed inlet total-pressure profile, these coefficients indicate approximately the same drag relationships for the four inlets as were indicated by the force measurements.

Since the additive drag is a part of the external drag

$$C_{D_e} = C_{D_a} + \int_K^3 P \, d\left(\frac{r}{R}\right)^2 + C_{D_{f_{K-3}}}$$

and since the force on the central-body affects the additive drag

$$C_{D_a} = 2C\left(\frac{V_1}{V_o} - 1\right) + P_1 \frac{A_1}{F} + C_{D_l} + C_{D_c}$$

the external-drag differences for a given mass-flow ratio can be expected to have originated in differences in the drag forces on the central bodies. These drag differences were not entirely compensated for at the higher Mach numbers by changes in the drag force on the external inlet surface. (For example, the figures in the table above show that only 37 percent of the additive-drag difference between the 22° conical and the elliptical configuration was compensated for by the reduction in the pressure drag on the external surface.) The pressure drag of the central bodies

is presented in figures 22 and 23, and the comparison at the maximum mass-flow rates (fig. 23) accordingly shows a substantial range of central-body drag force for the four central bodies at subsonic Mach numbers which increased markedly at the highest Mach numbers.

Comparison of annular and open-nose inlets.- The selection of an air-inlet configuration often involves the fitting of a forebody shape to an afterbody of predetermined profile. Since large changes in the shape of the forebody can be expected to induce only minor changes in the drag of afterbodies of low curvature (typical of the fuselage shapes of high-speed aircraft), the evaluation of an inlet design from the drag viewpoint can be made by a study of the drag $\left(C_{D_p}\right)_f$. As previously explained, $\left(C_{D_p}\right)_f$ is the additive drag plus the drag acting on the external surface between the stagnation point at the inlet lip and the maximum-ordinate station. If a given engine is considered and the maximum body diameter is specified, the free-stream tube area required for any particular flight condition can be calculated independently of the inlet configuration, if the effect of the pressure recovery on the air flow is neglected. The comparison of the drag of an annular and an open-nose-type inlet for a fixed m/m_o near the choking value can therefore be established essentially by reference to the force acting on streamline AKC for the annular inlet, and on streamline AK'C for the open-nose inlet (fig. 24). For the design conditions specified above, the choice between the two types of inlet consists of accepting with the annular inlet an increased stream-tube projected area in return for a reduction in the projected area of the external surface.

The result of this compromise is presented in figure 25 for the highest test Mach number. Since the free-stream tube area A_o is fixed for a given flight condition, the external drag curves are presented as a function of the mass-flow coefficient $\frac{m}{\rho_o V_o F} = A_o/F$. All the external-drag data in figure 25(a) were obtained with some tunnel boundary interference present in the form of the reflection of the bow shock to the afterbody surface (see figs. 6, 8, 10, and 12). The forebodies, however, were entirely free of tunnel interference so that comparisons of the curves in figure 25(a) can be invalidated only by differences in the interference on the afterbody which are associated with changes in the position and strength of the reflected bow shock. The pressure drag of the afterbody is shown for all cases, except that of the NACA 1-80-300 with elliptical central body, in figure 25(b). Since this drag was always small, and since mass-flow ratio and forebody-shape changes resulted in only small changes in the afterbody pressure drag, the differences in the external drag coefficients (fig. 25(a)) may be assumed to have

[redacted]

originated almost entirely on the forebody. The maximum value of A_o/F for each inlet corresponds to the choked condition.

The annular inlets tended toward larger drag increments with mass-flow reductions. At the higher stream-tube-area ratios, it appears that the drag of the annular inlet can be competitive with that of the open-nose inlet. In fact, the reduction of the curvature of the external surface which was achieved by replacing the NACA 1-80-100 inlet by the NACA 1-80-300 yielded a minimum drag coefficient as low as the minimum achieved by the open-nose inlets (the NACA 1-40-400). The minimum drag coefficient attained (approximately 0.18) may actually represent a value near the minimum which can be attained by the NACA 1-series profile with fineness ratios within the range of those involved here. This possibility is indicated by the fact that the minimum drag-coefficient value is equal to the drag of the well-shaped solid body of reference 13, and also by trends of the NACA 1-series transonic nose-inlet data (fig. 26.) so far available. In fig. 26(a) the transonic rise of the drag coefficient $\left(C_{D_p}\right)_f$ for five open-nose inlets as measured from the subsonic drag level is presented. The data are obtained from several sources (refs. 3, 4, and 6) and in some cases involved extrapolation. Figure 26(b) was obtained by plotting the drag-rise increments shown in figure 26(a) for a Mach number of 1.1. Although the simple parameter X/Y may not necessarily generalize inlet characteristics accurately for extreme proportions, the data so far obtained appear to establish a uniform trend. A large range of drag rise is indicated for the range of proportions shown, and there would appear to be little opportunity for improving the drag by increasing the ratio X/Y beyond that of the NACA 1-40-400 nose inlet. The indication of diminishing returns with increases of X/Y above 8 is in agreement with the two points plotted on figure 26(b) for the NACA 1-80-100 and 1-80-300 annular inlets fitted with the elliptical central body. These two points were obtained from the force measurements and, therefore, include the afterbody drag rise.

Pressure Recovery

Zero-angle-of-attack condition.- The pressure-recovery characteristics of the four NACA 1-80-100 inlet configurations at an angle of attack of 0° are presented in figure 27 as a function of the relative mass-flow ratio for four Mach numbers. The pressure-recovery data presented in this paper were obtained with a diffuser of such a rapid area growth that flow separation was probably always present. Such diffusers are sometimes required in practical ducting systems, and, although the present data are not directly applicable to other diffusers, these data should indicate the relative order of merit of the four central-body shapes for the case of a diffuser of a more favorable expansion rate.

At the maximum values of relative mass-flow ratio, the configurations experienced the pressure-recovery losses characteristically associated with the inlet-choked condition. As the relative mass-flow ratios were reduced from the values for peak total-pressure ratios, the pressure recovery of the curved bodies at the subsonic Mach numbers was decreased because of boundary-layer separation ahead of the inlet. The conical-central-body configurations showed less tendency towards poor pressure recovery at the lower relative mass-flow ratios than did the parabolic- and elliptical-central-body configurations. Because of the higher pressures acting on the cones (figs. 5, 7, 9, and 11), the boundary layer on these bodies moved against a less adverse pressure gradient and therefore did not separate as readily.

The effect of Mach number on pressure recovery was larger for the central bodies with curved profile than for the conical central bodies. At the Mach numbers of 1.00 and 1.10, the curvature of the elliptical and parabolic central bodies was shown by the pressure distributions (figs. 5 and 7) to result at high mass-flow ratios in a region of local supersonic velocities terminated ahead of the inlet lip by a strong pressure rise presumably associated with a shock. The presence of this shock adversely affected the entering boundary layer and thus reduced the peak values of pressure recovery. As is shown by figure 28, the shock-separation criterion of reference 16 for turbulent boundary layers indicates that the shock may have separated the entering flow. The minimum pressure rise required to separate the boundary layer of the two curved-profile central bodies at various points along their surfaces was calculated by the methods of reference 16 and is plotted in figure 28. At various points along the surface of these two central bodies, the local velocity was calculated from the observed pressure distribution and the pressure rise which would result from a normal shock at this velocity was then calculated and plotted in figure 28. The shocks actually occurred on the elliptical and parabolic central bodies at an X/D of about -0.2 (see figs. 5(j) and 7(i)), where, according to the criterion of reference 16, the resultant pressure rise was more than sufficient to separate the boundary layer.

In order to indicate the magnitude of the loss in internal-flow performance caused by the rapid expansion rate of the diffuser, the dashed curve in figure 27 was plotted with the 22°-cone curves from data for a 6° annular diffuser of an area expansion ratio of 1.75 (ref. 17). The curve is plotted for a range of relative mass-flow ratio for which the entering boundary layer of the 22°-conical configuration should be thin. Although the initial boundary layers and the area ratios were different for the diffuser of reference 17 and the diffuser of this investigation, most of the difference between the curves for the two diffusers is considered to be the effect of the rapid expansion of the diffuser of the NACA 1-80-100 configuration. The total-pressure recovery of this diffuser was about 2.5 percent less than that of the 6° diffuser at $m/m_o = 0.56$, and the decrement increased gradually as the mass-flow ratio was increased.

[redacted]

In figures 29 to 31 are presented radial distributions of total-pressure ratio after diffusion at $M_o \approx 1.10$ and $\alpha = 0^\circ$. In all cases, flow separation from the duct inner surface was indicated to have occurred at some point upstream from the pressury-recovery-measurement station. At low mass flows, separation occurred ahead of the inlet because of the unfavorable pressure gradient there. (See, for example, fig. 9(a), $m/m_o = 0.12$.) At mass-flow ratios sufficiently high to avoid separation ahead of the inlet, separation was present in the diffuser because of the rapid area expansion.

At all Mach numbers, the total pressures tended to be fairly uniform around the annulus, the conical-central-body configurations tending toward higher over-all levels of total pressure.

Effects of angle of attack on pressure recovery.- In figure 32 is presented a comparison of the pressure-recovery characteristics at angles of attack of 0°, 4°, 7°, and 10°. The inlets with the conical central bodies were less sensitive to angle of attack than were those with the curved central bodies. In fact, the inlet with the 22°-conical central body was affected almost negligibly by angle of attack over the mass-flow range of practical interest.

The angle-of-attack effects were accentuated by increases in Mach number. At relative mass-flow ratios greater than about 0.6, angle of attack did not affect the pressure recovery by a great amount at $M_o = 0.6$ but, at $M_o \approx 1.0$ and 1.1, the pressure recovery in this range of mass-flow ratio was reduced substantially at an angle of attack of 10° for the elliptical and parabolic central bodies. With the possible exception of the elliptical central body at $M_o = 1.1$, $\alpha = 10^\circ$ (fig. 32(c)), angle of attack caused only small changes in the maximum mass-flow ratio. The increased pressure recovery at the minimum mass-flow rates which resulted from inclining the inlets at angles of attack of 7° or 10° can perhaps be explained by the fact that the annular inlets at angle of attack of 0° were either partially or completely engulfed by the central-body boundary layer, and inclining the inlet permitted much of the boundary layer to pass over the top of the inlet and resulted in a thinner boundary layer on the lower surface. The data obtained in the tests are not sufficiently complete to explain the cause of the loops between the curves for angles of attack of 7° and 10° at relative mass-flow ratios below about 0.6.

All aspects of the internal-flow performance which can be established by reference to the data presented indicate that the inlet with the 22°-conical central body was decidedly the best of the configurations studied.

Total-pressure-ratio profiles for an angle of attack of 10° are presented in figures 33 to 35 for the maximum mass-flow low Mach number case and for high and low mass-flow cases at the maximum test Mach number.

At the higher mass-flow rates, the attitude of the entering flow was conducive to separation from the lower region of the inner lip surface. Separation of this type was never observed with the two conical central bodies, and in those instances in which it occurred for the elliptical and parabolic central bodies, it occurred only at near-maximum mass-flow ratios. The presence of such separation resulted in large peripheral total-pressure gradients and is indicated in figures 33(b), 35(a), and 35(b) by the low total pressures measured at the outboard portions of the rakes near the bottom of the duct. As is indicated by figures 33(a) and 33(b), the inlet with the elliptical central body was free of lower lip separation at low Mach numbers, but such was not the case with the parabolic central body. As the Mach number was increased, there appeared to be a greater tendency toward lower lip separation.

At an angle of attack of 7°, no lip separation was observed at any Mach number for the inlet with the parabolic central body, and only at the highest test Mach number was any lip separation indicated for the elliptical-central-body configuration. In the absence of lip separation, the flow was fairly uniform around the annulus at the pressure-recovery-measurement station.

Propulsive Thrust Comparison

Method of calculation.- A calculation of the thrust-minus-drag performance was made for the NACA 1-80-100 inlet with the four different central bodies. The calculations were made for a specific axial-flow turbojet engine of 8100-pound static thrust rating operating at $M_O = 1.1$, 35,000 feet altitude, with afterburner at military power. At each value of mass-flow ratio, the measured pressure recovery (fig. 27) was used to calculate the engine thrust and air flow. The inlet area was thereby specified so that the scale of the configuration varied with the mass-flow ratio. (The term A_1/F was held constant.) The percent thrust loss per percent pressure-recovery loss was assumed as 1.25, and the external drag coefficients were read from figures 17 to 20. The foregoing method of analysis results in no significance in the absolute values of $C_{F_n} - C_{D_e}$, but a comparison of the peak values is useful.

Results.- The peak values and the mass-flow ratios at which they occurred are as follows:

[redacted]

Central body	$\left(C_{F_n} - C_{D_e}\right)_{max}$	m/m_o
Ellipse	1.022	0.87
Parabola	1.084	.90
14° Cone	1.098	.95
22° Cone	1.093	.96

Although the inlets with the curved central bodies had the better drag characteristics, the poorer pressure recovery of these inlets precluded the realization of greater propulsive thrusts. The peak values of propulsive-thrust coefficient were about the same for the inlets with the parabolic and the two conical central bodies, but the lesser drag of the elliptical-central-body configuration was more than offset by pressure-recovery losses. Although the curvature of the elliptical-central-body surface resulted in lower pressures (and hence, lower drag) on the central body, the formation of these low pressures was simultaneously responsible for a reduced pressure recovery through the action of the shock on the entering boundary layer.

The reduction of the external drag by reducing the central-body drag load is thus generally incompatible with the maintenance of good internal-flow performance; the resultant increase in the velocities over the central body inevitably acts to the detriment of the entering boundary layer through increasing the magnitude of the unfavorable pressure gradient or, at transonic speeds, through the possibility of shock separation for curved central bodies. The effect of the compensation between the drag and pressure recovery is to reduce the sensitivity of the propulsive thrust to changes in the central-body shape.

CONCLUSIONS

A study of the drag of five annular air-inlet configurations and the internal flow performance of four of these configurations with a rapidly expanding diffuser for a Mach number range extending from about 0.6 to 1.10 led to the following conclusions:

1. There was very little effect of central-body profile on the external drag at subsonic Mach numbers but, above a Mach number of 1.0, a prominent effect of changes in central-body profile was observed with the lower external drags measured for the inlets with the curved central bodies.

2. At the higher values of the ratio of the entering stream-tube area to the body frontal area, the minimum external drag (corresponding to inlet choked) of the NACA 1-80-300 nose-inlet-central-body combination was as low as the minimum drag measured to date for an NACA 1-series open-nose inlet.

3. There was considerable effect of central-body profile on the pressure recovery of the inlets, with the conical (and in particular the 22° conical-central-body configuration) having decidedly the better pressure-recovery characteristics. The lower pressure recovery of the curved-central-body configurations at the higher Mach numbers was associated with the action of a shock on the entering boundary layer.

4. The pressure-recovery characteristics of the conical-central-body configurations were less sensitive to changes in angle of attack than were those of the two inlets with curved central bodies; the inlet fitted with the 22° cone was almost negligibly affected in the mass-flow range of practical interest. Increases in angle of attack for the curved-central-body configurations at useful mass-flow ratios produced significant losses in pressure recovery at the higher Mach numbers.

5. Increases in angle of attack generally caused only small changes in the maximum mass-flow ratio.

6. Reductions in external drag obtained by utilizing the configuration with lower pressures over the central-body surface were accompanied by resultant reductions in pressure recovery. The sensitivity of the propulsive thrust to changes in central-body shape was therefore reduced.

Langley Aeronautical Laboratory,
National Advisory Committee for Aeronautics,
Langley Field, Va., June 8, 1953.

[redacted]

REFERENCES

1. Baals, Donald D., Smith, Norman F., and Wright, John B.: The Development and Application of High-Critical-Speed Nose Inlets. NACA Rep. 920, 1948. (Supersedes NACA ACR L5F30a.)

2. Nichols, Mark R., and Keith, Arvid L., Jr.: Investigation of a Systematic Group of NACA 1-Series Cowlings With and Without Spinners. NACA Rep. 950, 1949. (Supersedes NACA RM L8A15.)

3. Pendley, Robert E., and Smith, Norman F.: An Investigation of the Characteristics of Three NACA 1-Series Nose Inlets at Subcritical and Supercritical Mach Numbers. NACA RM L8L06, 1949.

4. Pendley, Robert E., and Robinson, Harold L.: An Investigation of Several NACA 1-Series Nose Inlets With and Without Protruding Central Bodies at High-Subsonic Mach Numbers and at a Mach Number of 1.2. NACA RM L9L23a, 1950.

5. Pendley, Robert E., Robinson, Harold L., and Williams, Claude V.: An Investigation of Three Transonic Fuselage Air Inlets at Mach Numbers From 0.4 to 0.94 and at a Mach Number of 1.19. NACA RM L50H24, 1950.

6. Pendley, Robert E., Milillo, Joseph R., and Fleming, Frank F.: An Investigation of Three NACA 1-Series Nose Inlets at Subsonic and Transonic Speeds. NACA RM L52J23, 1952.

7. Sears, Richard I., and Merlet, C. F.: Flight Determination of the Drag and Pressure Recovery of an NACA 1-40-250 Nose Inlet at Mach Numbers From 0.9 to 1.8. NACA RM L50L18, 1951.

8. Selna, James, and Schlaff, Bernard A.: An Investigation of the Drag and Pressure Recovery of a Submerged Inlet and a Nose Inlet in the Transonic Flight Range With Free-Fall Models. NACA RM A51H20, 1951.

9. Sears, Richard I., and Merlet, C. F.: Flight Determination of Drag and Pressure Recovery of a Nose Inlet of Parabolic Profile at Mach Numbers From 0.8 to 1.7. NACA RM L51E02, 1951.

10. Nichols, Mark R., and Pendley, Robert E.: Performance of Air Inlets at Transonic and Low Supersonic Speeds. NACA RM L52A07, 1952.

11. Wright, Ray H., and Ritchie, Virgil S.: Characteristics of a Transonic Test Section With Various Slot Shapes in the Langley 8-Foot High-Speed Tunnel. NACA RM L51H10, 1951.

12. Ritchie, Virgil S., and Pearson, Albin O.: Calibration of the Slotted Test Section of the Langley 8-Foot Transonic Tunnel and Preliminary Experimental Investigation of Boundary-Reflected Disturbances. NACA RM L51K14, 1952.

13. Pendley, Robert E., and Bryan, Carroll R.: An Investigation of Some Factors Affecting the Drag of Relatively Large Nonlifting Bodies of Revolution in a Slotted Transonic Wind Tunnel. NACA RM L52H22, 1953.

14. Dennard, John S.: An Investigation of the Low-Speed Characteristics of Two Sharp-Edge Supersonic Inlets Designed for Essentially External Supersonic Compression. NACA RM L7D03, 1947.

15. Whitcomb, Richard T.: A Study of the Zero-Lift Drag-Rise Characteristics of Wing-Body Combinations Near the Speed of Sound. NACA RM L52H08, 1952.

16. Donaldson, Coleman duP., and Lange, Roy H.: Study of the Pressure Rise Across Shock Waves Required To Separate Laminar and Turbulent Boundary Layers. NACA TN 2770, 1952.

17. Nelson, William J., and Popp, Eileen G.: Performance Characteristics of Two 6° and Two 12° Diffusers at High Flow Rates. NACA RM L9H09, 1949.

[redacted]

TABLE I

DESIGN COORDINATES OF INLET LIP

All coordinates are in inches.

NACA 1-series profile

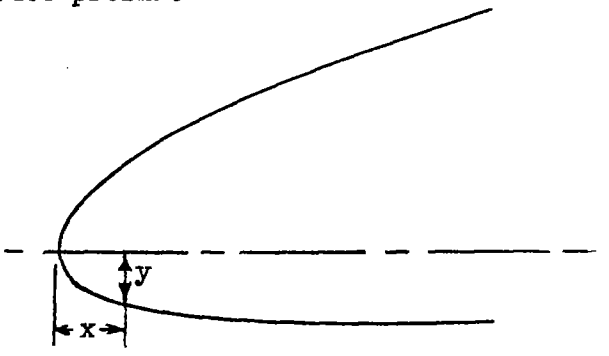

NACA 1-80-100 annular inlet	
x	y
0.000	0.000
.10	.071
.20	.091
.30	.099
1.131	.099

Inlet minimum area, 13.04 sq in. (measured)

NACA

TABLE II

CENTRAL-BODY DESIGN COORDINATES

Ellipse		Parabola	
Station x_c	Radius r_c	Station x_c	Radius r_c
0	0	0	0
.125	.377	.125	.061
.250	.532	.250	.120
.500	.747	.500	.238
.750	.909	.750	.352
1.000	1.042	1.000	.462
2.000	1.434	2.000	.874
3.000	1.704	3.000	1.235
4.000	1.906	4.000	1.546
5.000	2.060	5.000	1.806
6.000	2.176	6.000	2.015
7.000	2.260	7.000	2.174
8.000	2.316	8.000	2.282
9.000	2.345	9.000	2.339
9.645	2.350	9.645	2.350
9.895	2.350	9.895	2.350

NACA

[redacted]

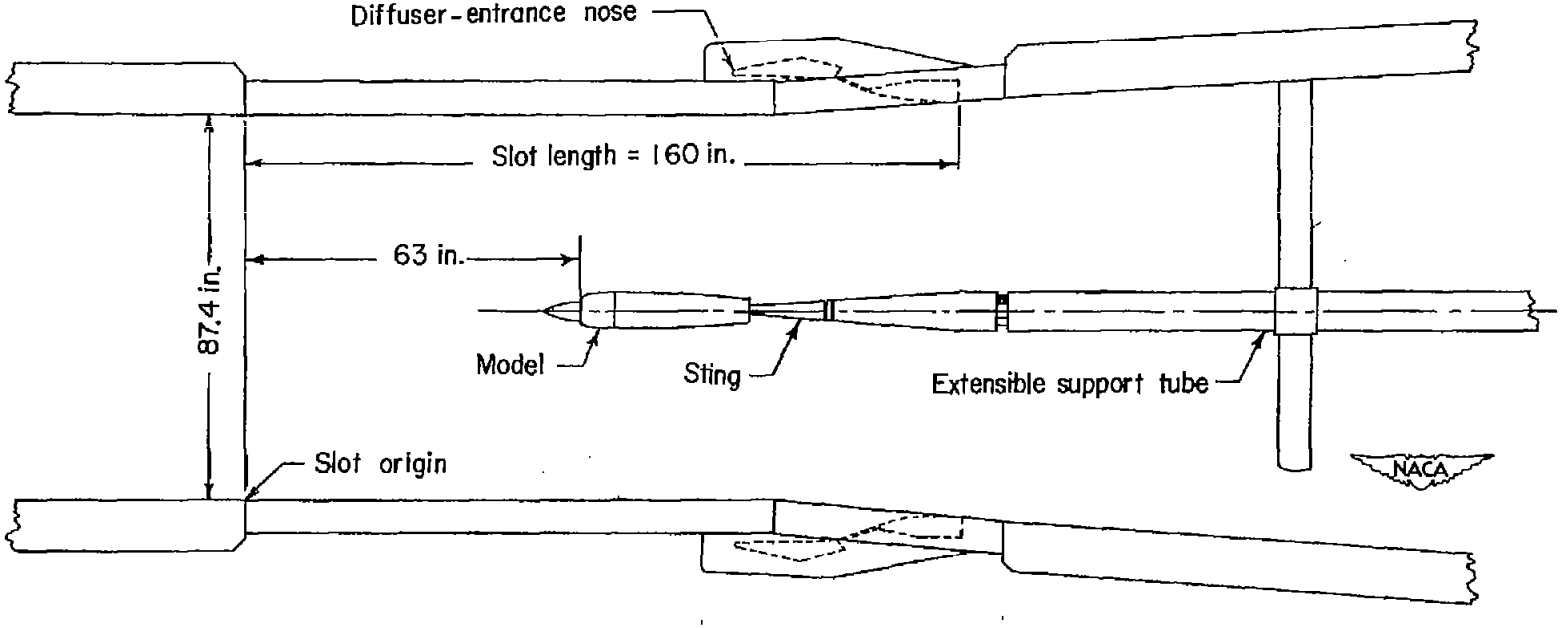

Figure 1.- Model support system in 8-foot transonic tunnel test section.

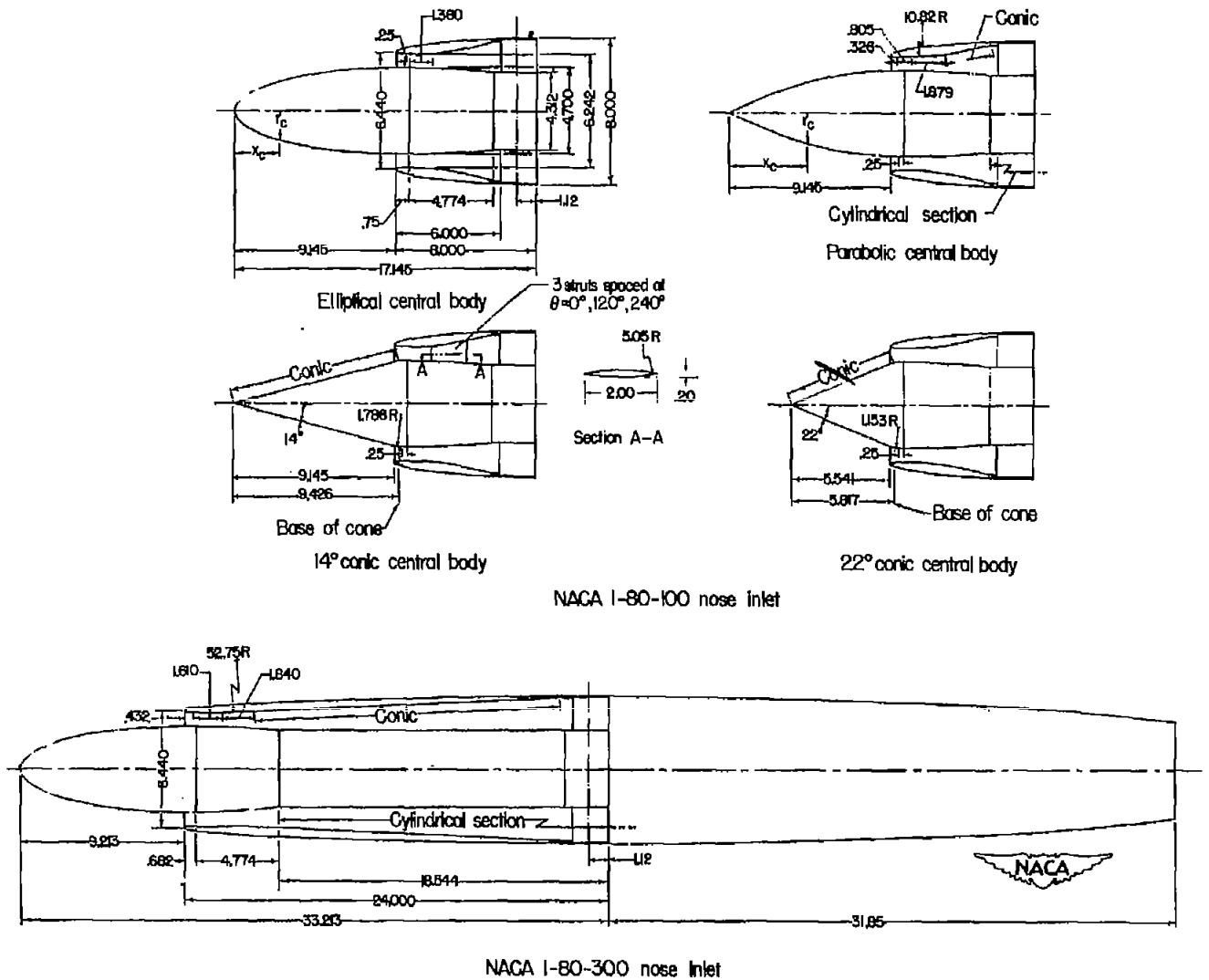

Figure 2.- Drawing of configurations tested. All linear dimensions are in inches.

NACA L-76429

Figure 3.- Photograph of components of inlet configurations.

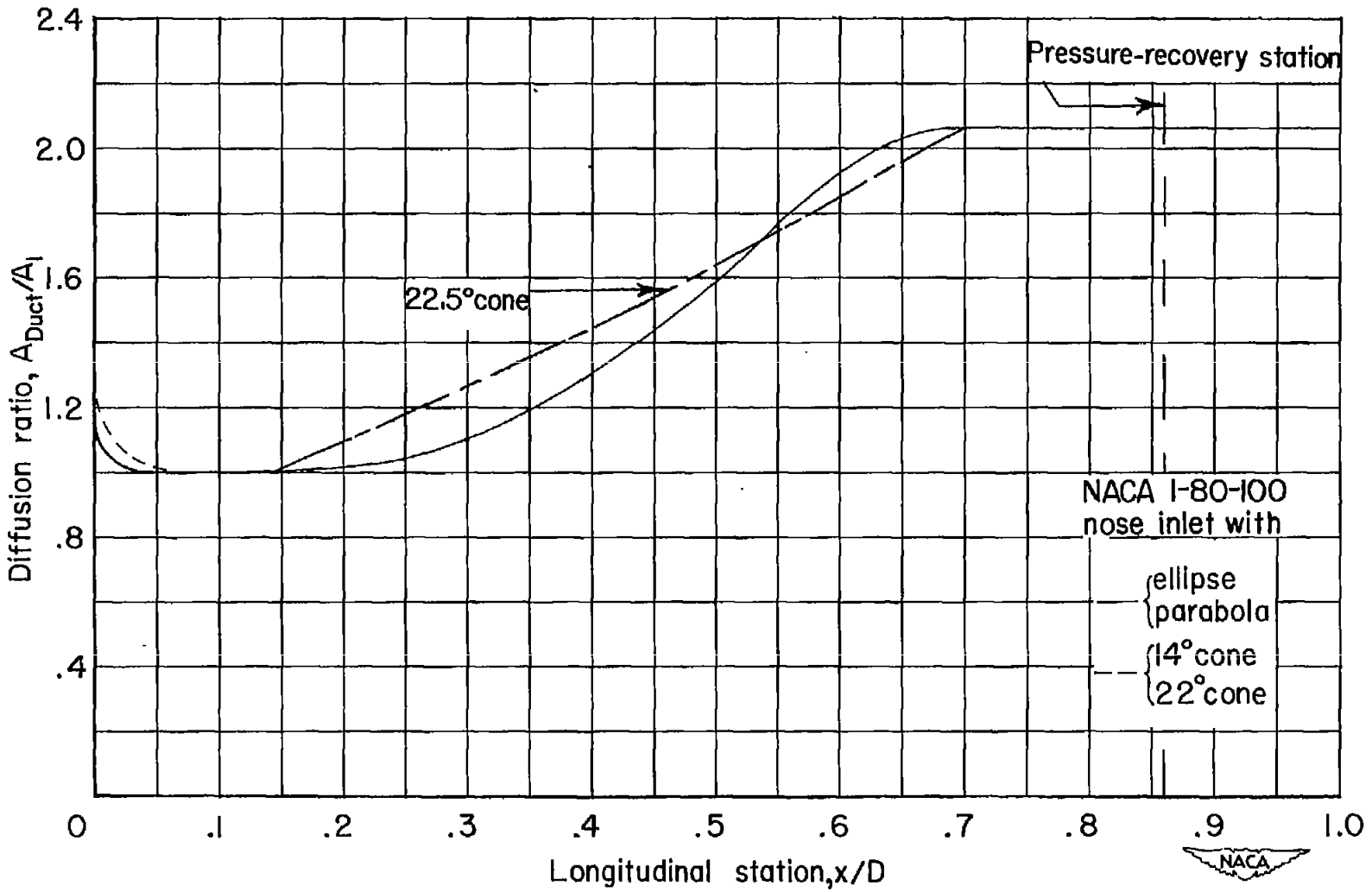

Figure 4.- Variation of inlet duct area with longitudinal station.

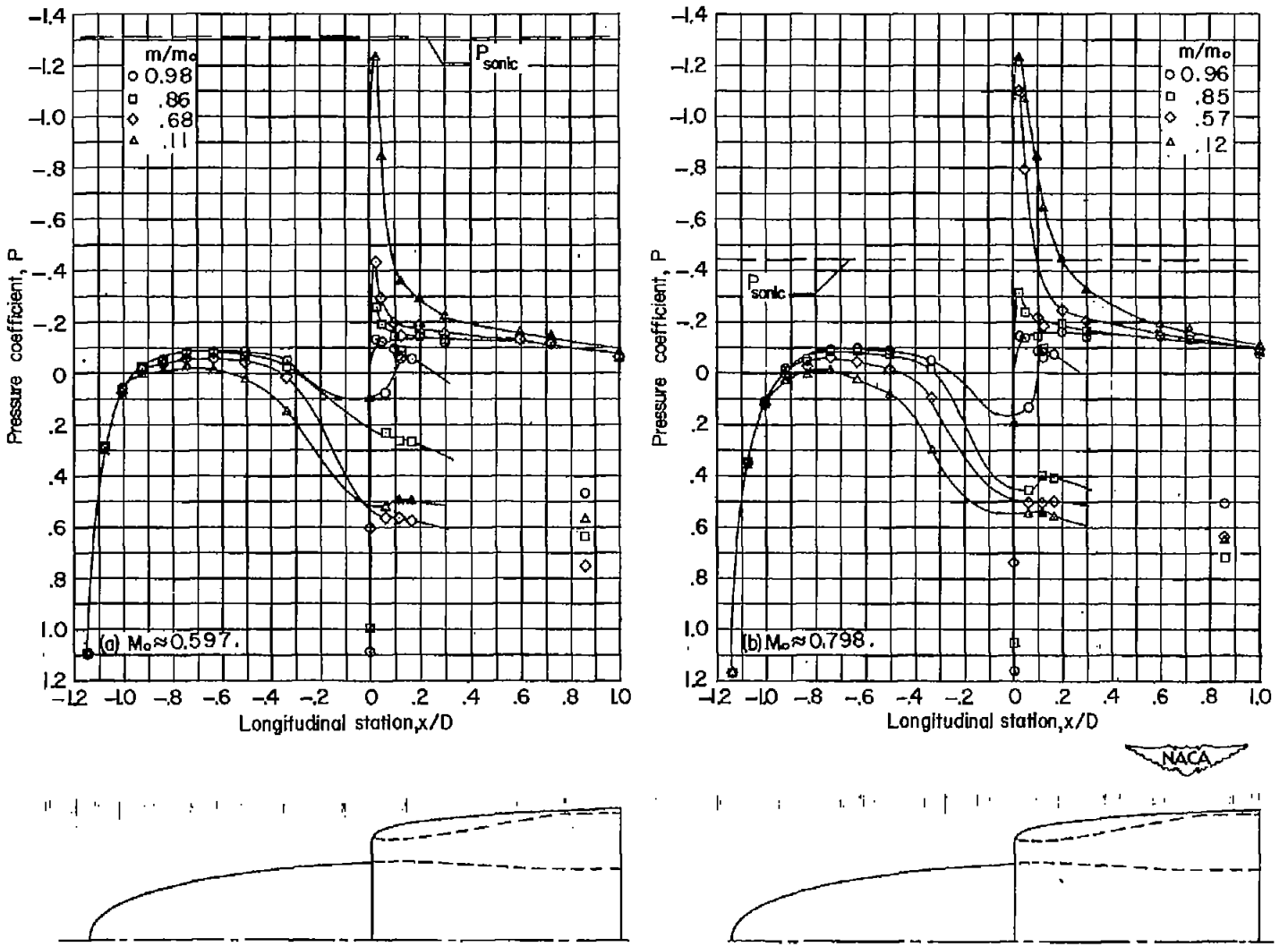

Figure 5.- Effect of mass-flow ratio on surface pressure distributions ahead of maximum-diameter station. Elliptical central body; $\alpha_i = 0^o$.

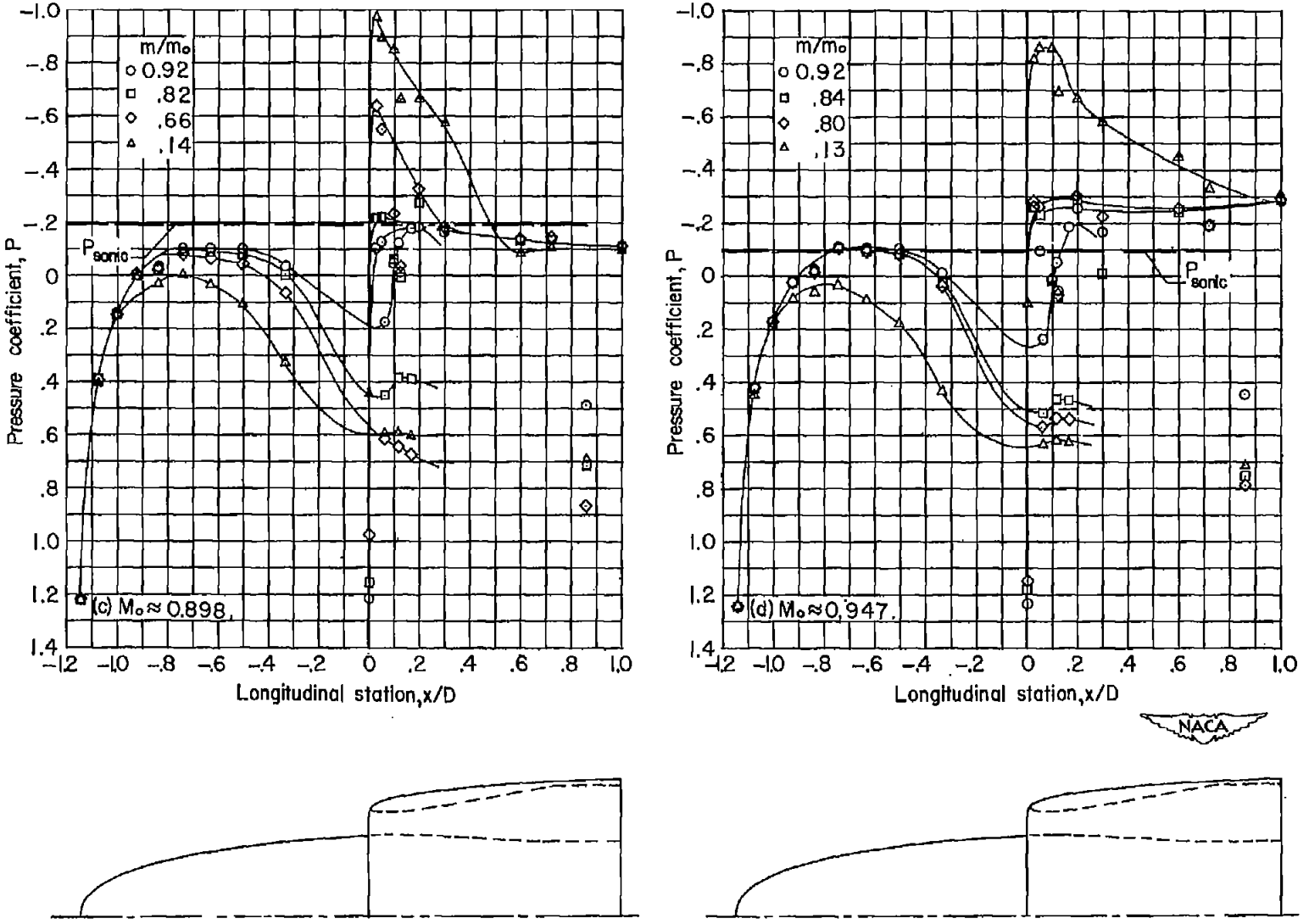

Figure 5.- Continued.

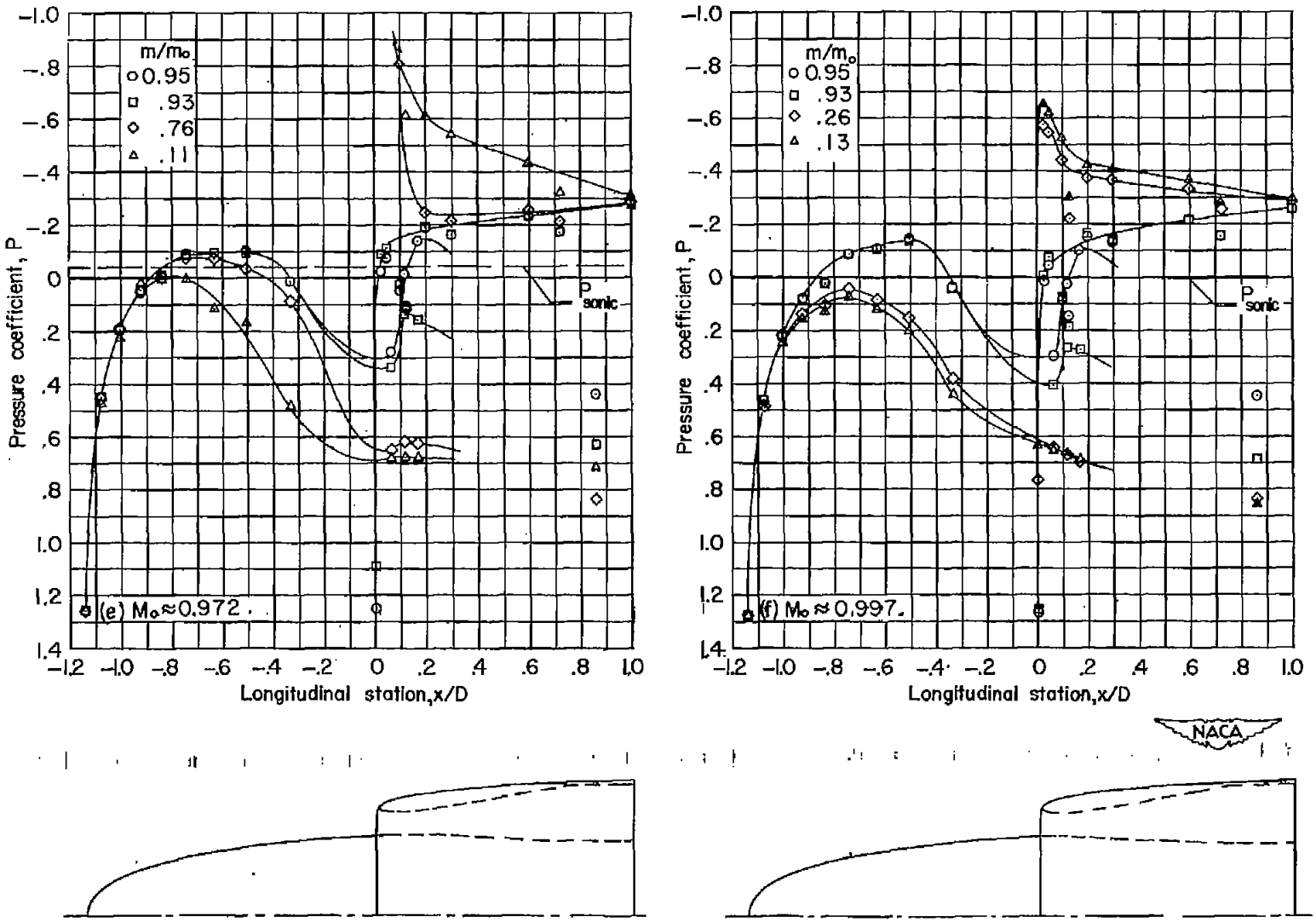

Figure 5.- Continued.

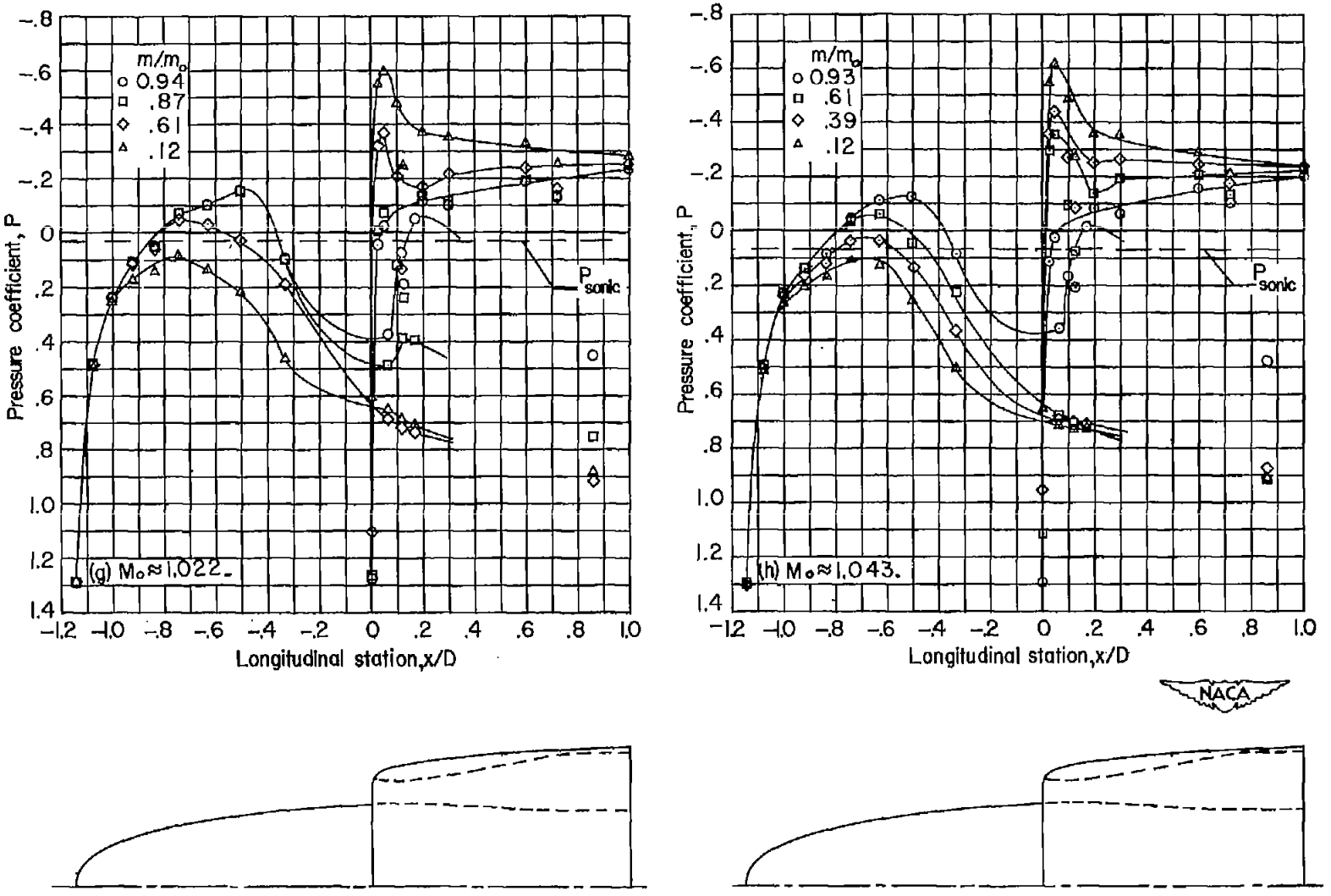

Figure 5.- Continued.

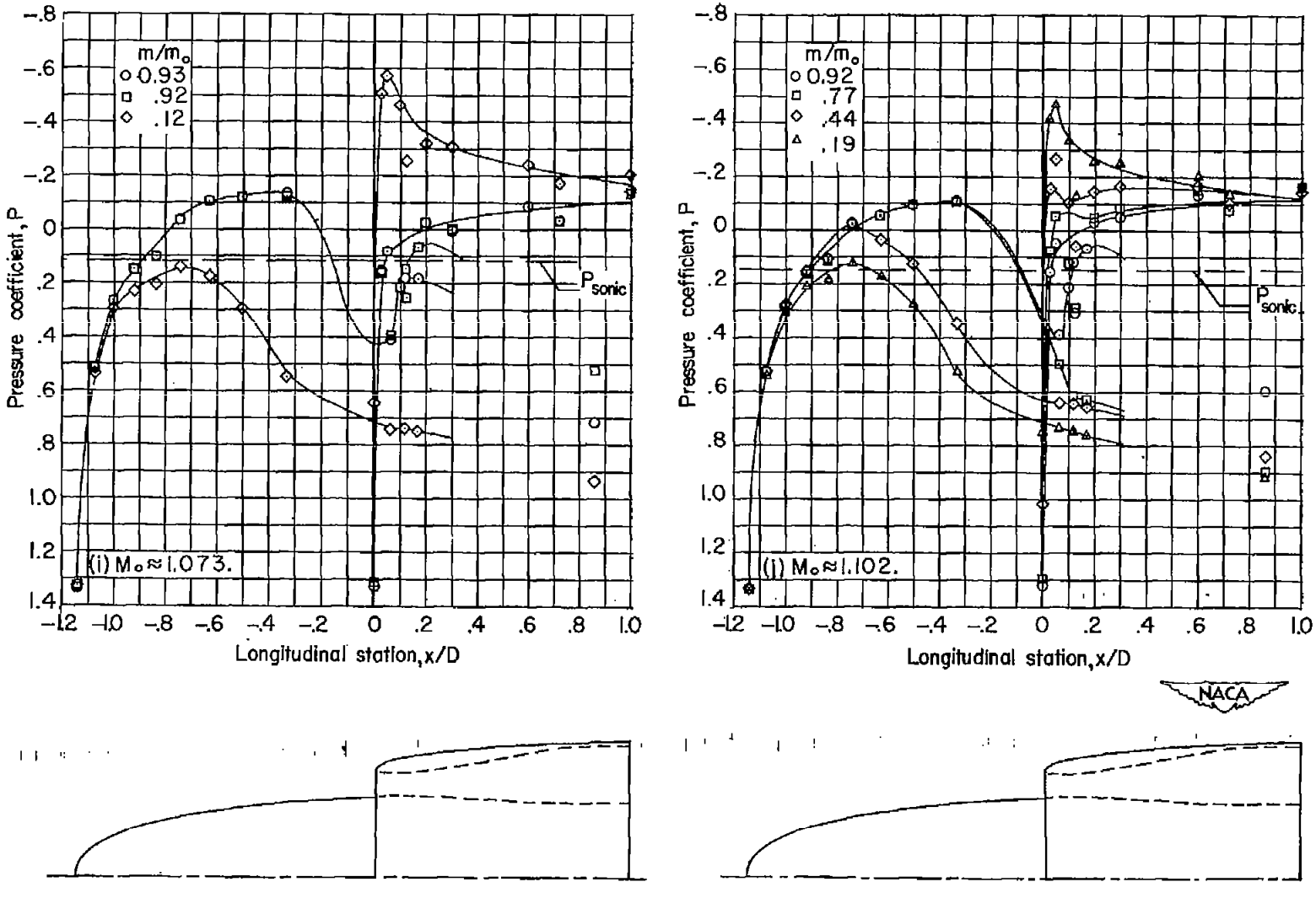

Figure 5.- Concluded.

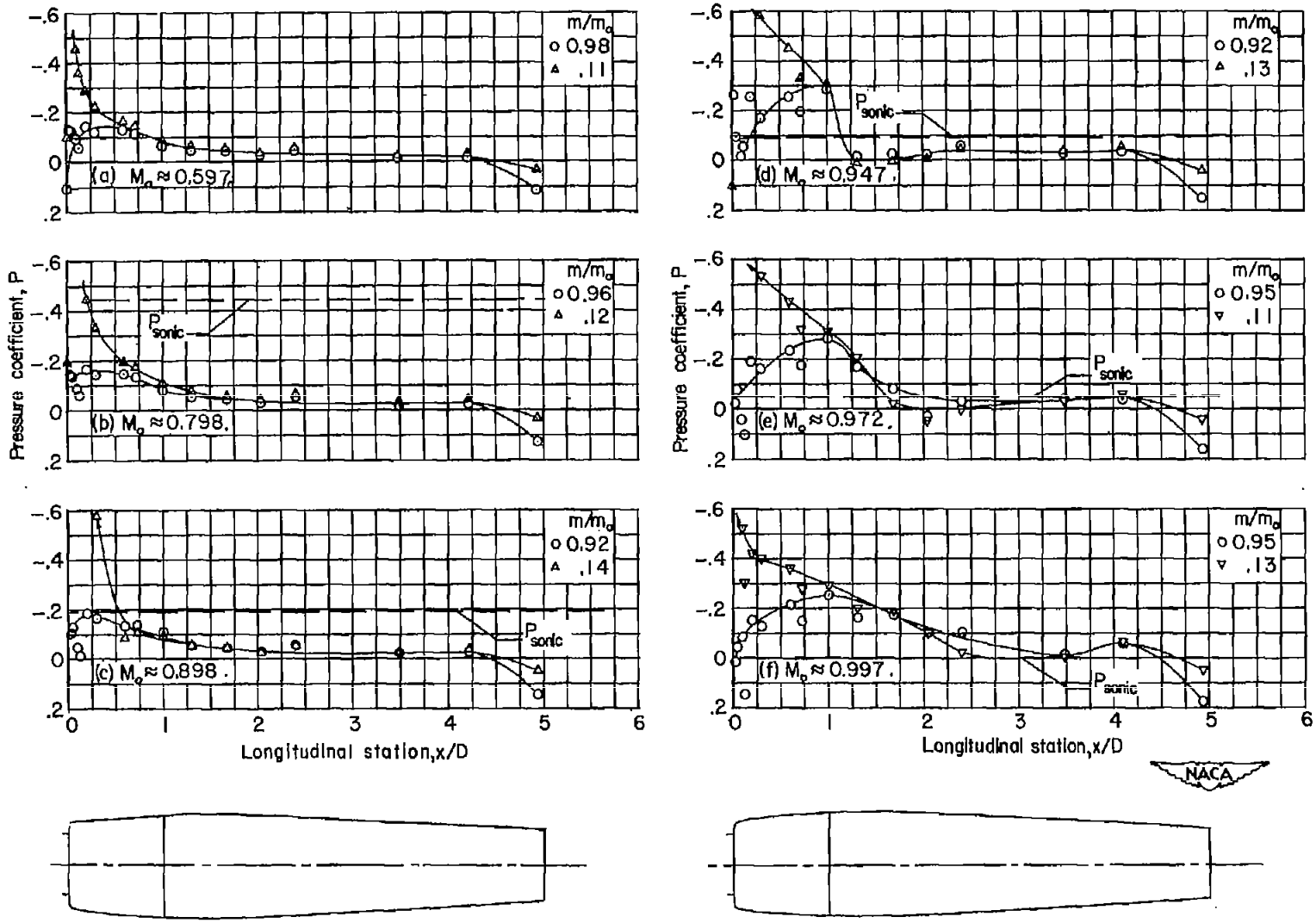

Figure 6.- Effect of mass-flow ratio on external-surface pressure distributions. Elliptical central body; $\alpha = 0^\circ$.

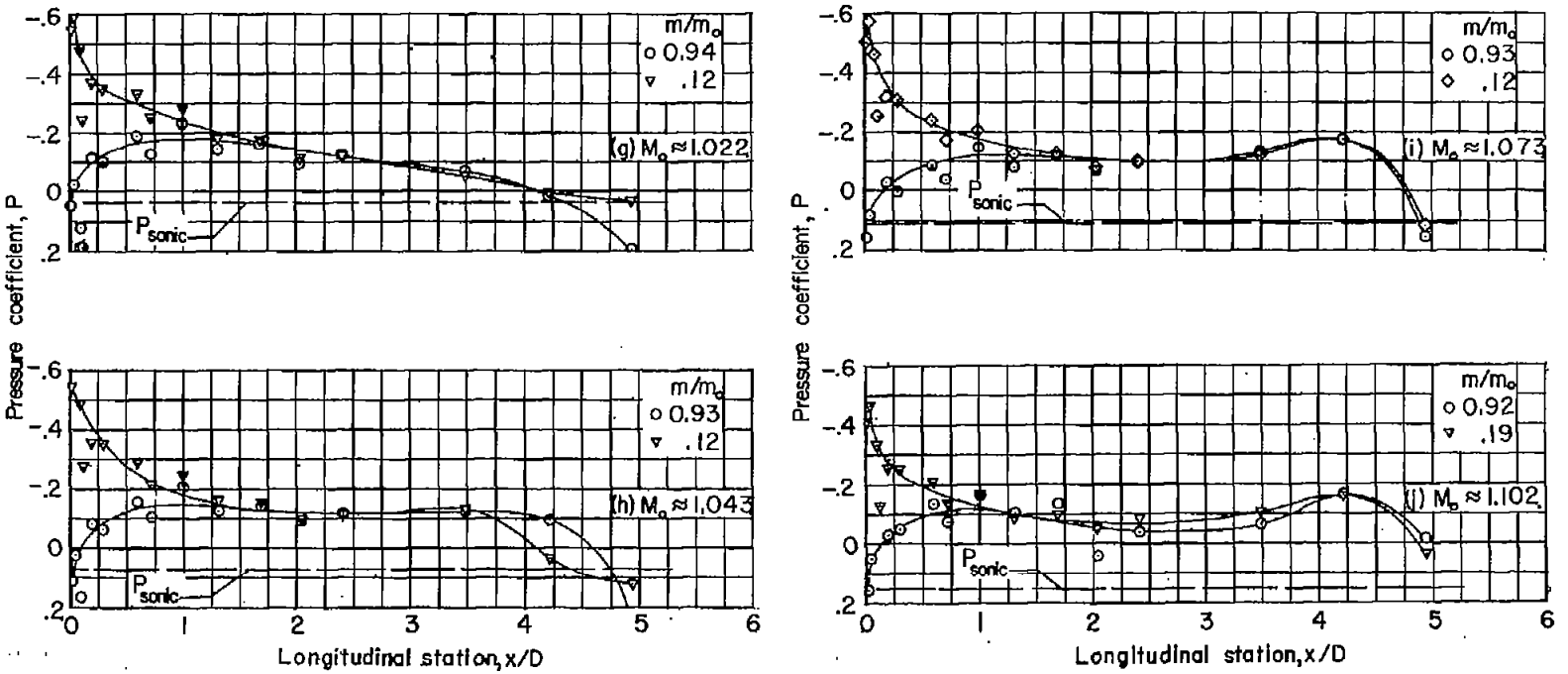

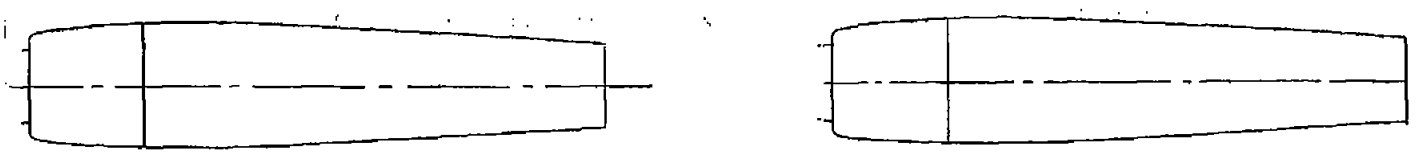

Figure 6.- Concluded.

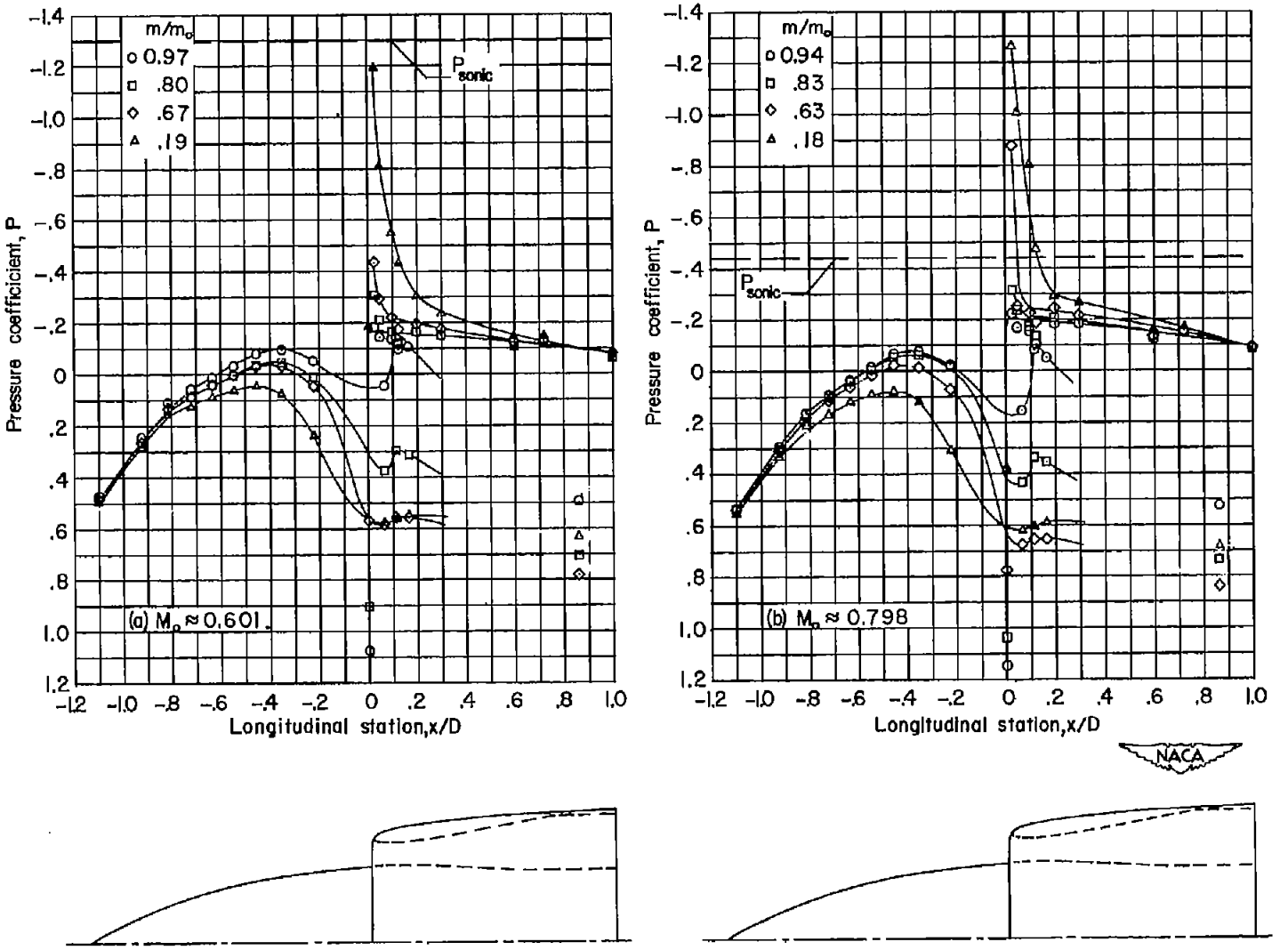

Figure 7.- Effect of mass-flow ratio on surface pressure distributions ahead of maximum-diameter station. Parabolic central body; $\alpha = 0^{\circ}$.

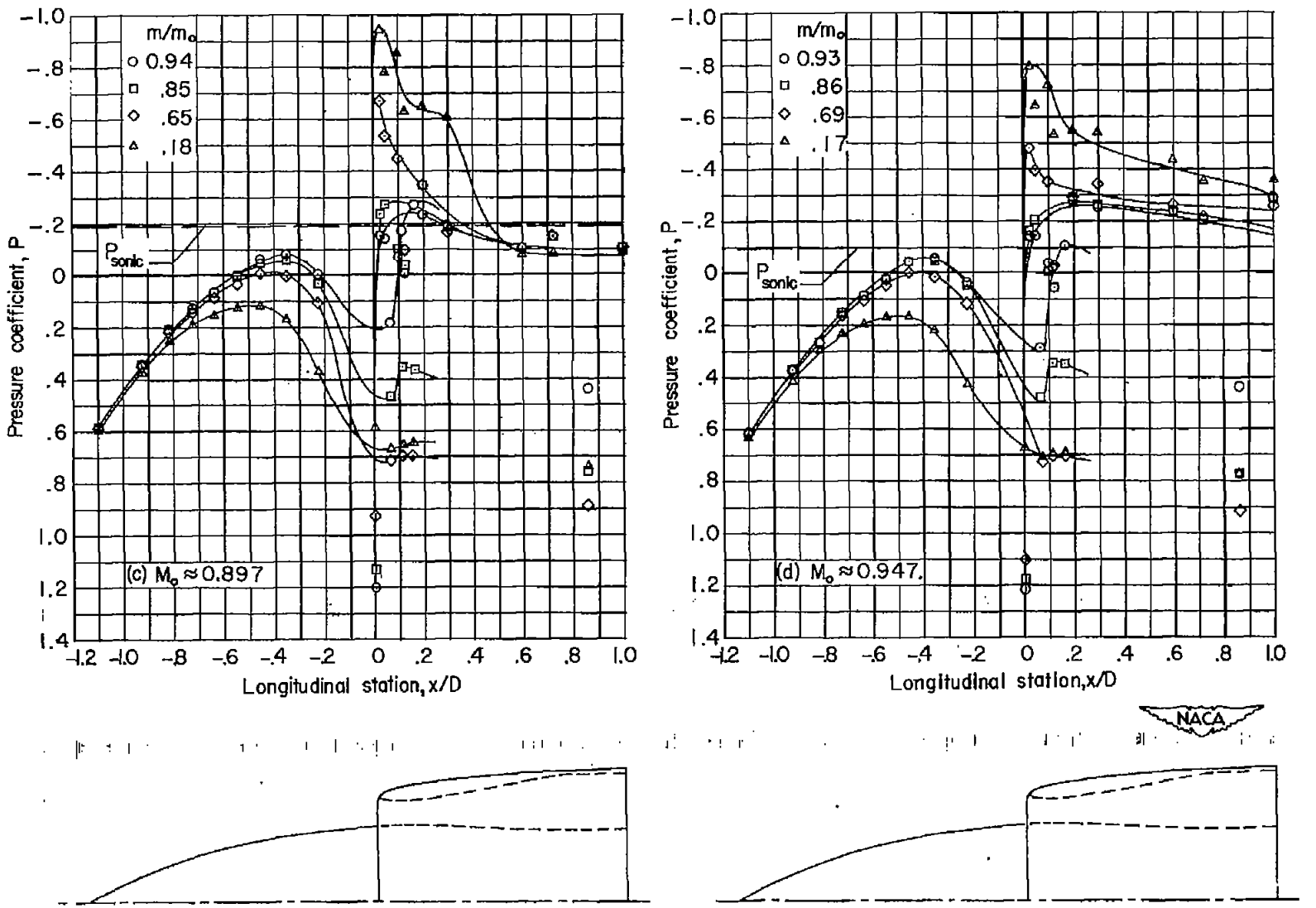

Figure 7.- Continued.

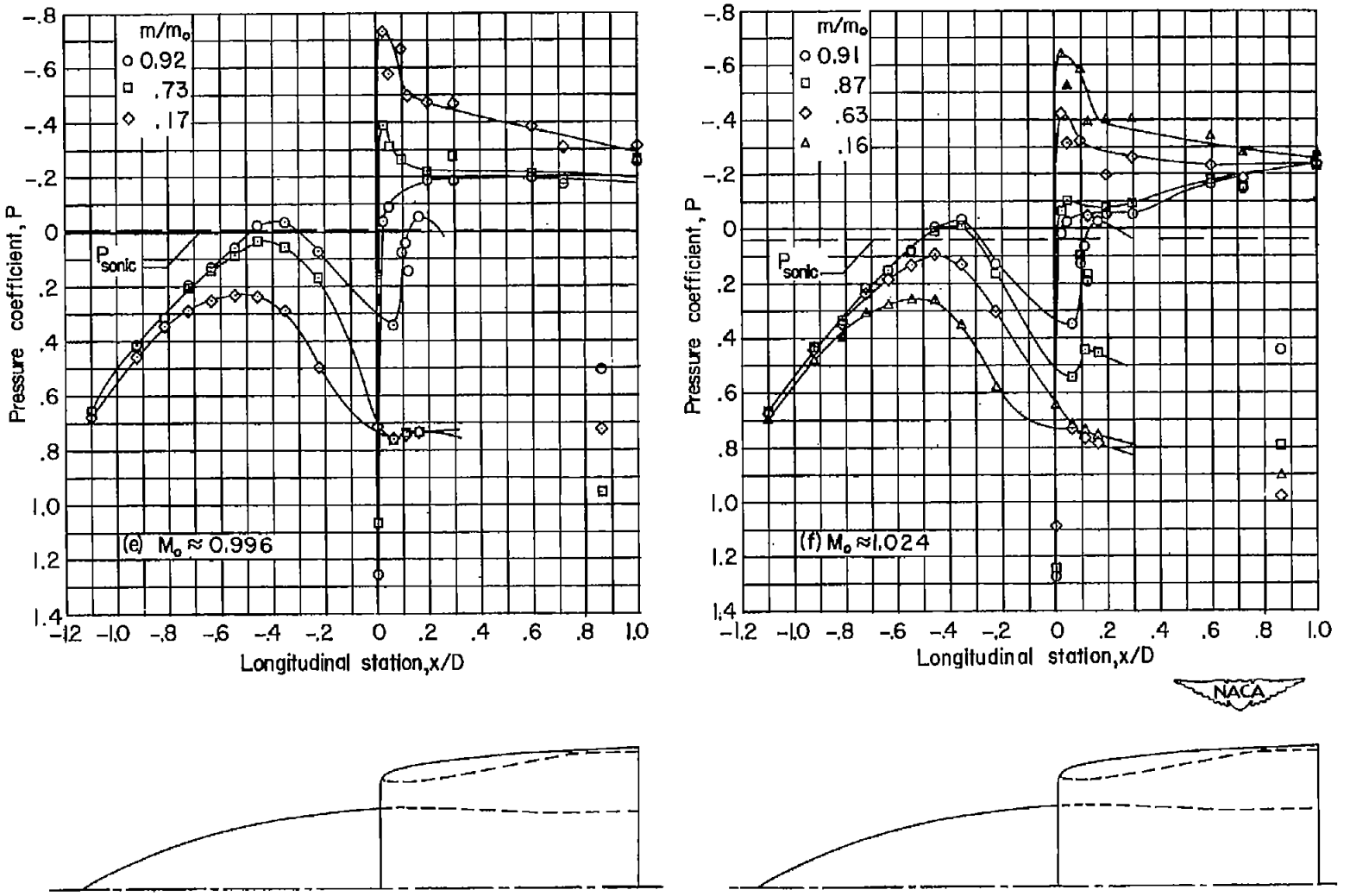

Figure 7.- Continued.

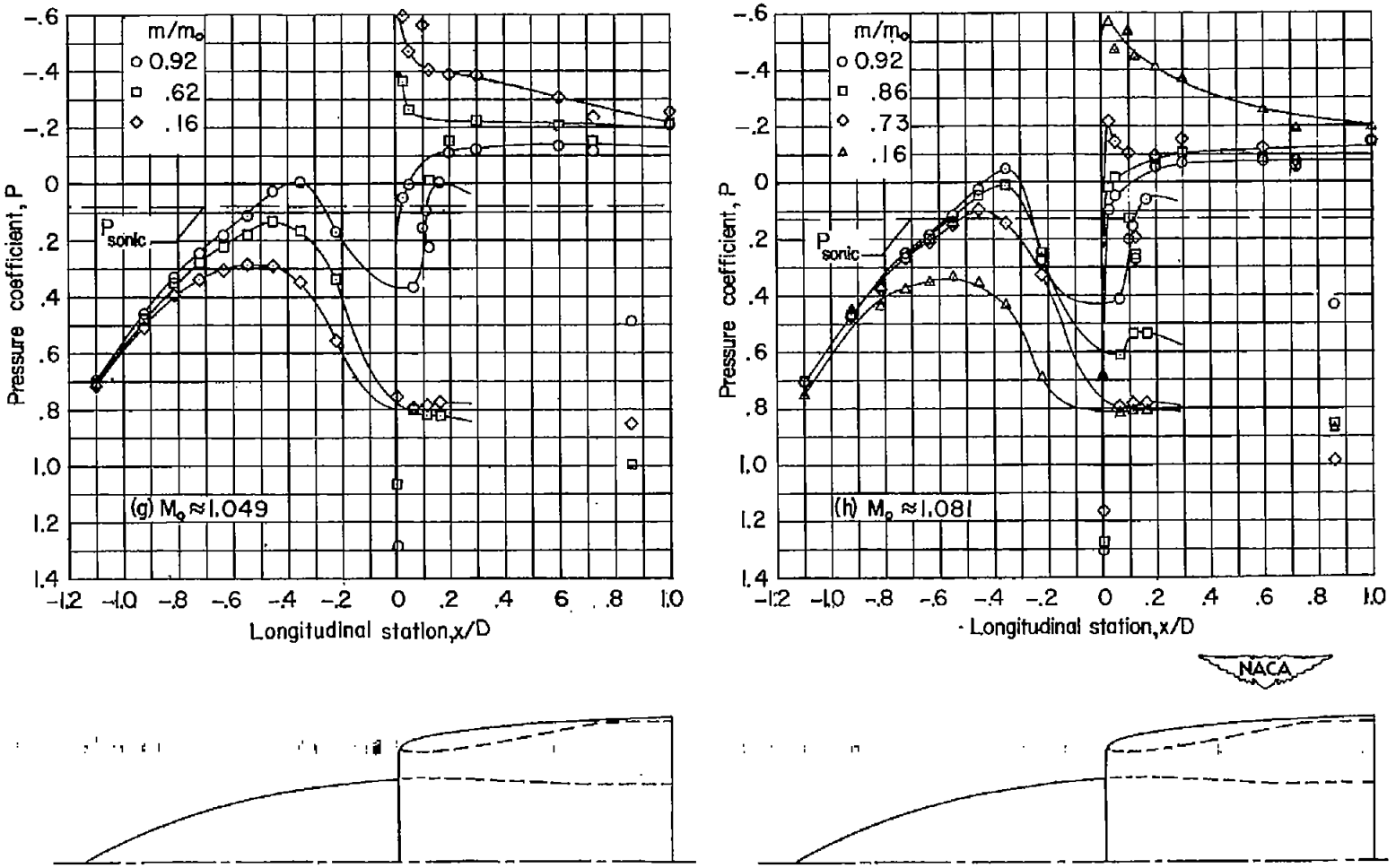

Figure 7.- Continued.

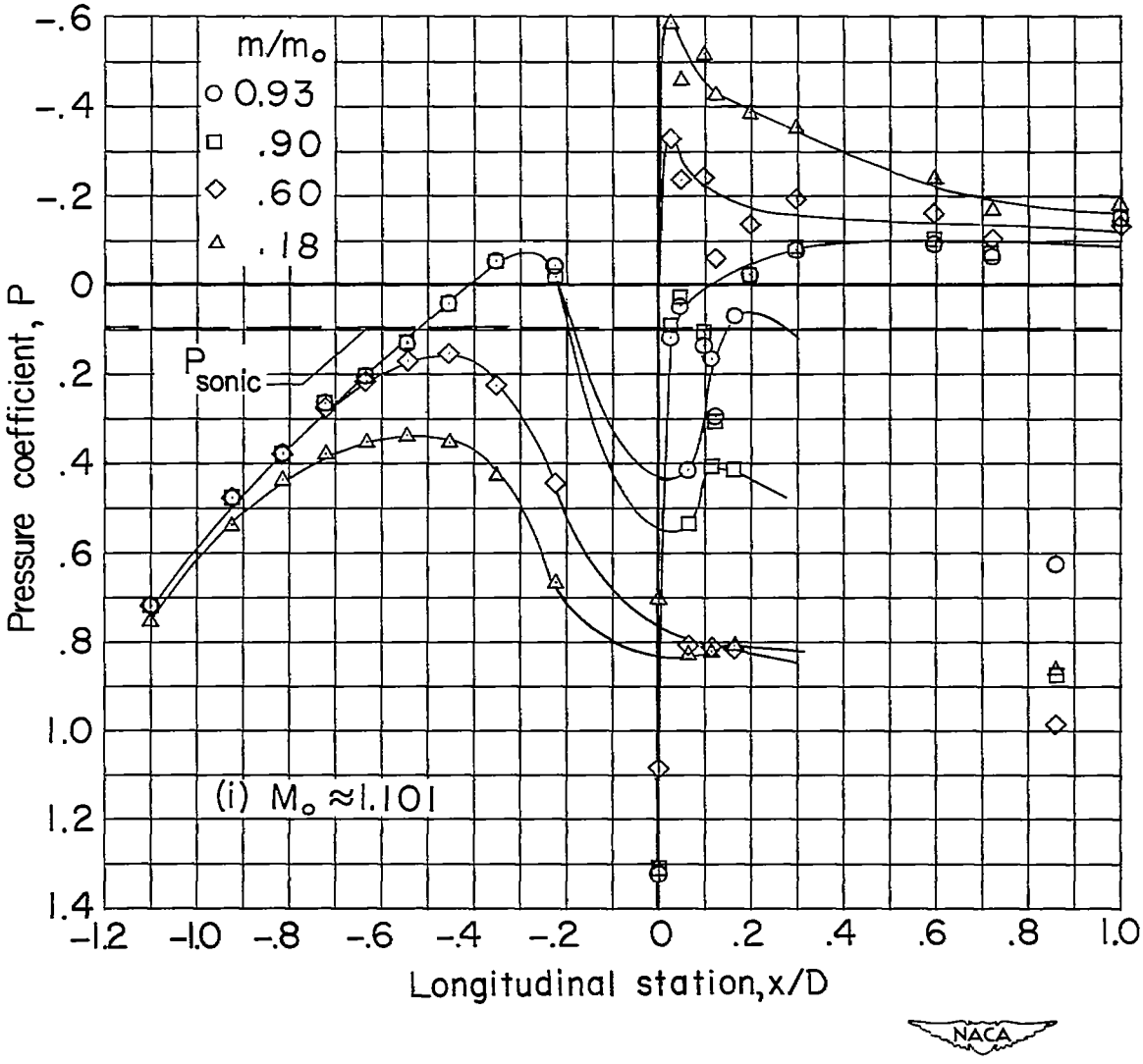

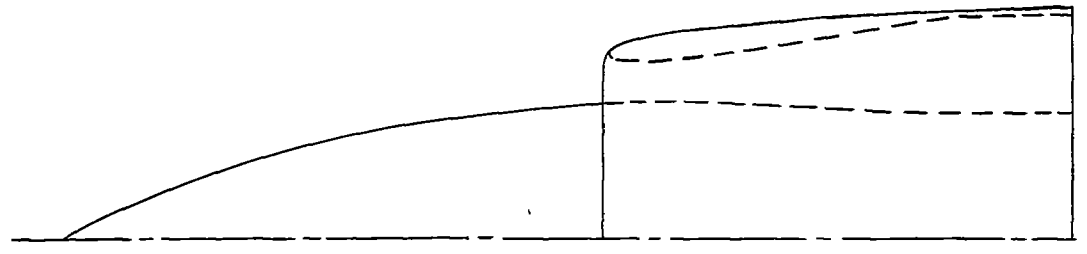

Figure 7.- Concluded.

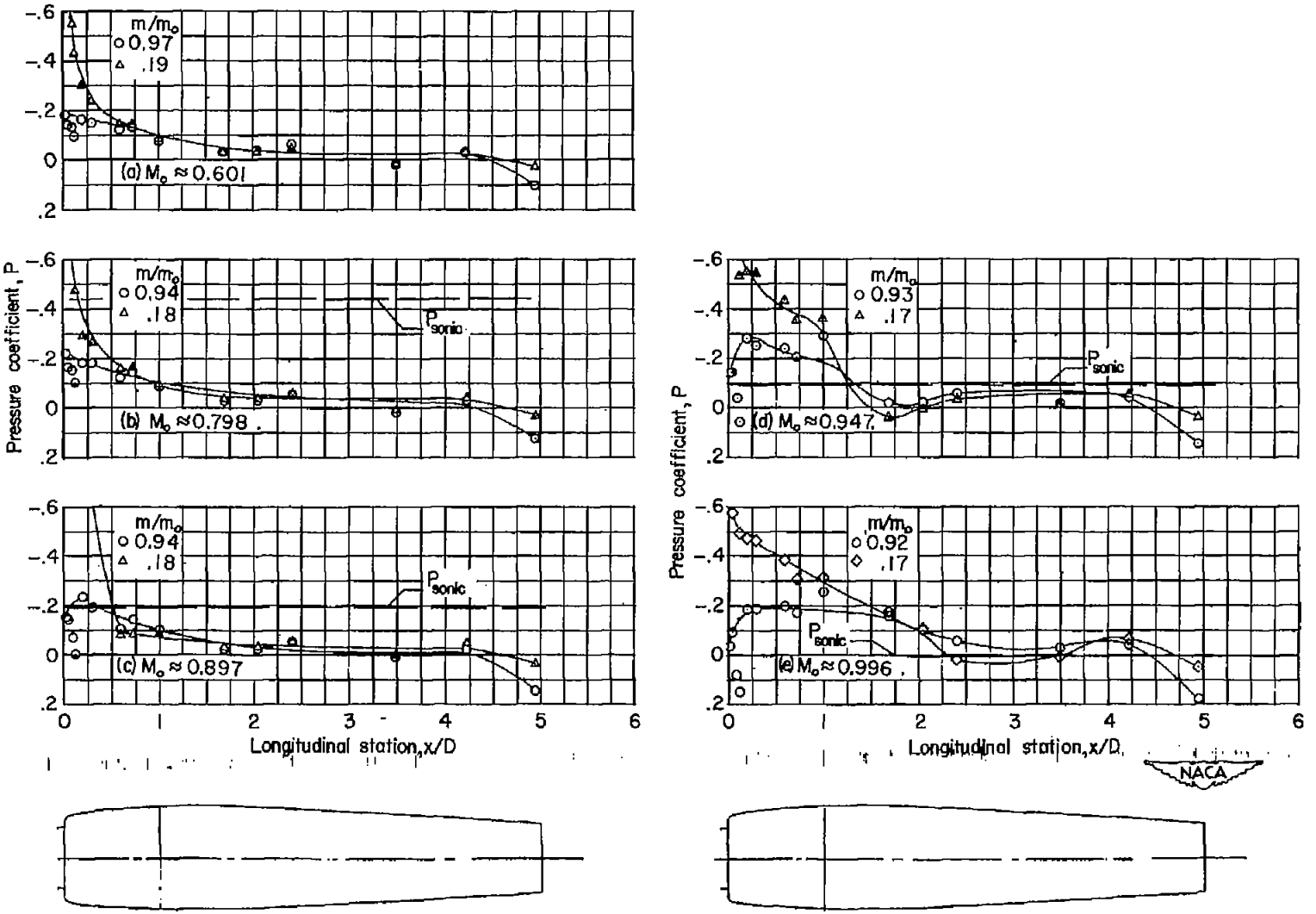

Figure 8.- Effect of mass-flow ratio on external-surface pressure distributions. Parabolic central body; $\alpha = 0^{\circ}$.

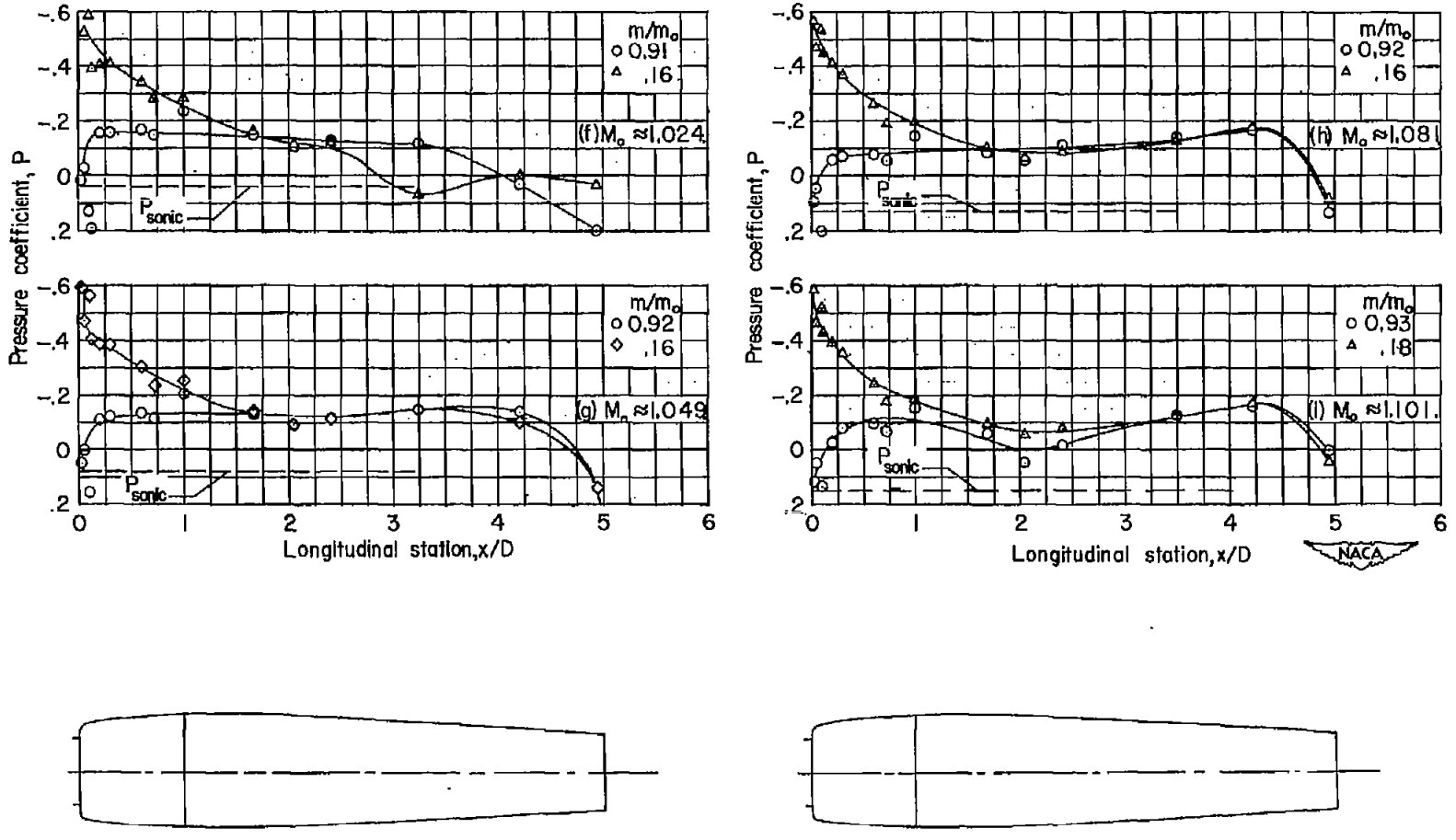

Figure 8.- Concluded.

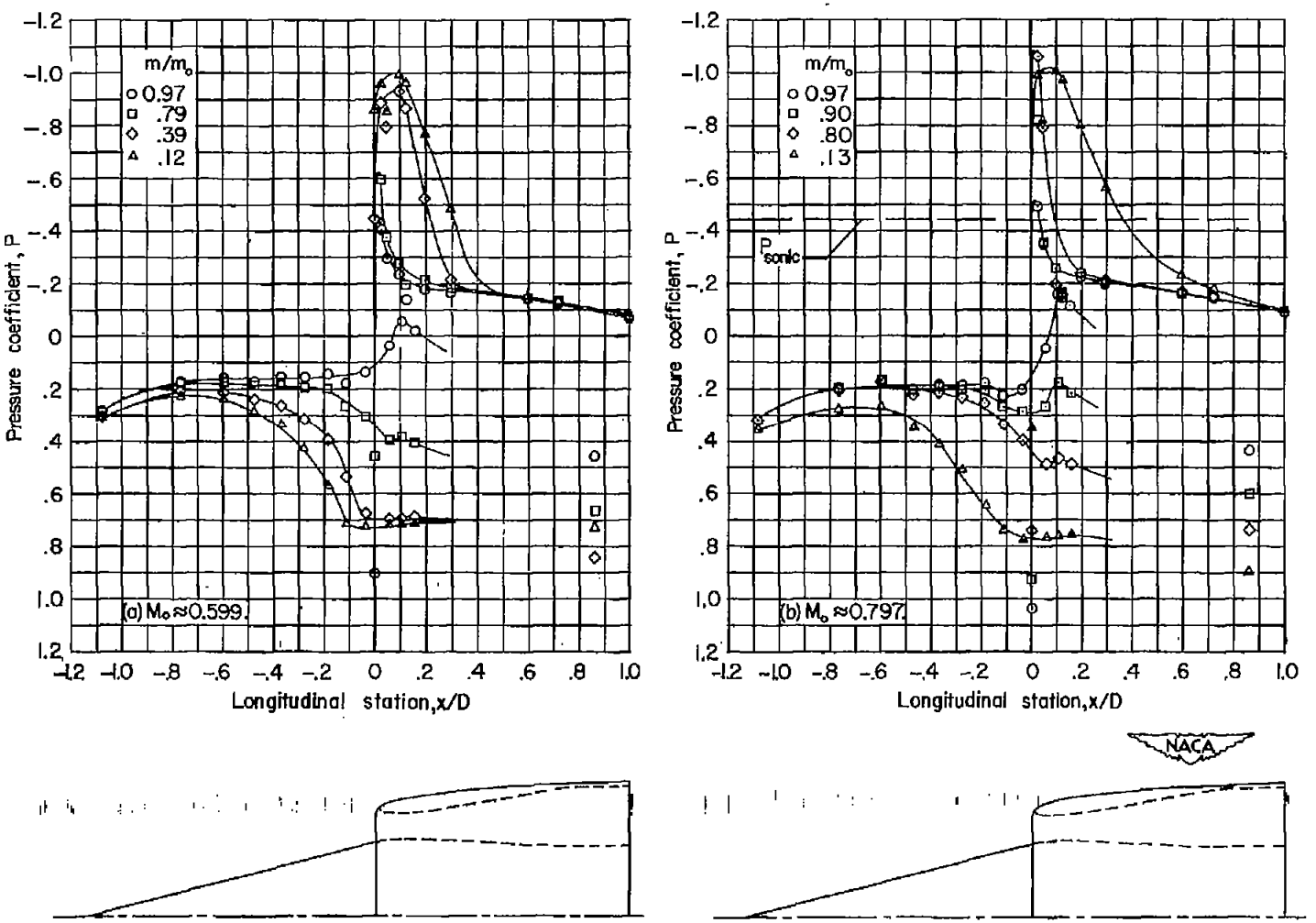

Figure 9.- Effect of mass-flow ratio on surface pressure distributions ahead of the maximum-diameter station. 14° conical central body; $\alpha = 0°$.

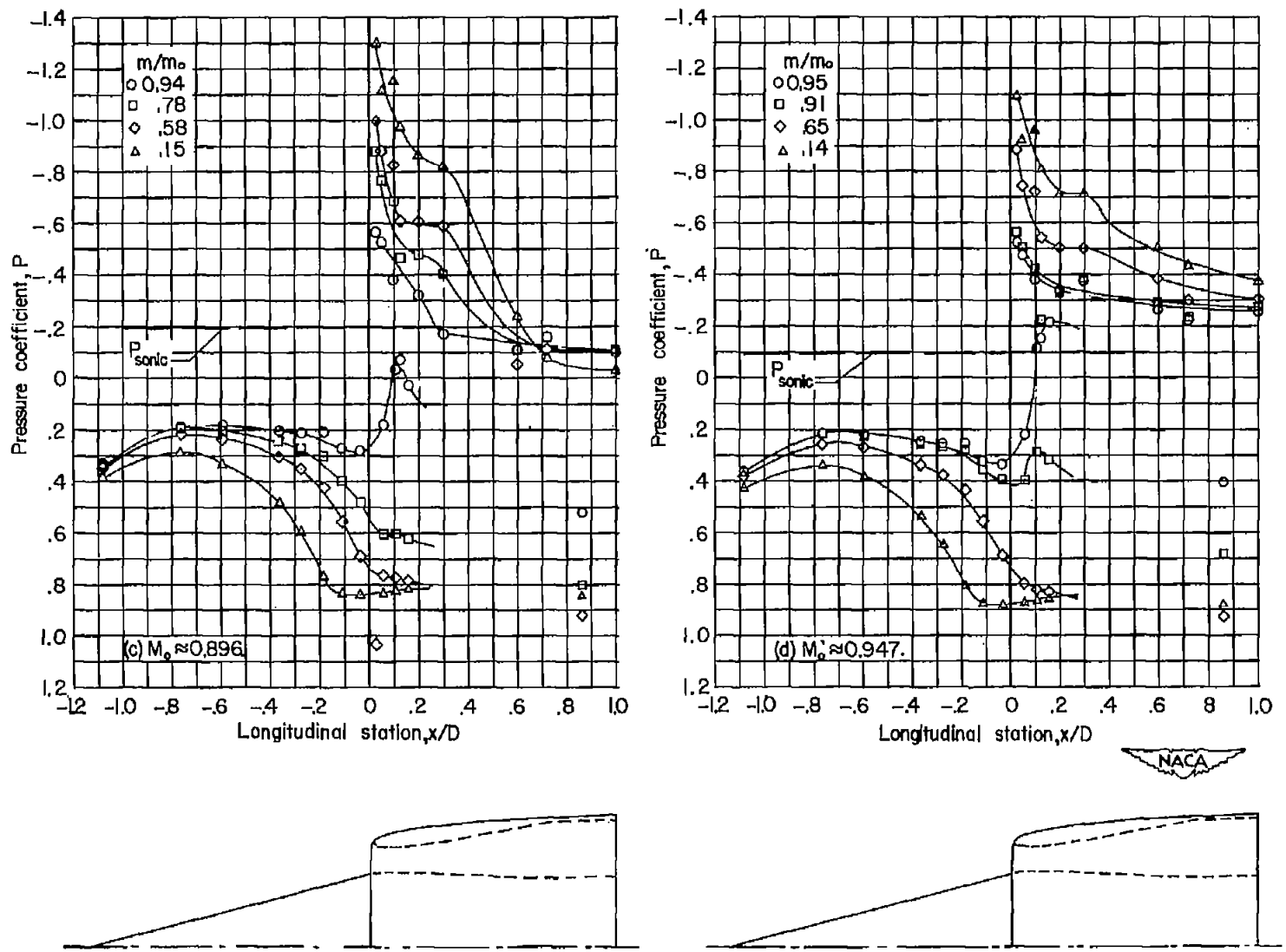

Figure 9.- Continued.

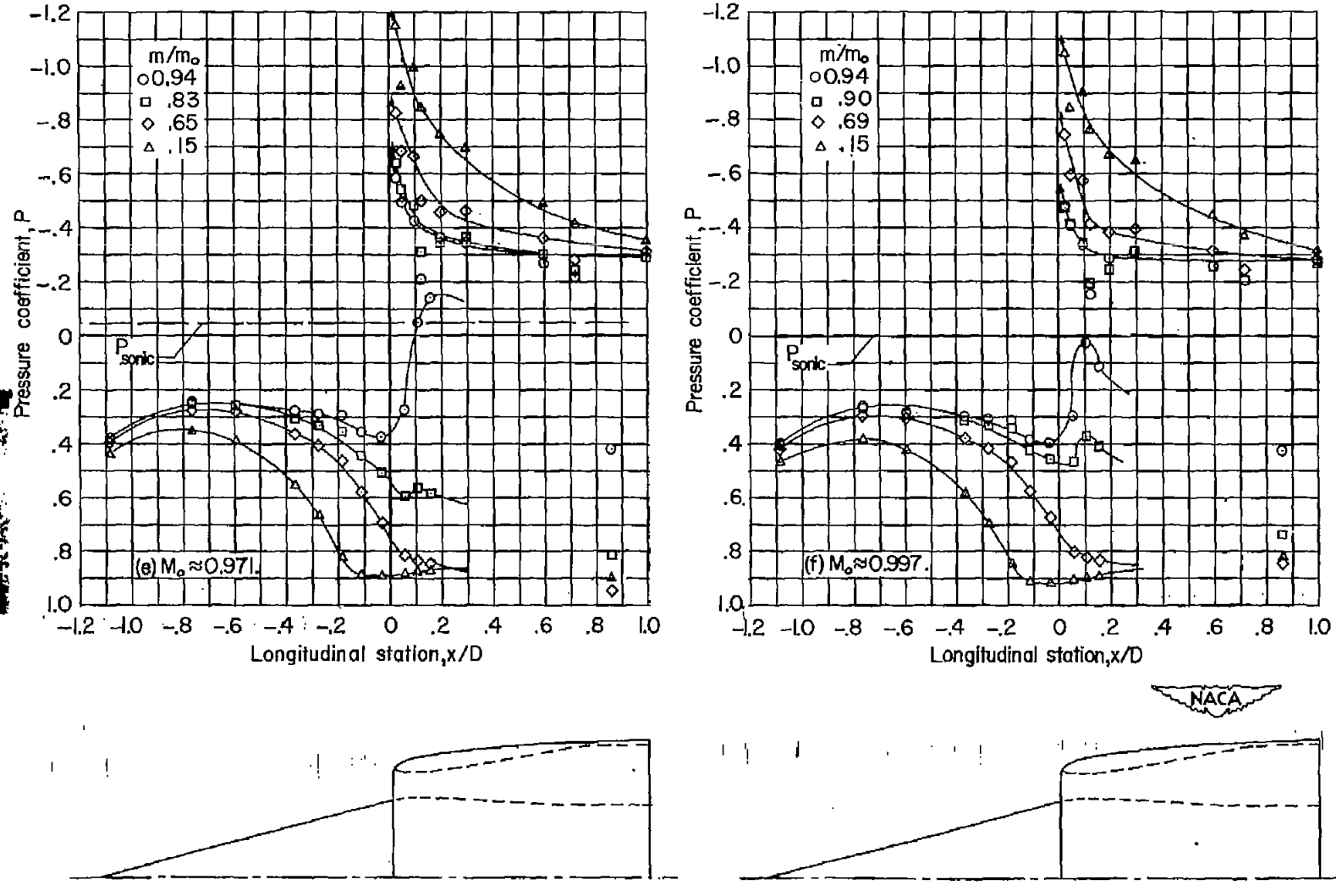

Figure 9.- Continued.

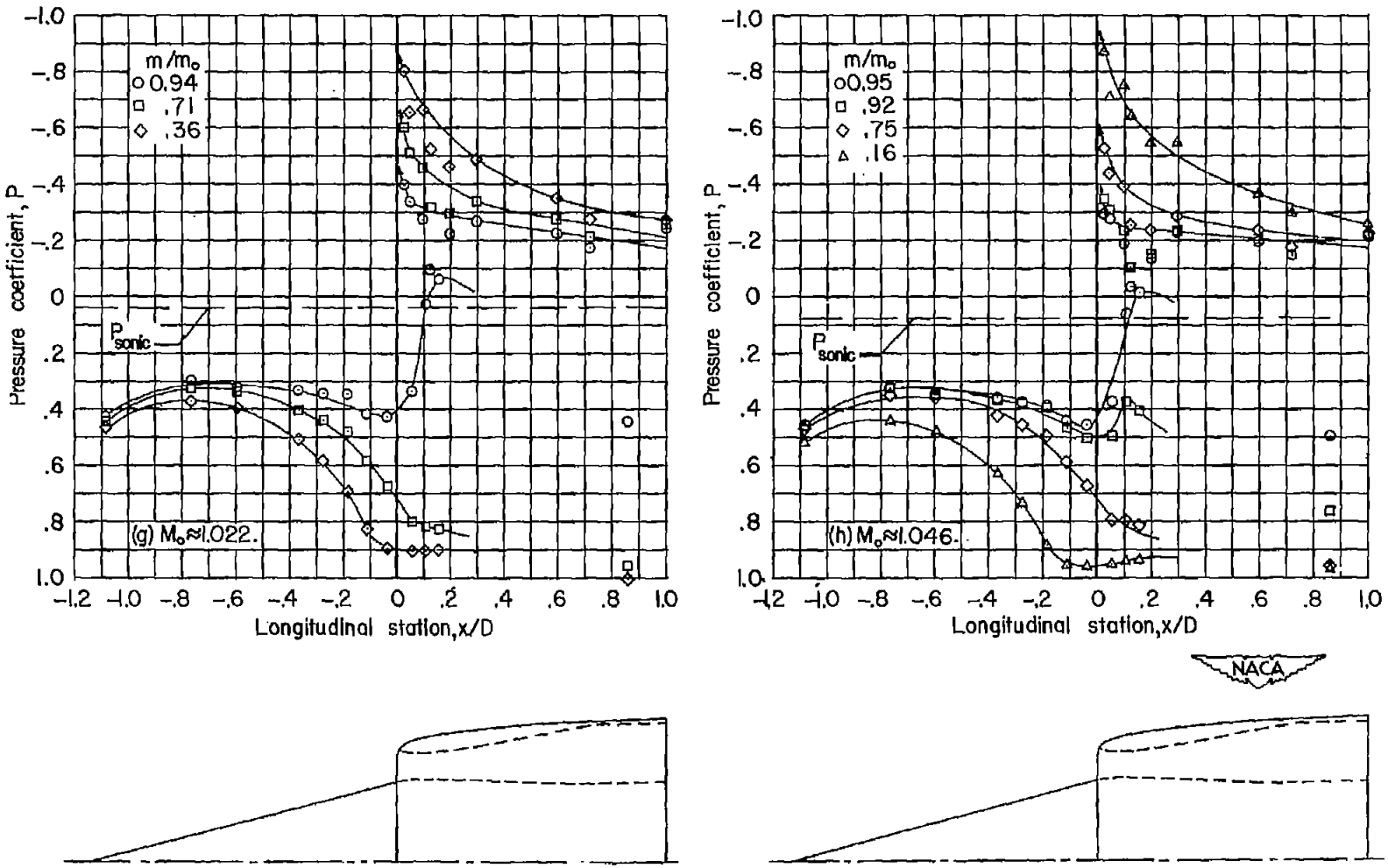

Figure 9.- Continued.

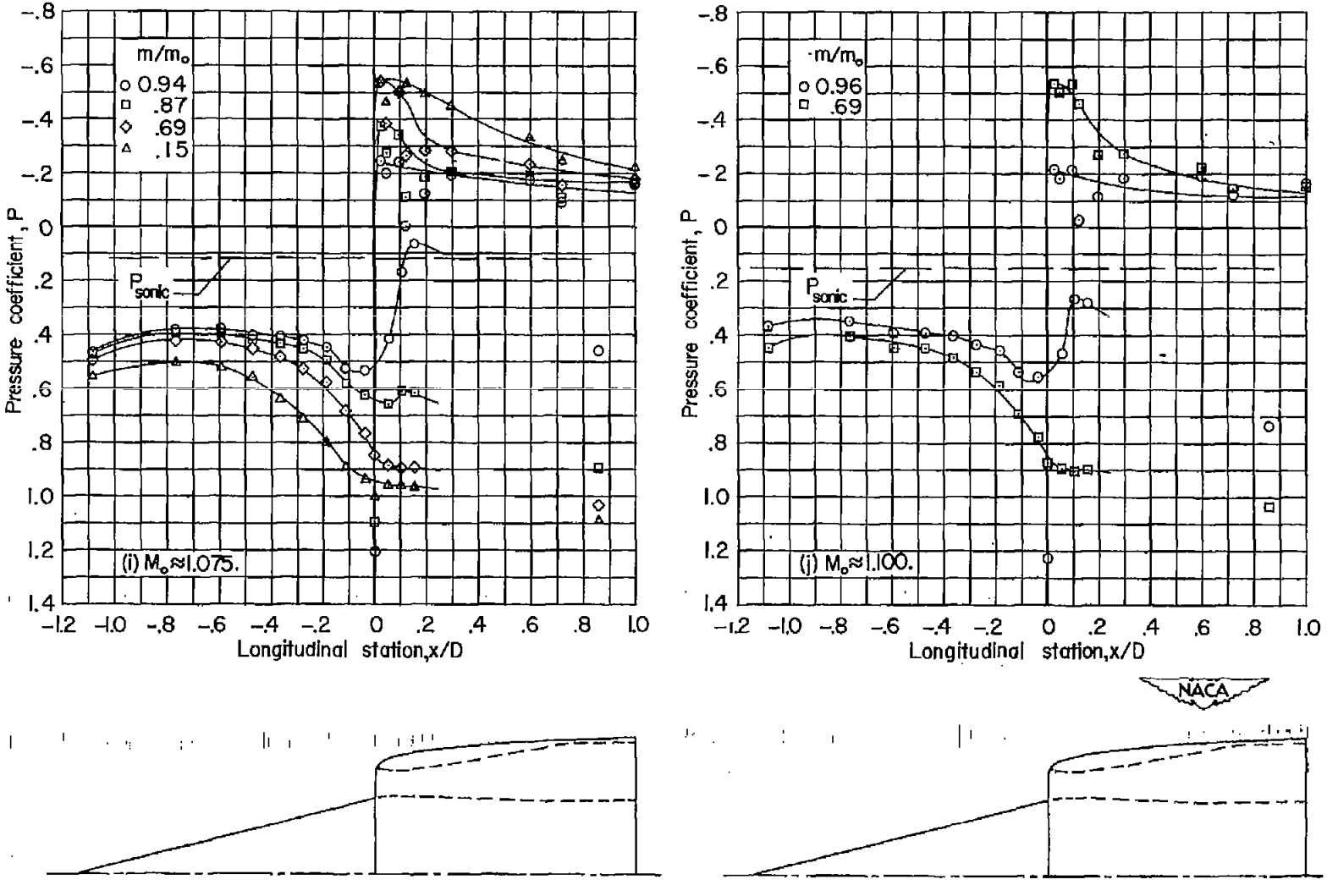

Figure 9.- Concluded.

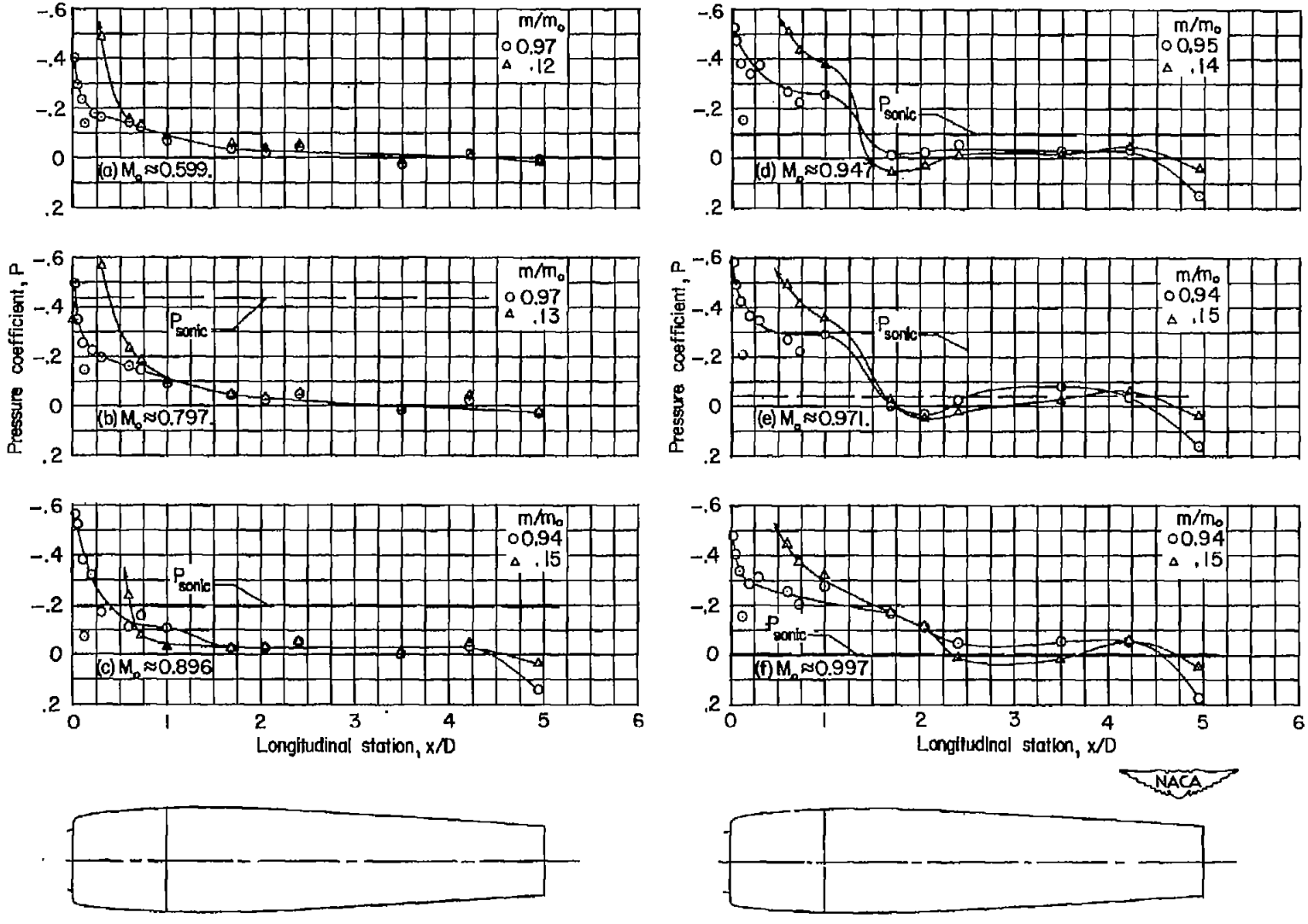

Figure 10.- Effect of mass-flow ratio on external-surface pressure distributions. 14° conical central body; $\alpha = 0°$.

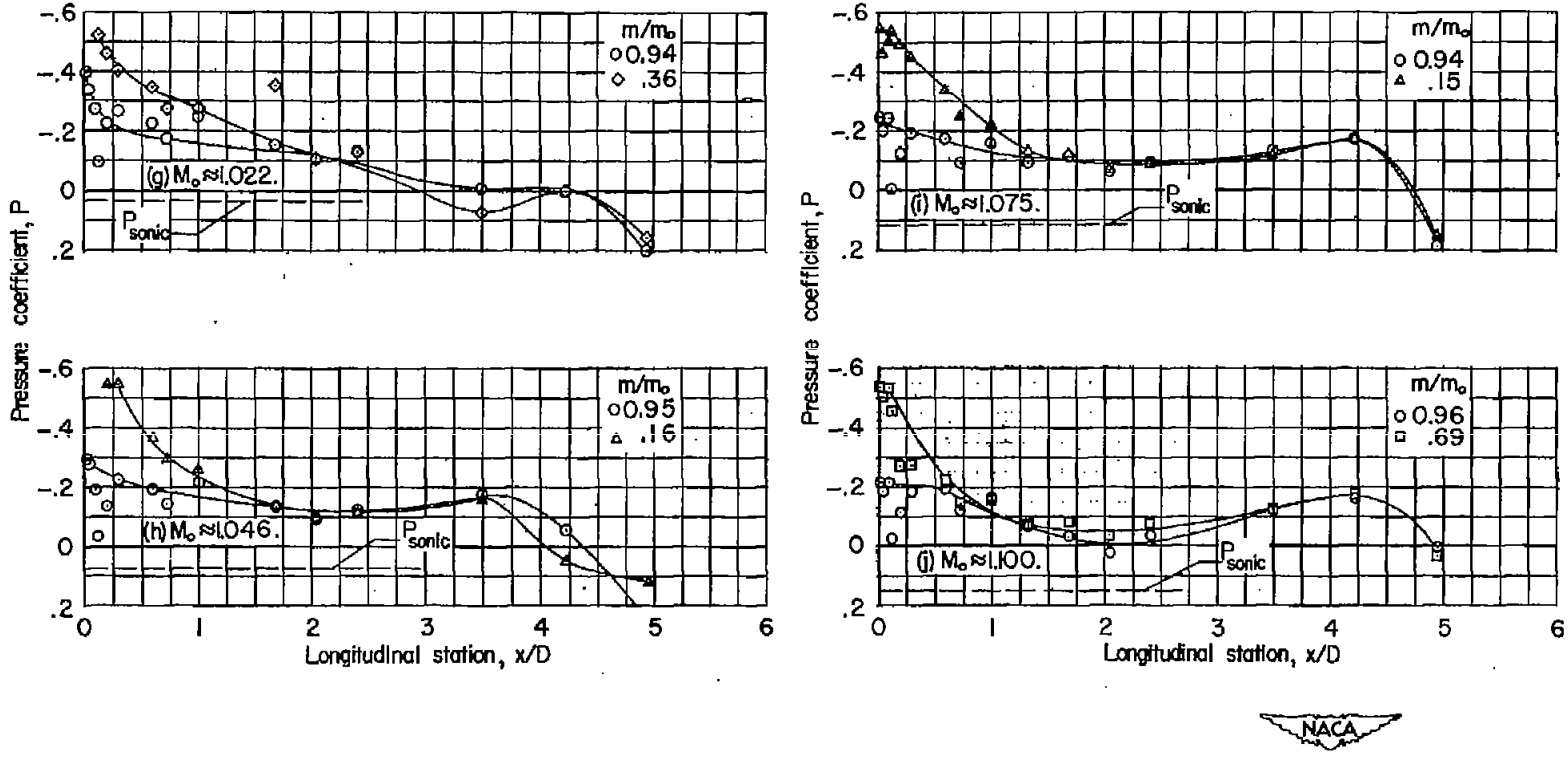

Figure 10.- Concluded.

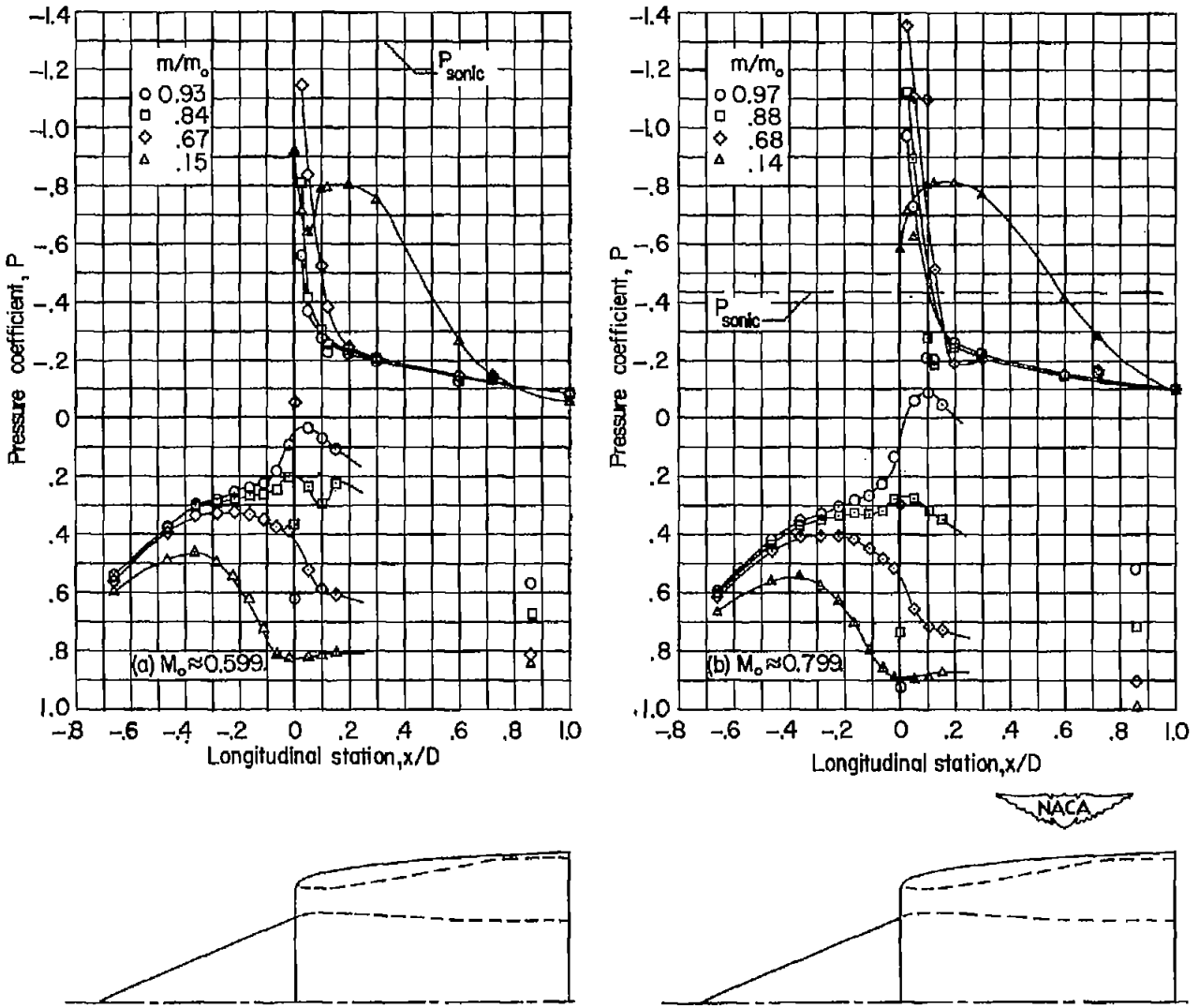

Figure 11.- Effect of mass-flow ratio on surface pressure distributions ahead of maximum-diameter station. 22° conical central body; $\alpha = 0°$.

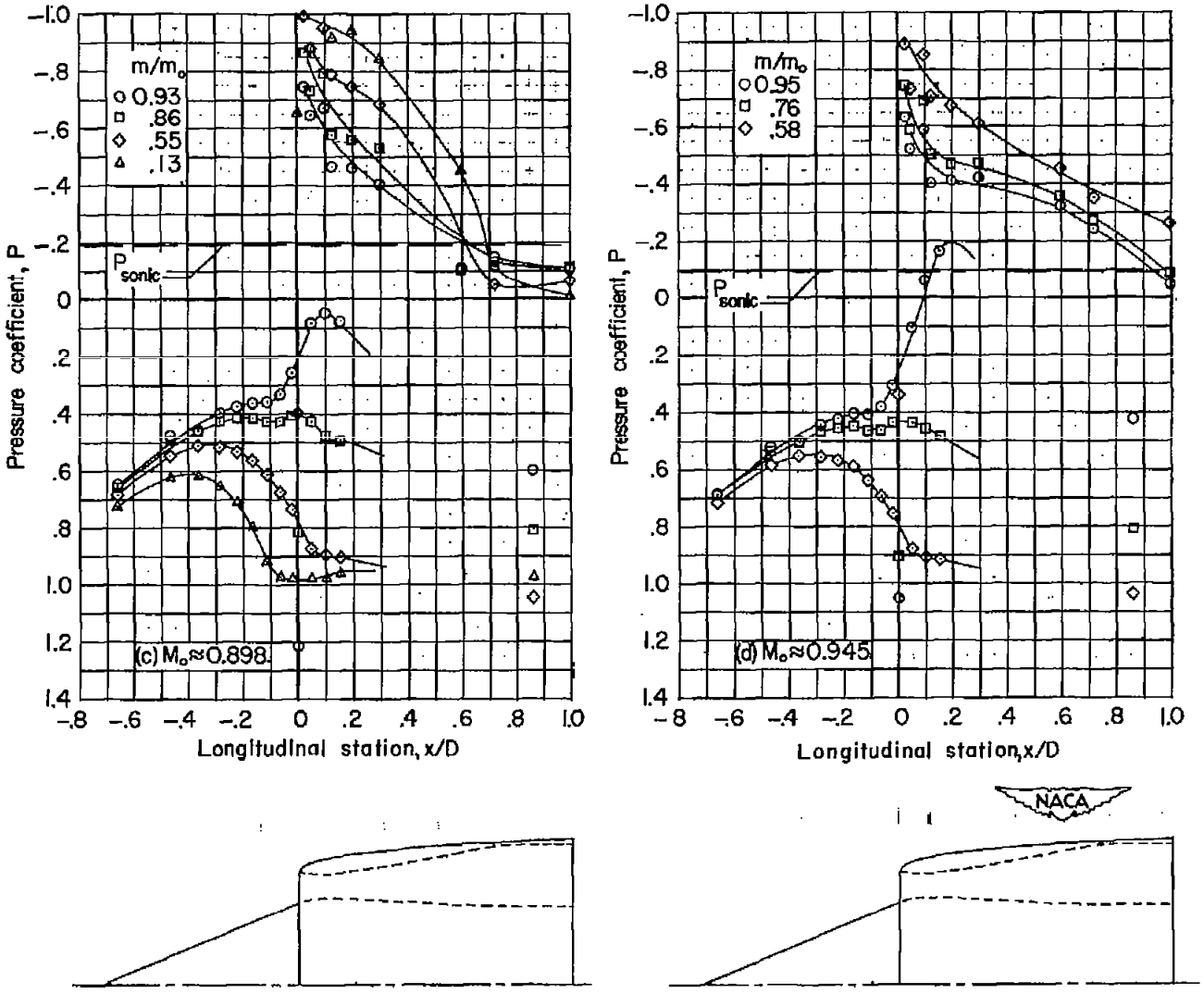

Figure 11.- Continued.

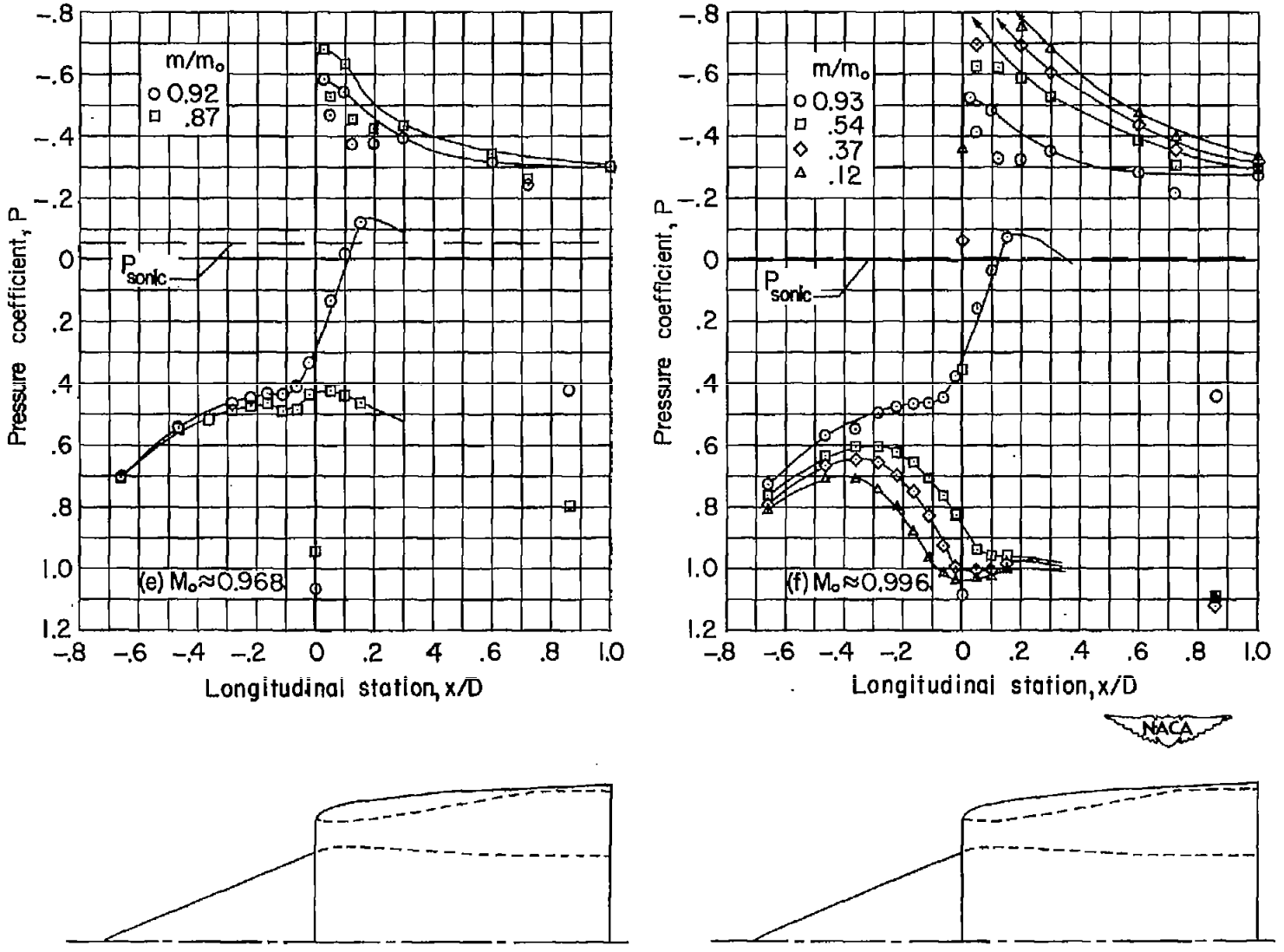

Figure 11.- Continued.

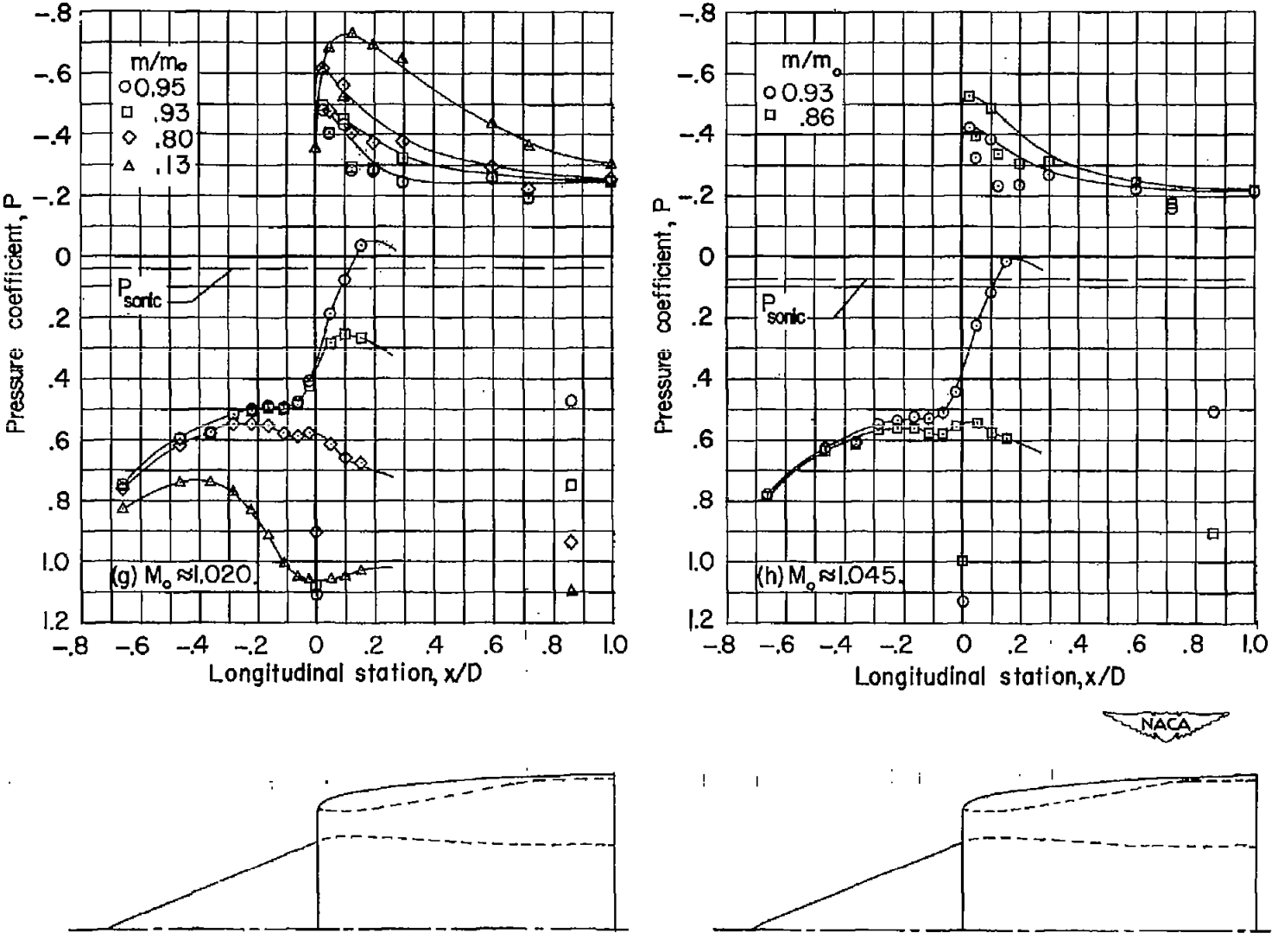

Figure 11.- Continued.

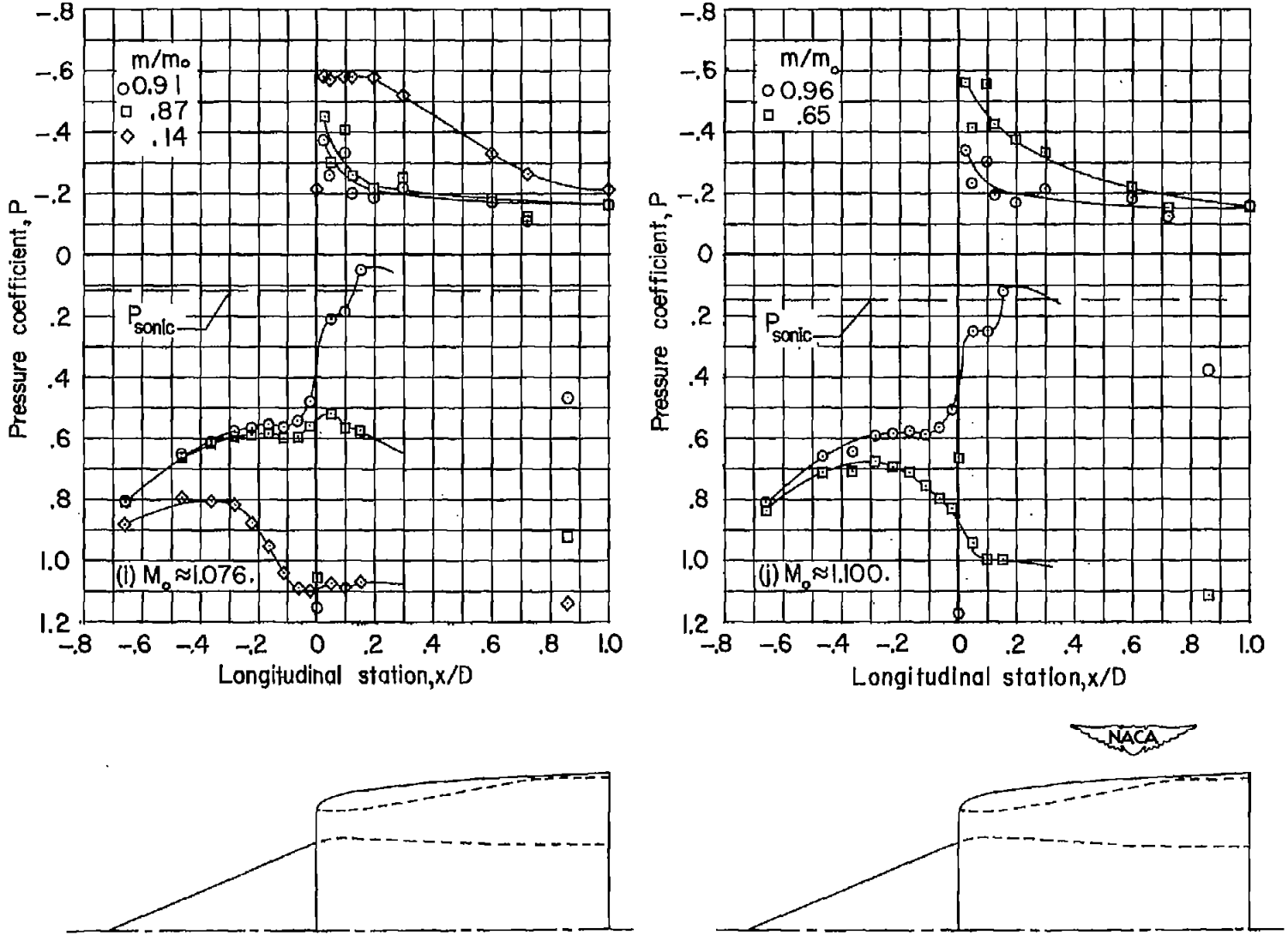

Figure 11.- Concluded.

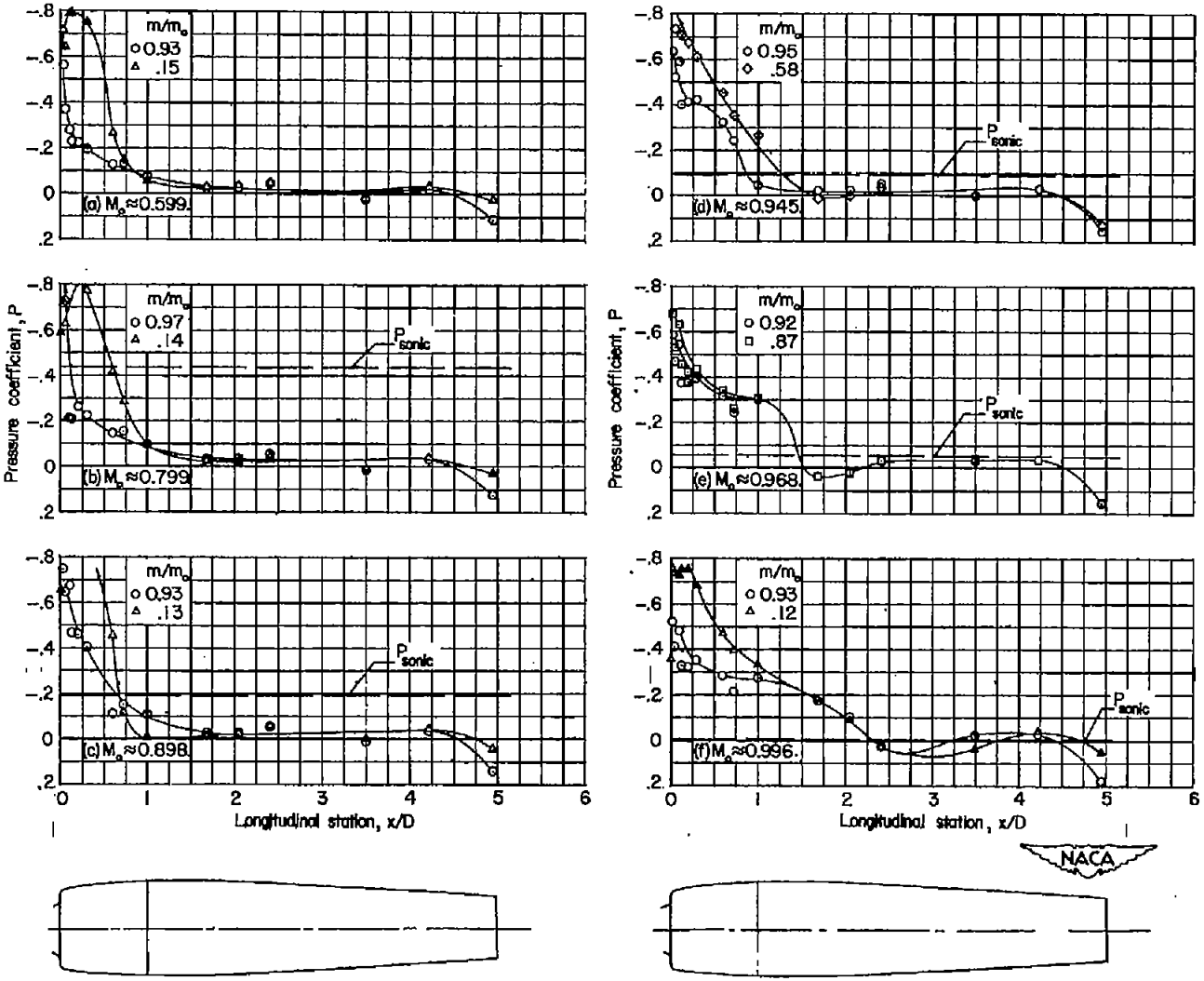

Figure 12.- Effect of mass-flow ratio on external-surface pressure distributions. 22° conical central body; $\alpha = 0°$.

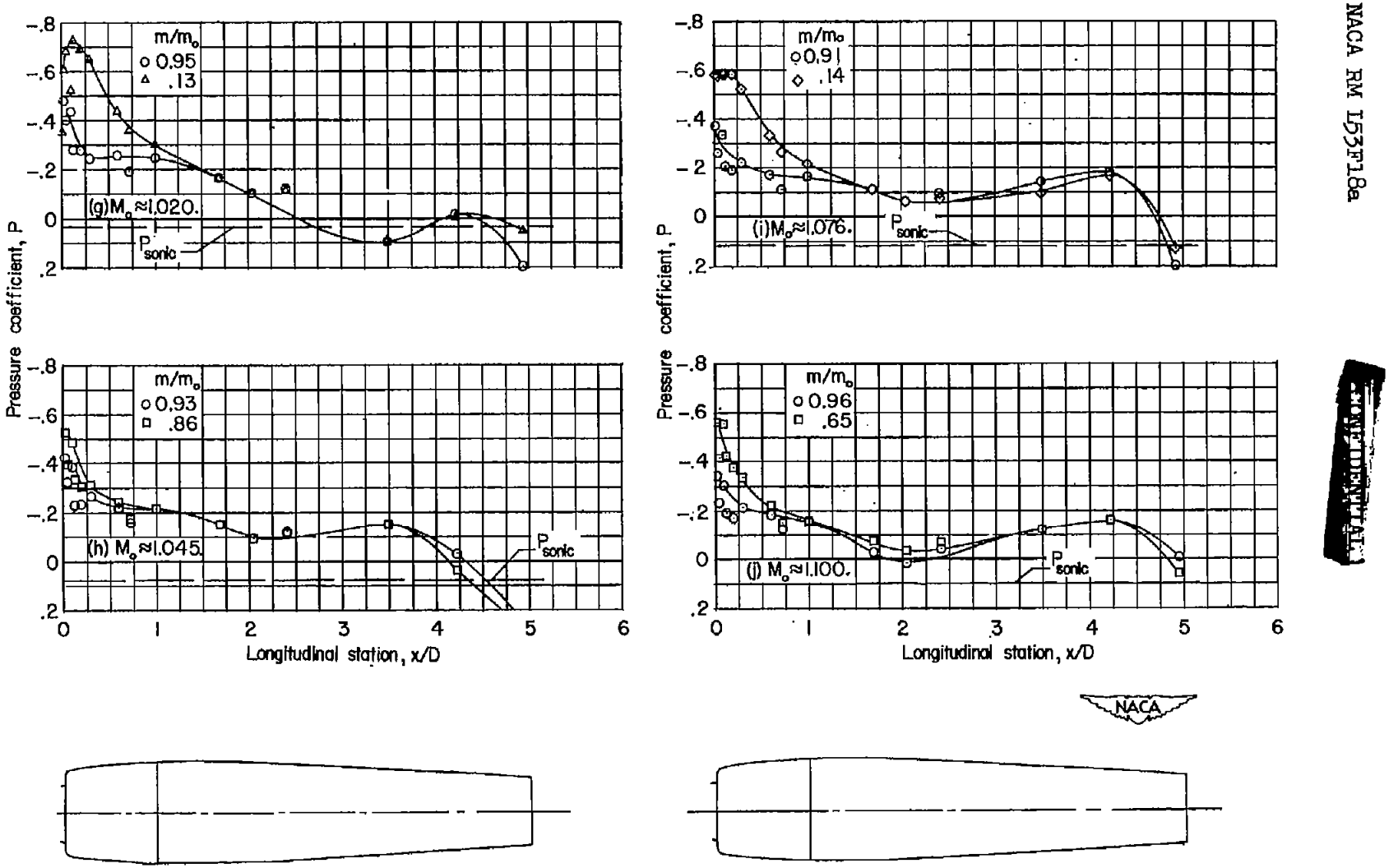

Figure 12.- Concluded.

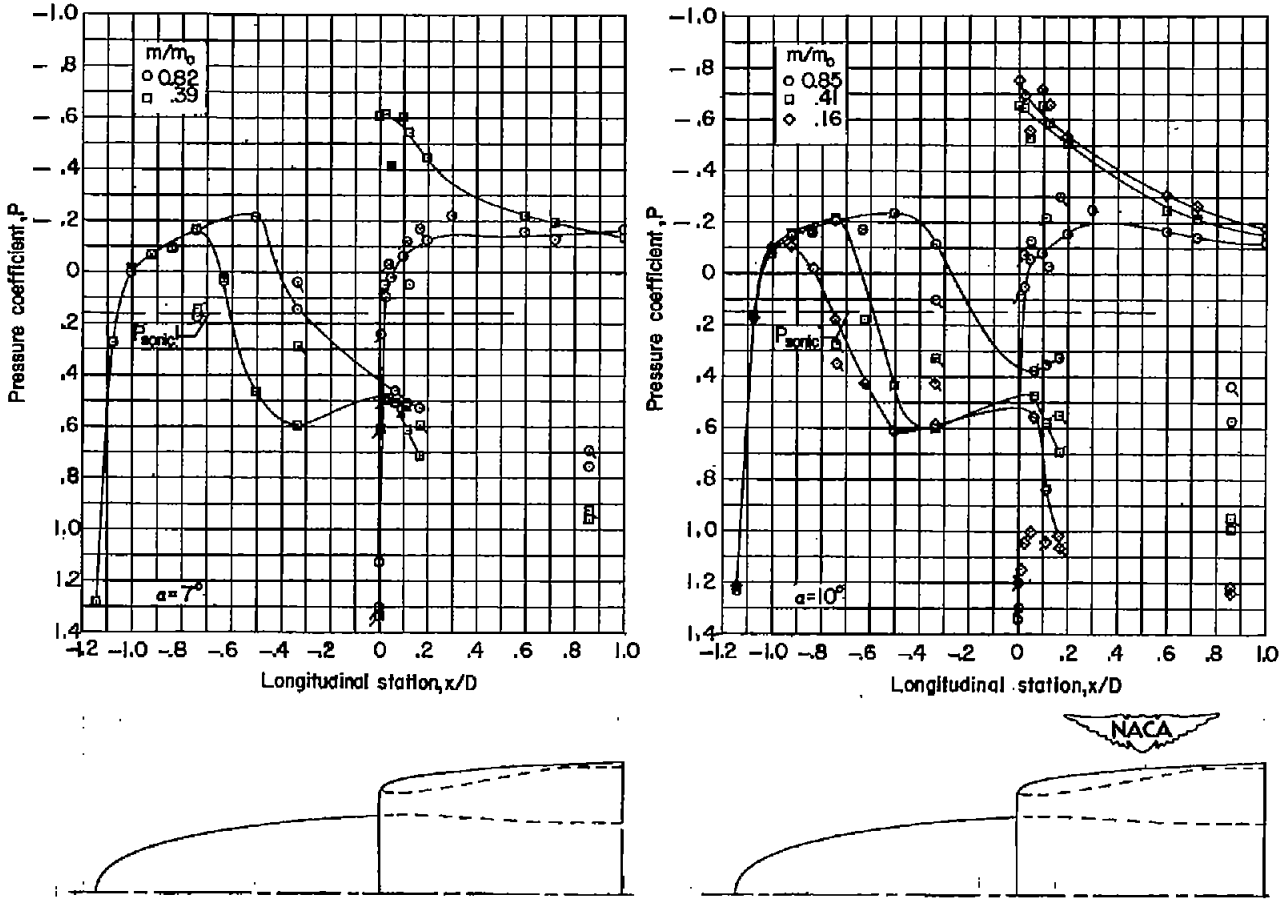

(a) $M_0 \approx 1.10$.

Figure 13.- Effect of mass-flow ratio on surface pressure distributions ahead of maximum-diameter station. Elliptical central body. Test points with flags on lower right indicate lower surface of central body. Test points with flags on upper right indicate upper inner lip. Test points with flags on lower left indicate lower inner lip.

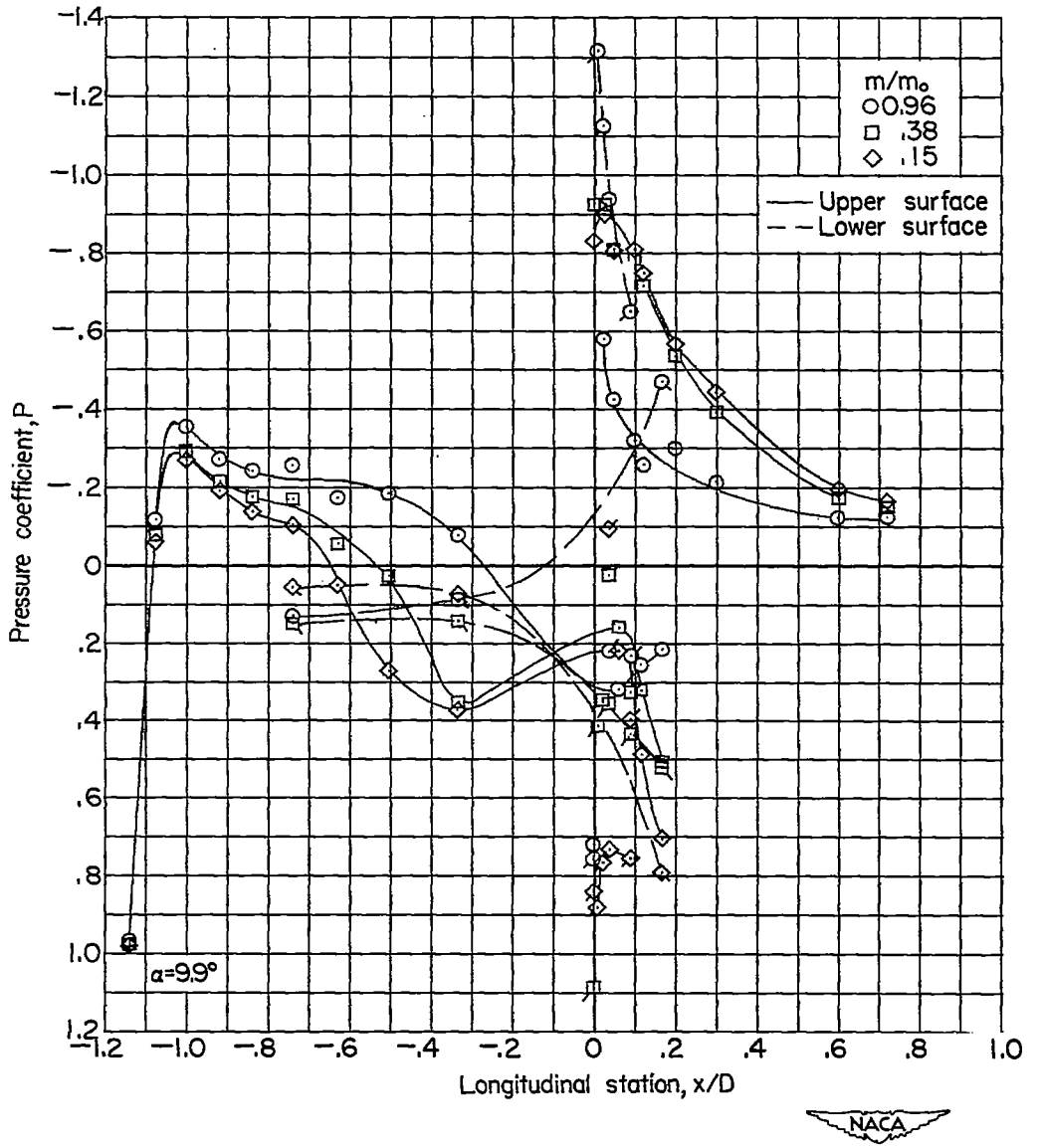

(b) $M_o \approx 0.60$.

Figure 13.- Concluded.

[redacted]

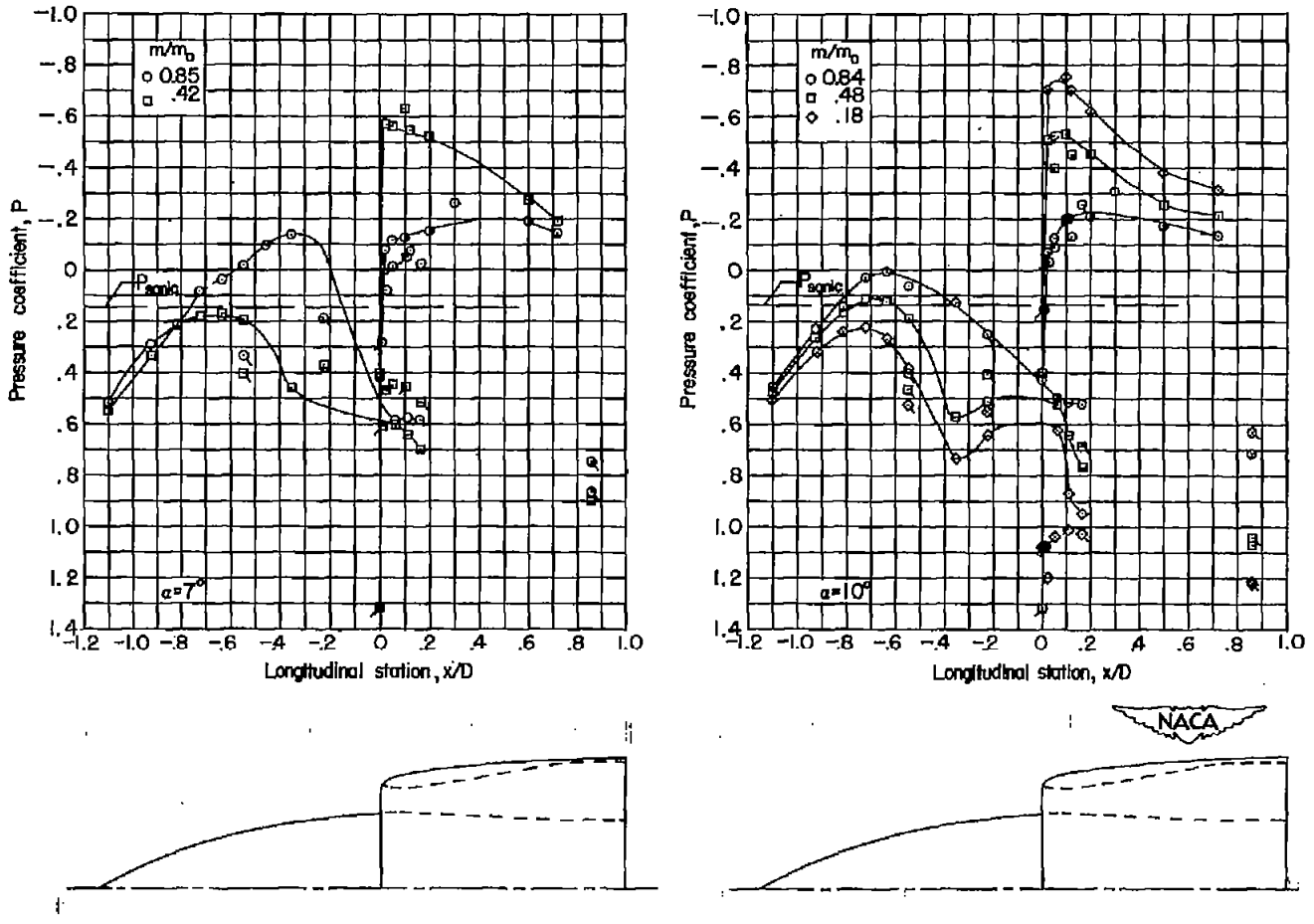

(a) $M_O \approx 1.10$.

Figure 14.- Effect of mass-flow ratio on surface pressure distributions ahead of maximum-diameter station. Parabolic central body. Test points with flags on lower right indicate lower surface of central body. Test points with flags on upper right indicate upper inner lip. Test points with flags on lower left indicate lower inner lip.

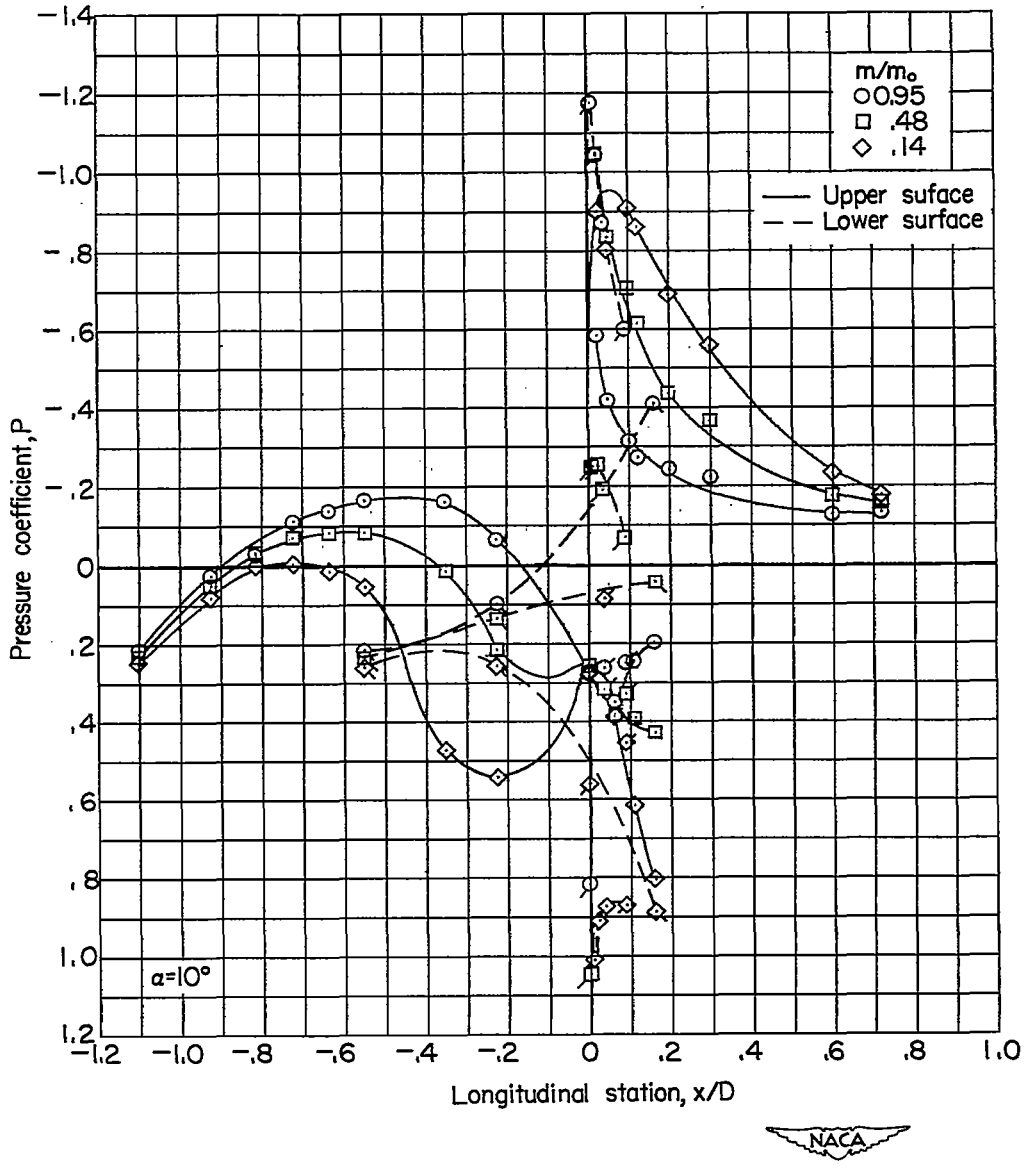

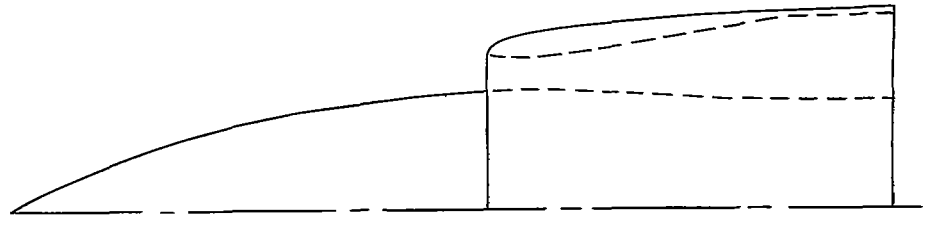

(b) $M_0 \approx 0.60$.

Figure 14.- Concluded.

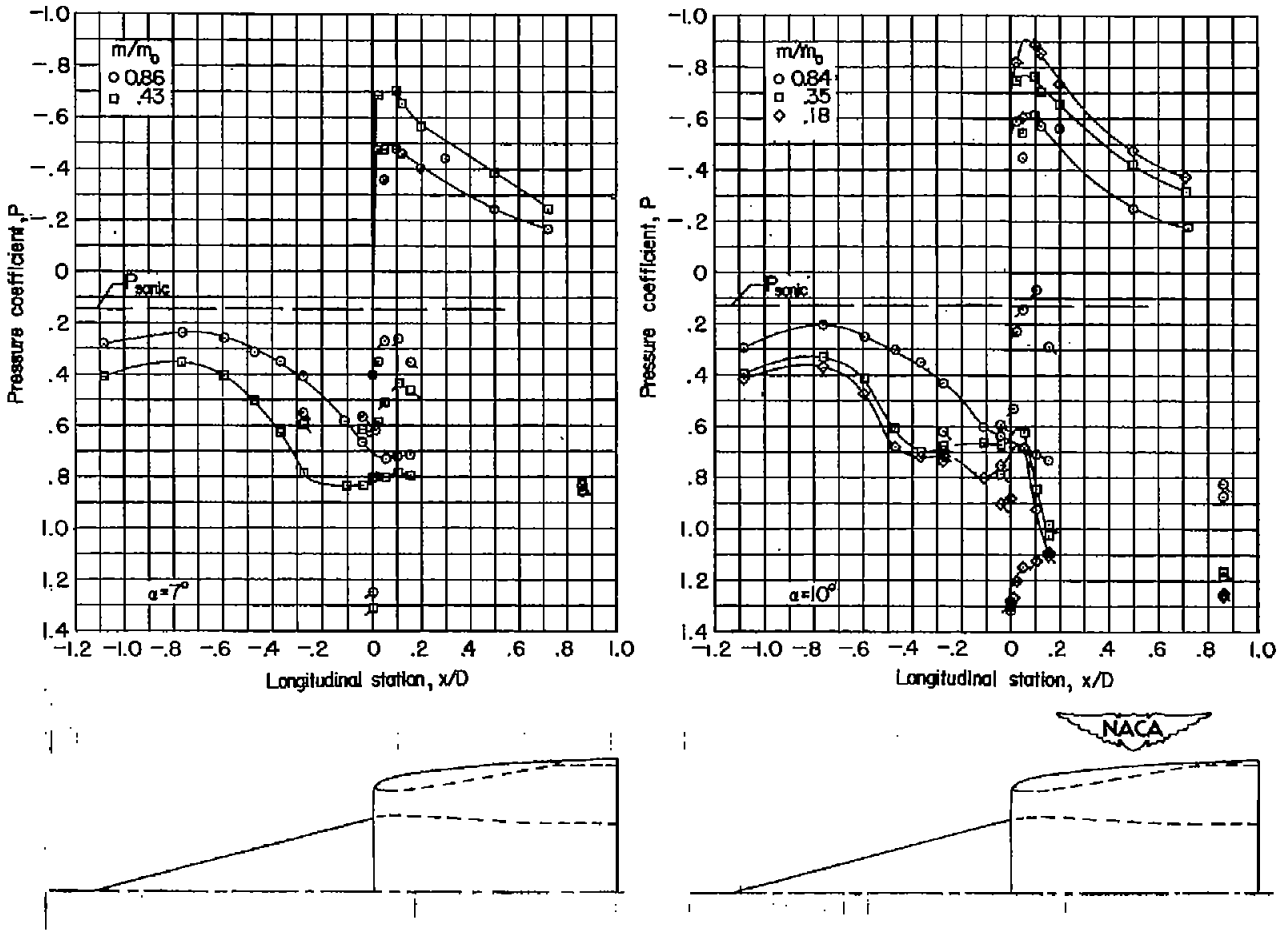

(a) $M_0 \approx 1.10$.

Figure 15.- Effect of mass-flow ratio on surface pressure distributions ahead of maximum-diameter station. 14° conical central body. Test points with flags on lower right indicate lower surface of central body. Test points with flags on upper right indicate upper inner lip. Test points with flags on lower left indicate lower inner lip.

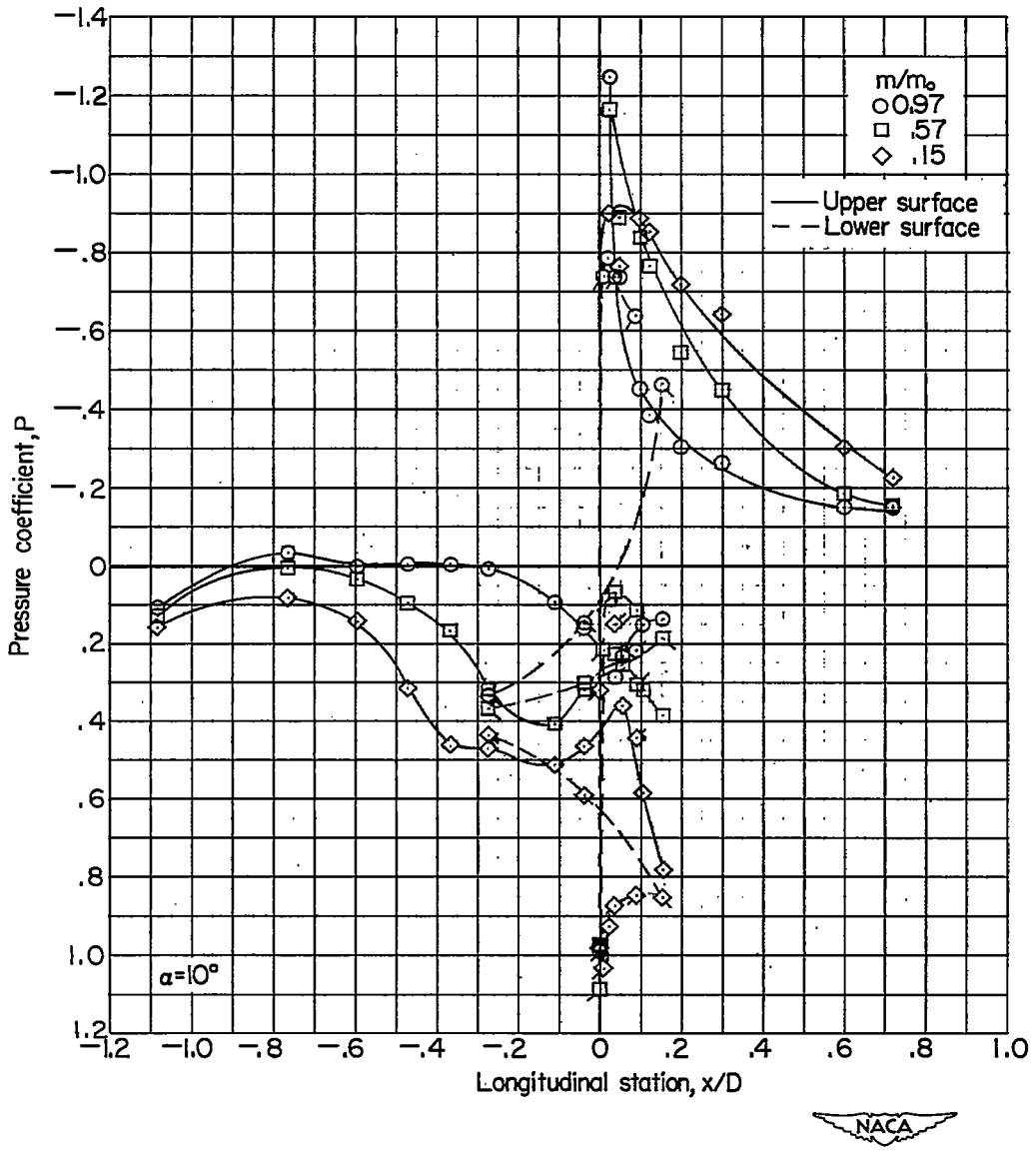

(b) $M_o \approx 0.60$.

Figure 15.- Concluded.

[redacted]

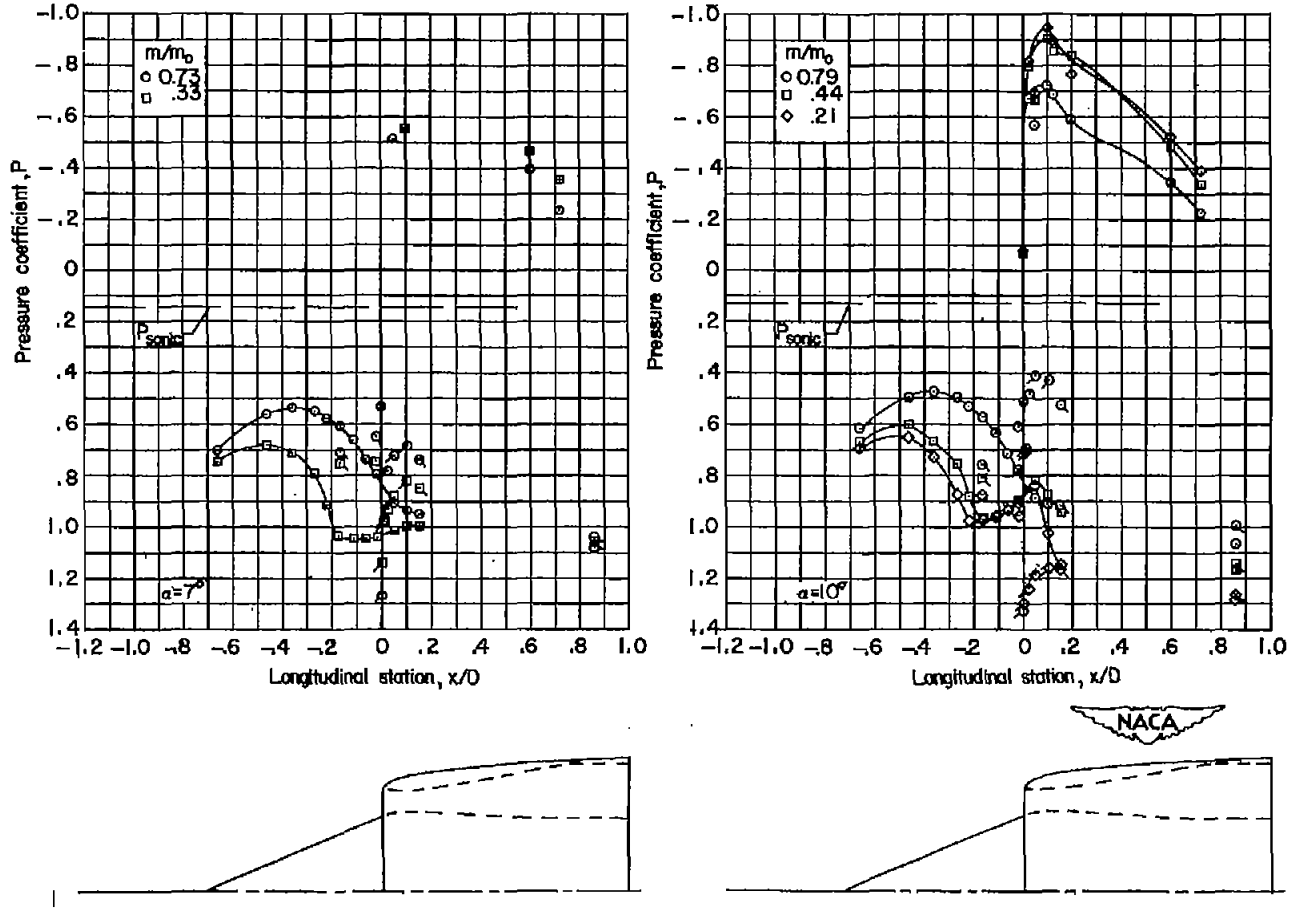

(a) $M_0 \approx 1.10$.

Figure 16.- Effect of mass-flow ratio on surface pressure distributions ahead of maximum-diameter station. 22° conical central body. Test points with flags on lower right indicate lower surface of central body. Test points with flags on upper right indicate upper inner lip. Test points with flags on lower left indicate lower inner lip.

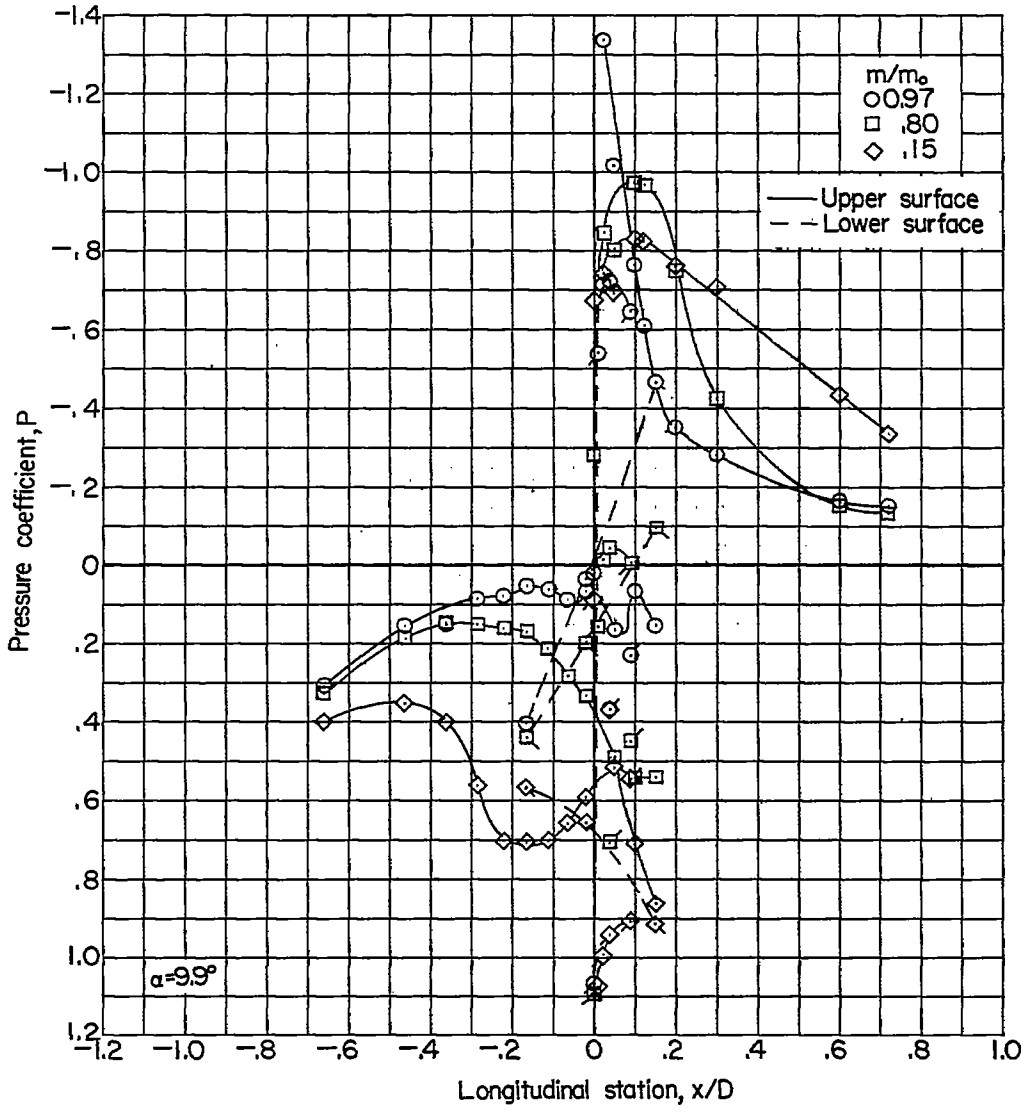

(b) $M_o \approx 0.60$.

Figure 16.- Concluded.

[redacted]

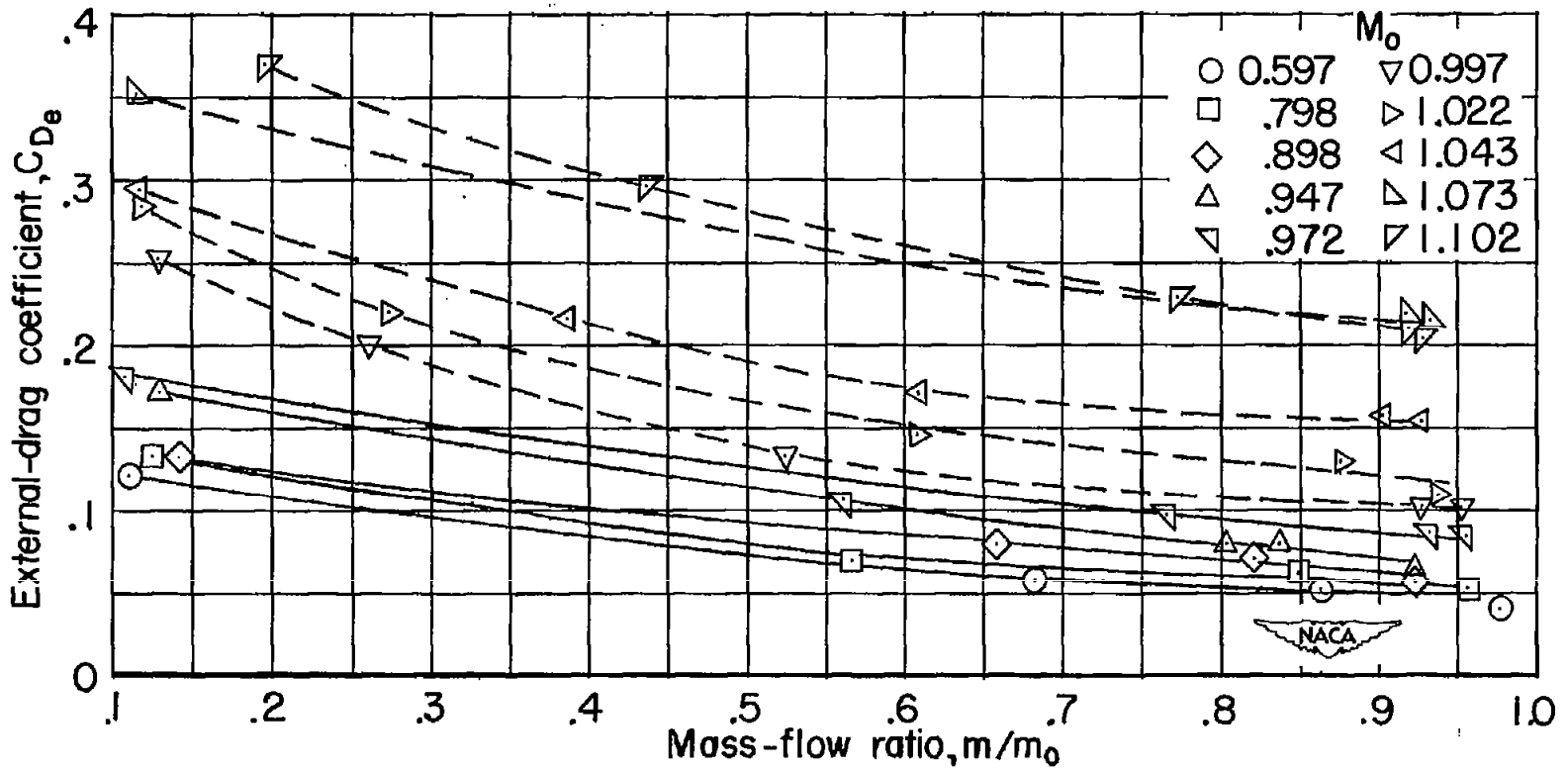

Figure 17.- Effect of mass-flow ratio on external drag coefficient. Elliptical central body; $\alpha = 0^\circ$.

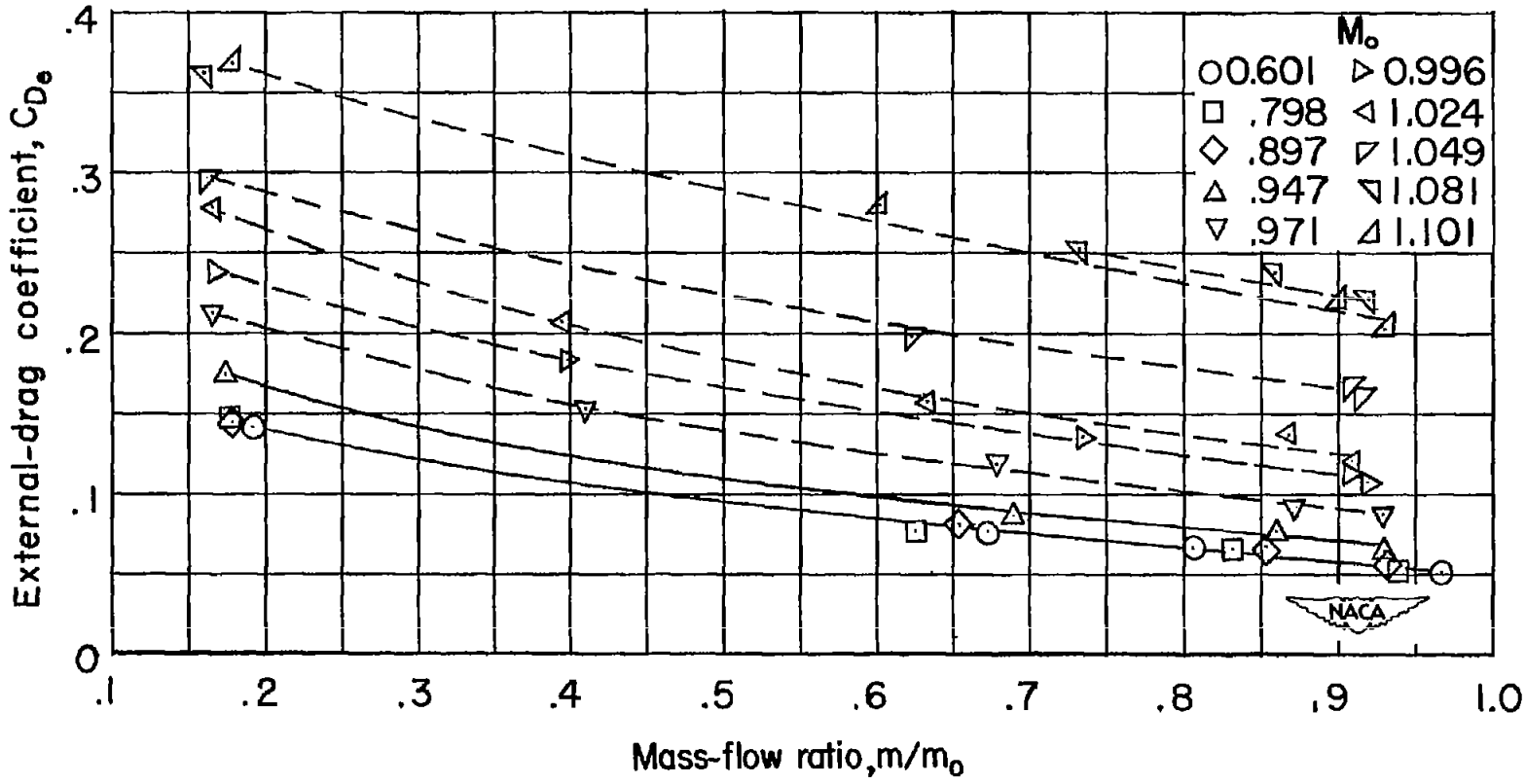

Figure 18.- Effect of mass-flow ratio on external drag coefficient. Parabolic central body; $\alpha = 0^\circ$.

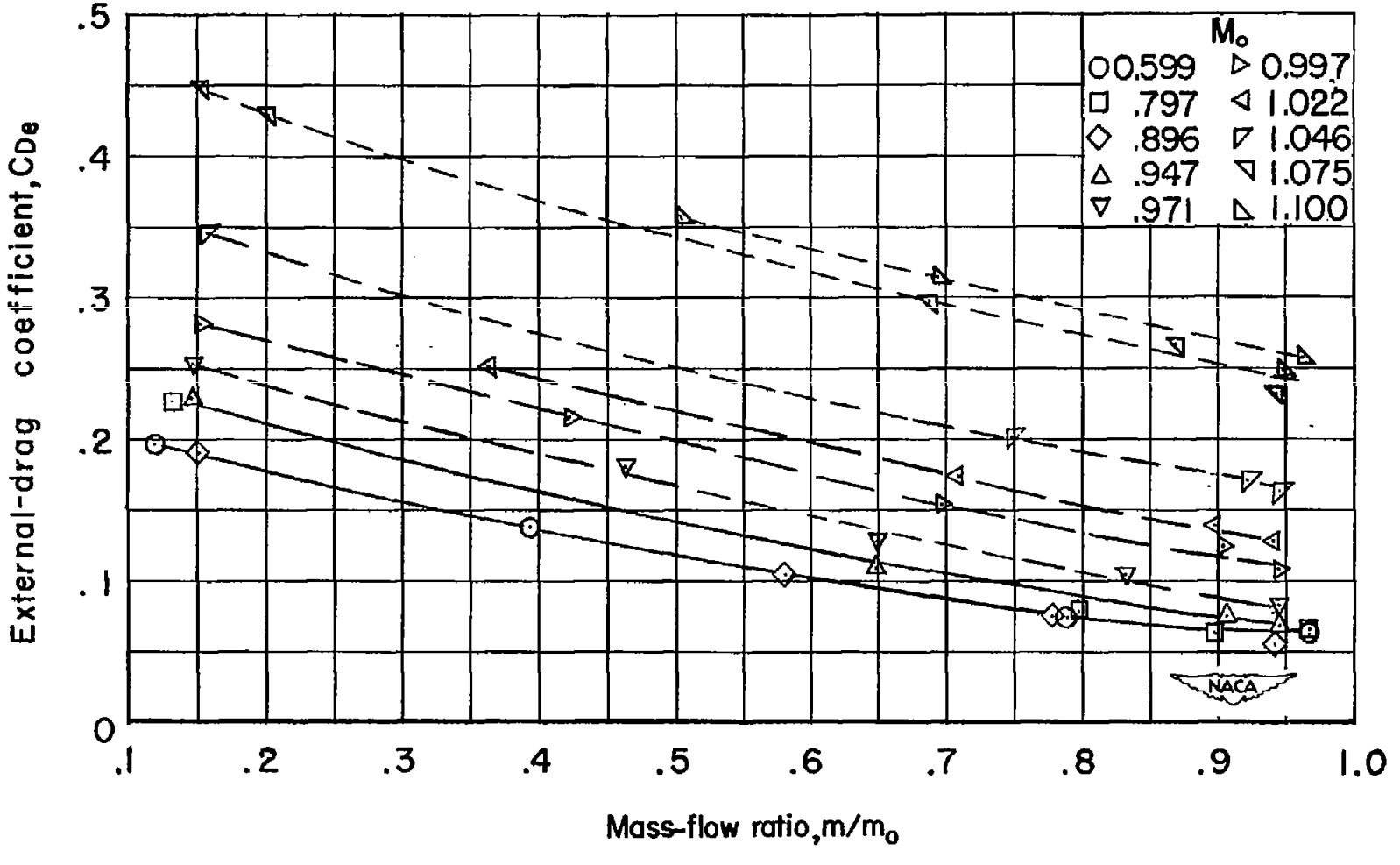

Figure 19.- Effect of mass-flow ratio on external drag coefficient. 14° conical central body; $\alpha = 0°$.

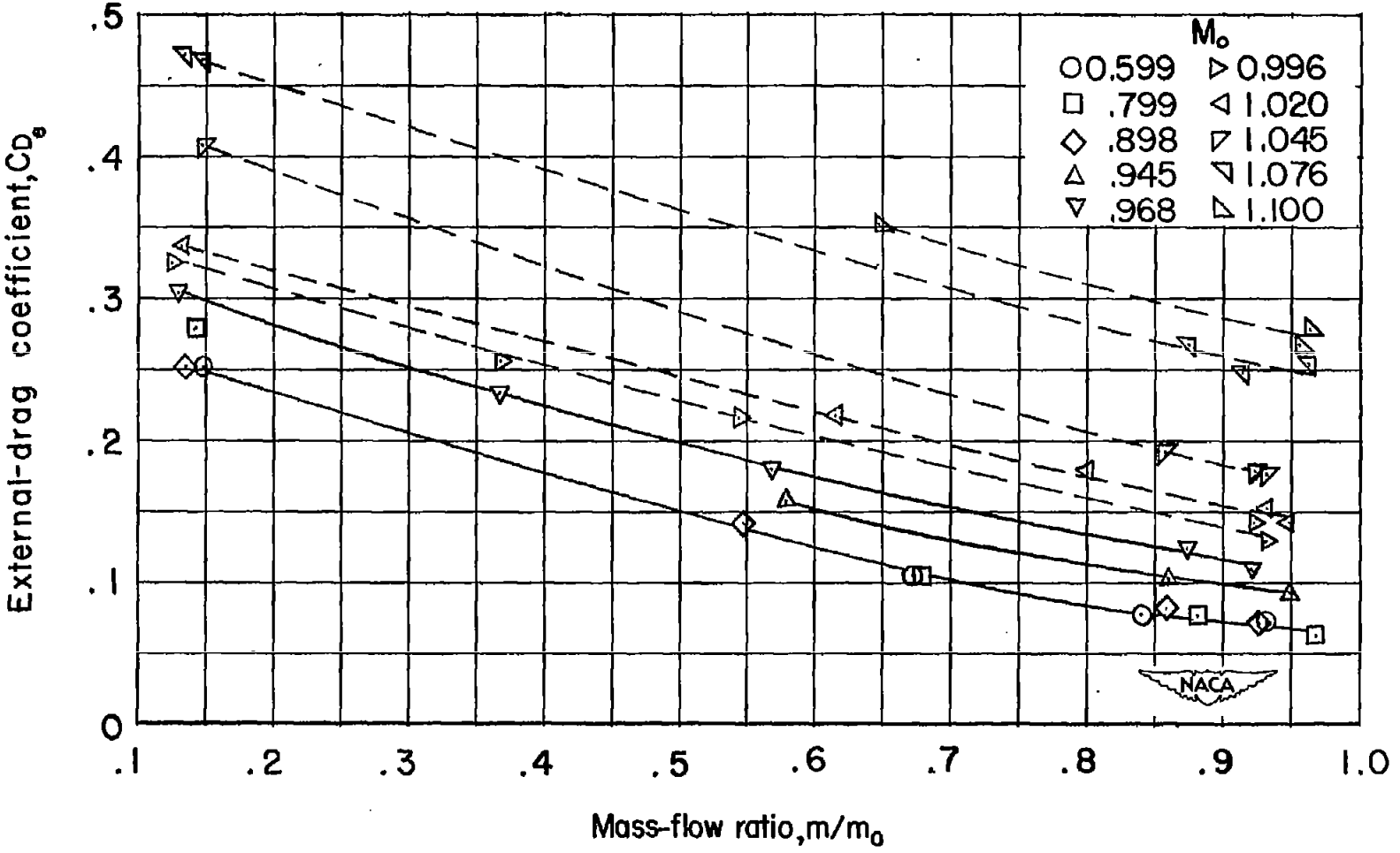

Figure 20.- Effect of mass-flow ratio on external drag coefficient. 22° conical central body; $\alpha = 0°$.

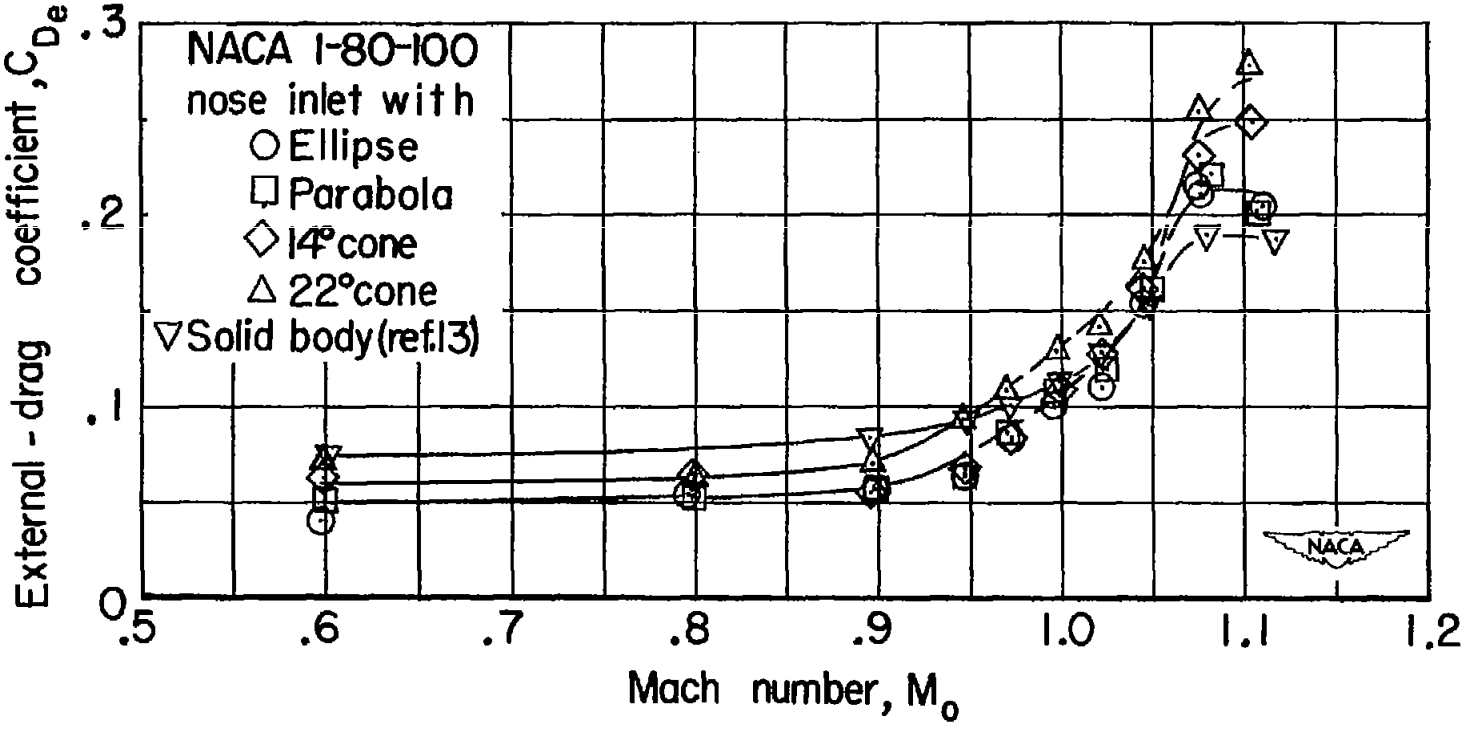

Figure 21.- Comparison of Mach number effects on external drag coefficients of various configurations. $\alpha = 0^\circ$; maximum test mass-flow ratio.

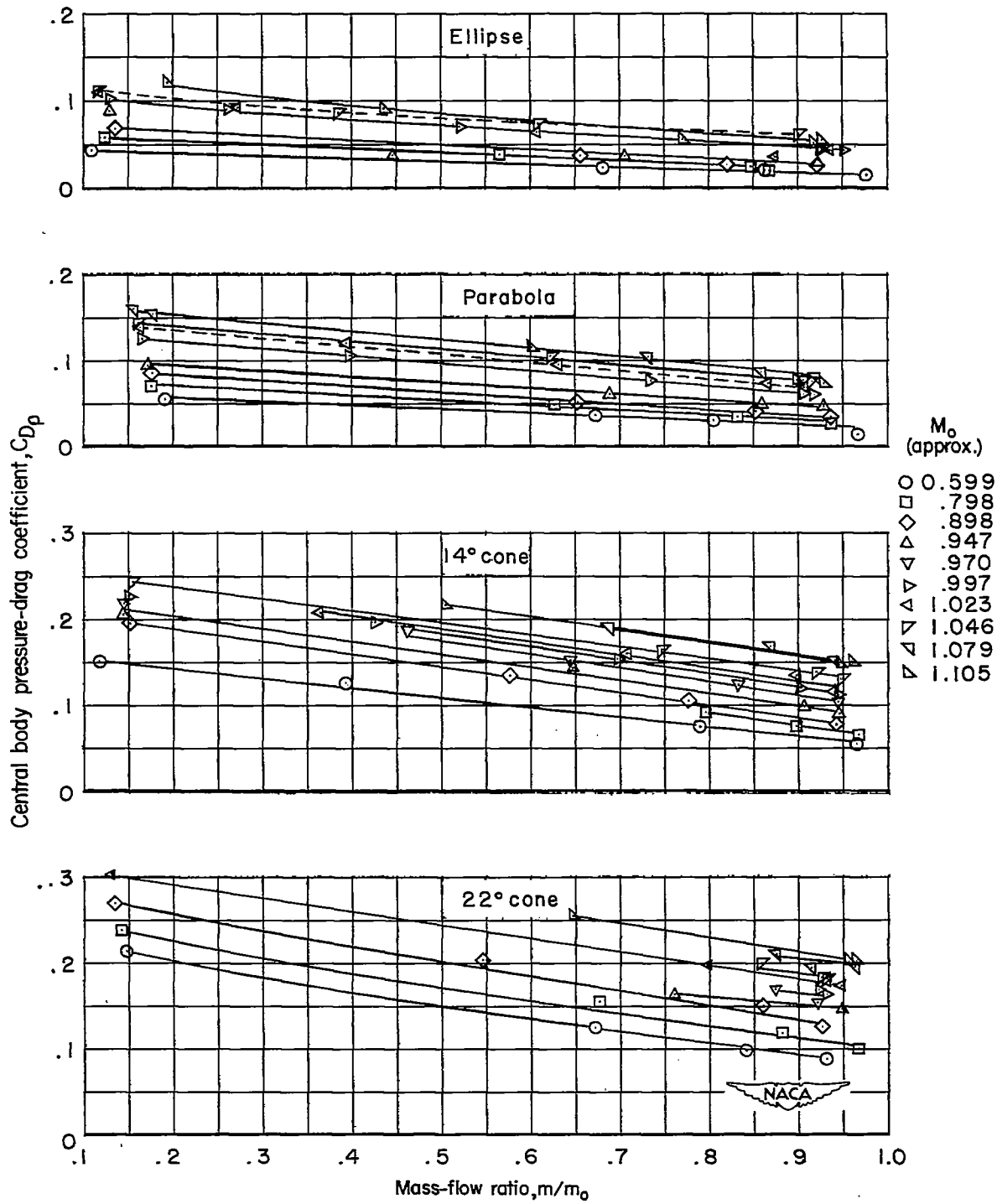

Figure 22.- Effect of mass-flow ratio on central-body-pressure-drag coefficient. $\alpha = 0^\circ$.

[redacted]

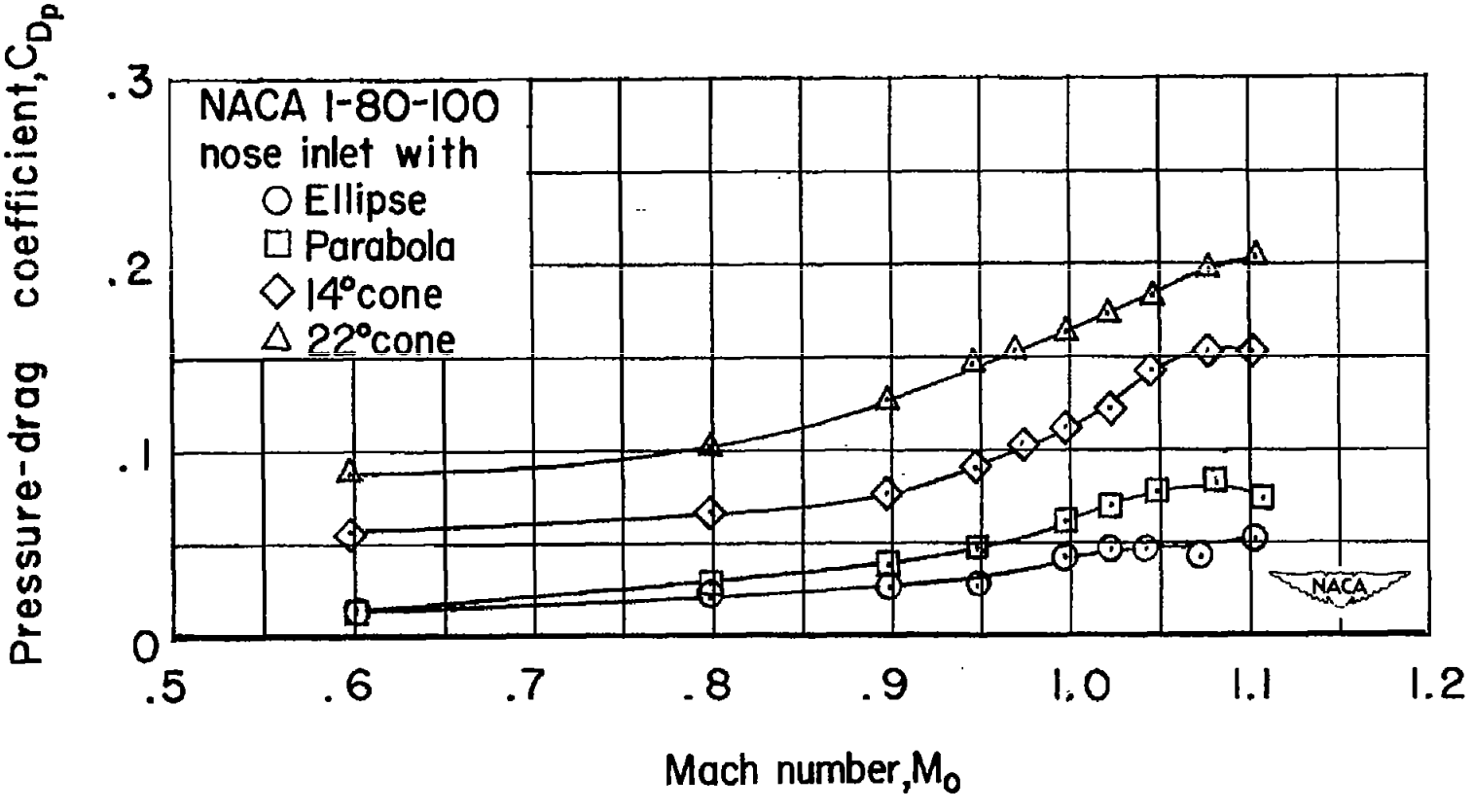

Figure 23.- Comparison of effects of Mach number on the central-body-pressure-drag coefficient. $\alpha = 0^\circ$; maximum test m/m_o.

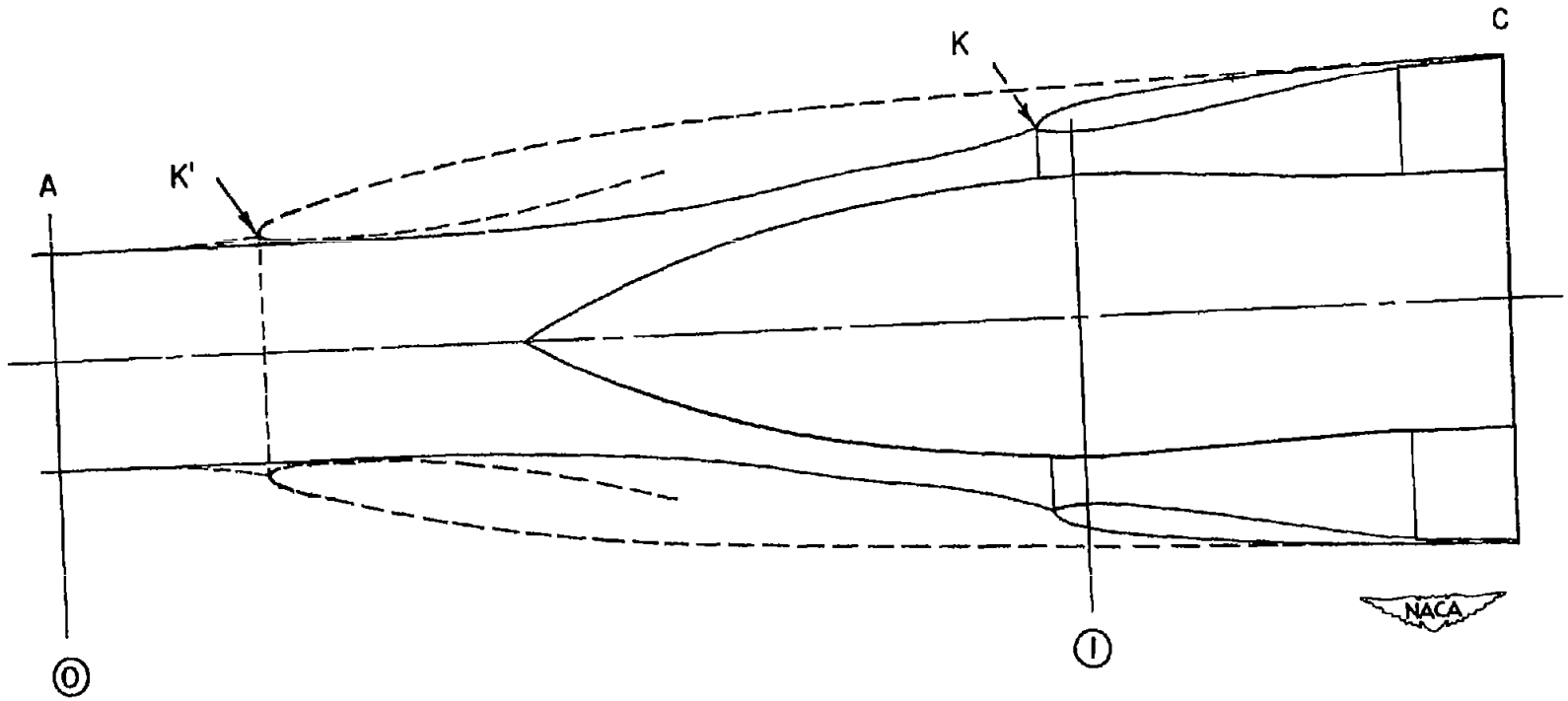

Figure 24.- Diagram of entering stream tube of an open-nose- and an annular-inlet configuration.

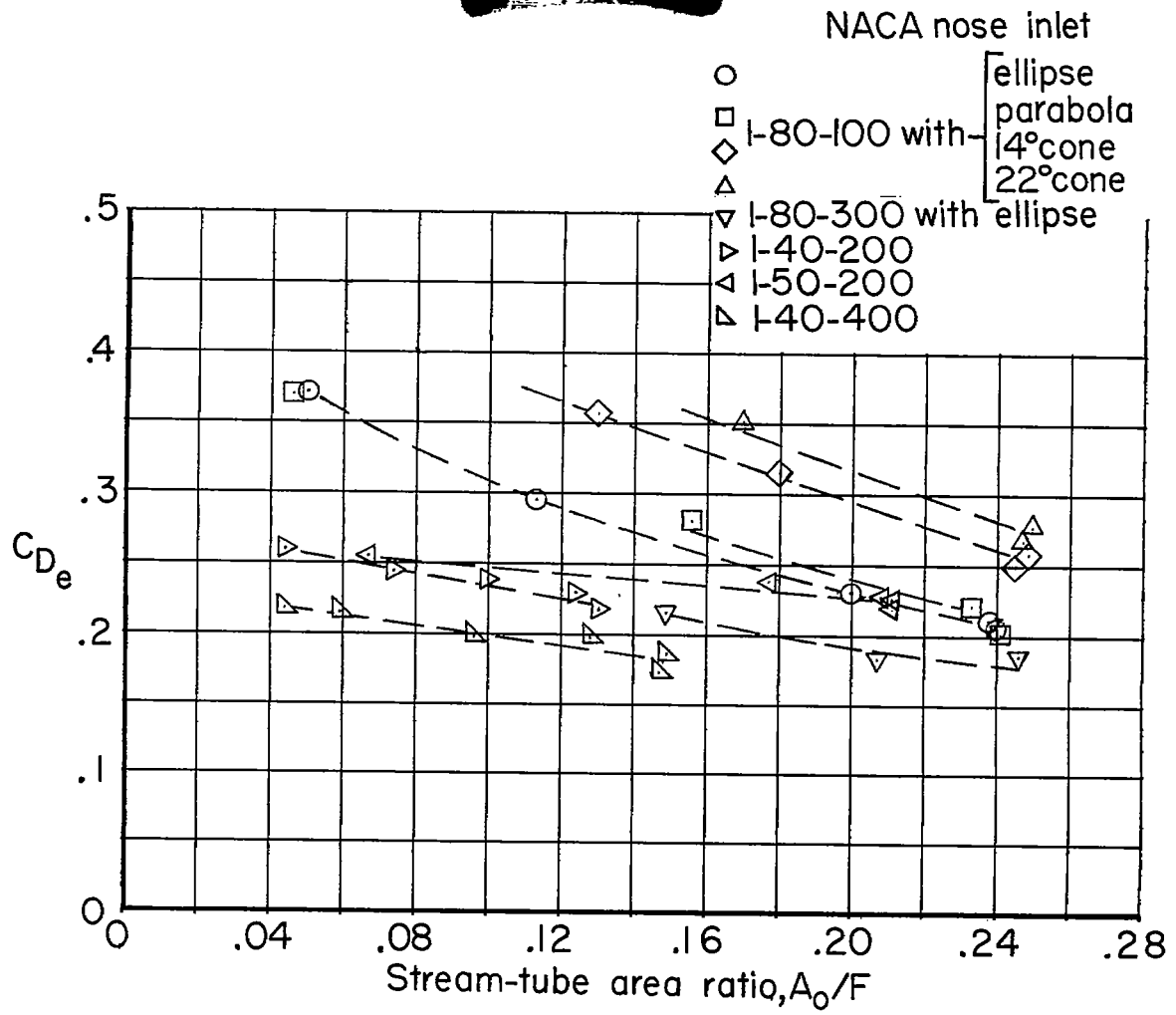

(a) External drag.

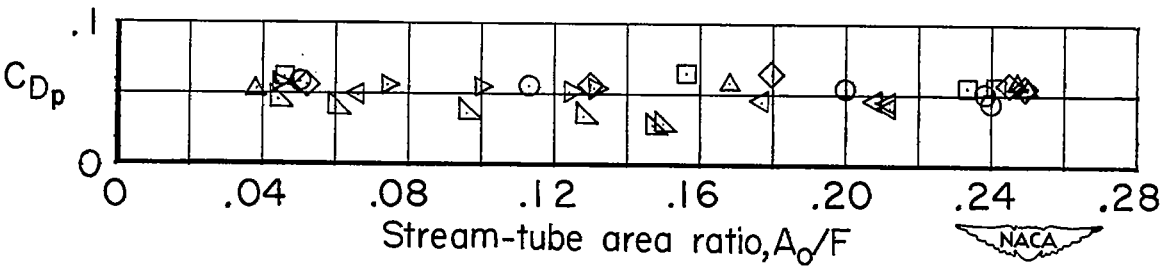

(b) Afterbody pressure drag.

Figure 25.- Comparison of effects of variations of stream-tube-area ratio on drag coefficients. $M_o \approx 1.10$; $\alpha = 0°$.

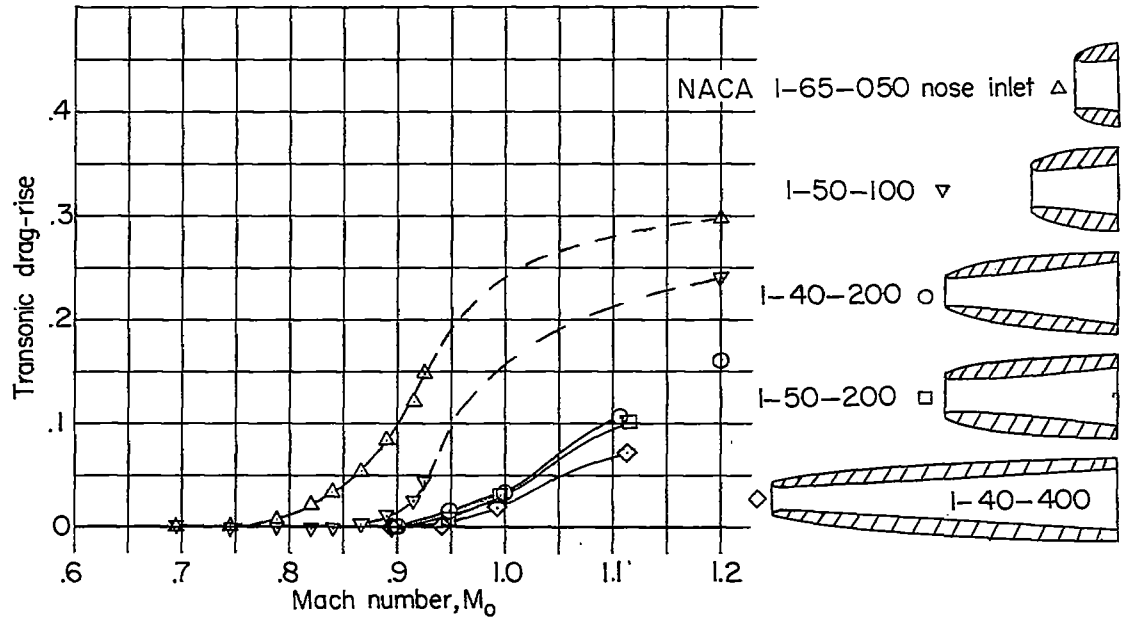

(a) Transonic drag-rise curves.

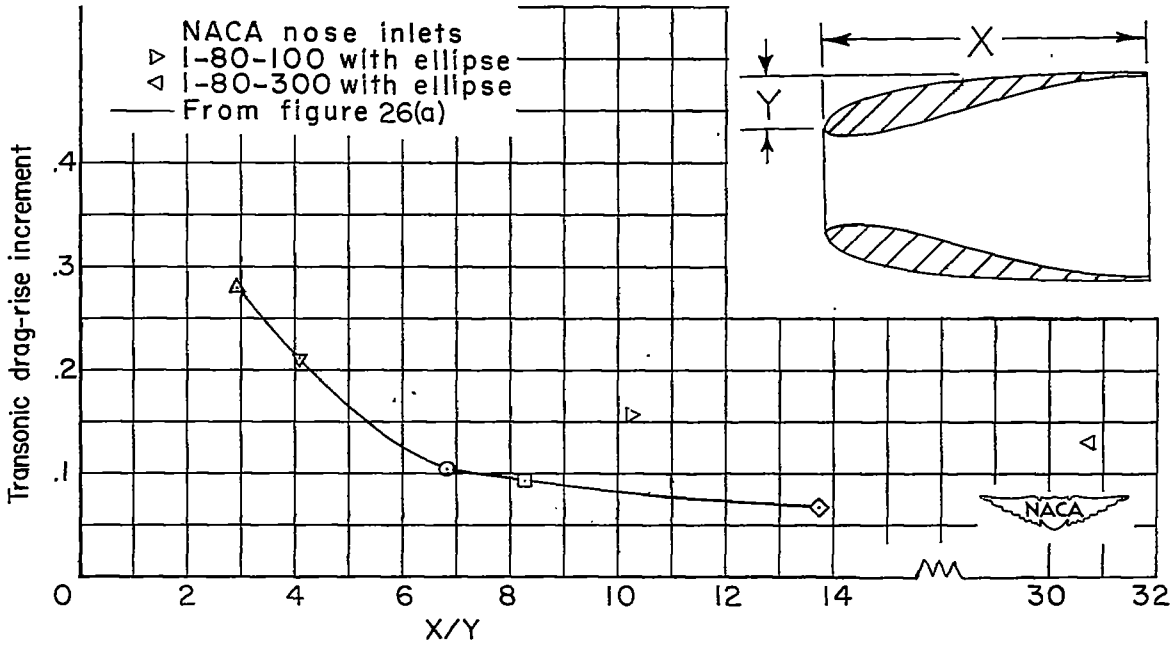

(b) Drag-rise increment for $M_o \approx 1.10$.

Figure 26.- Comparison of transonic drag rise. Inlet choked; $\alpha = 0^\circ$.

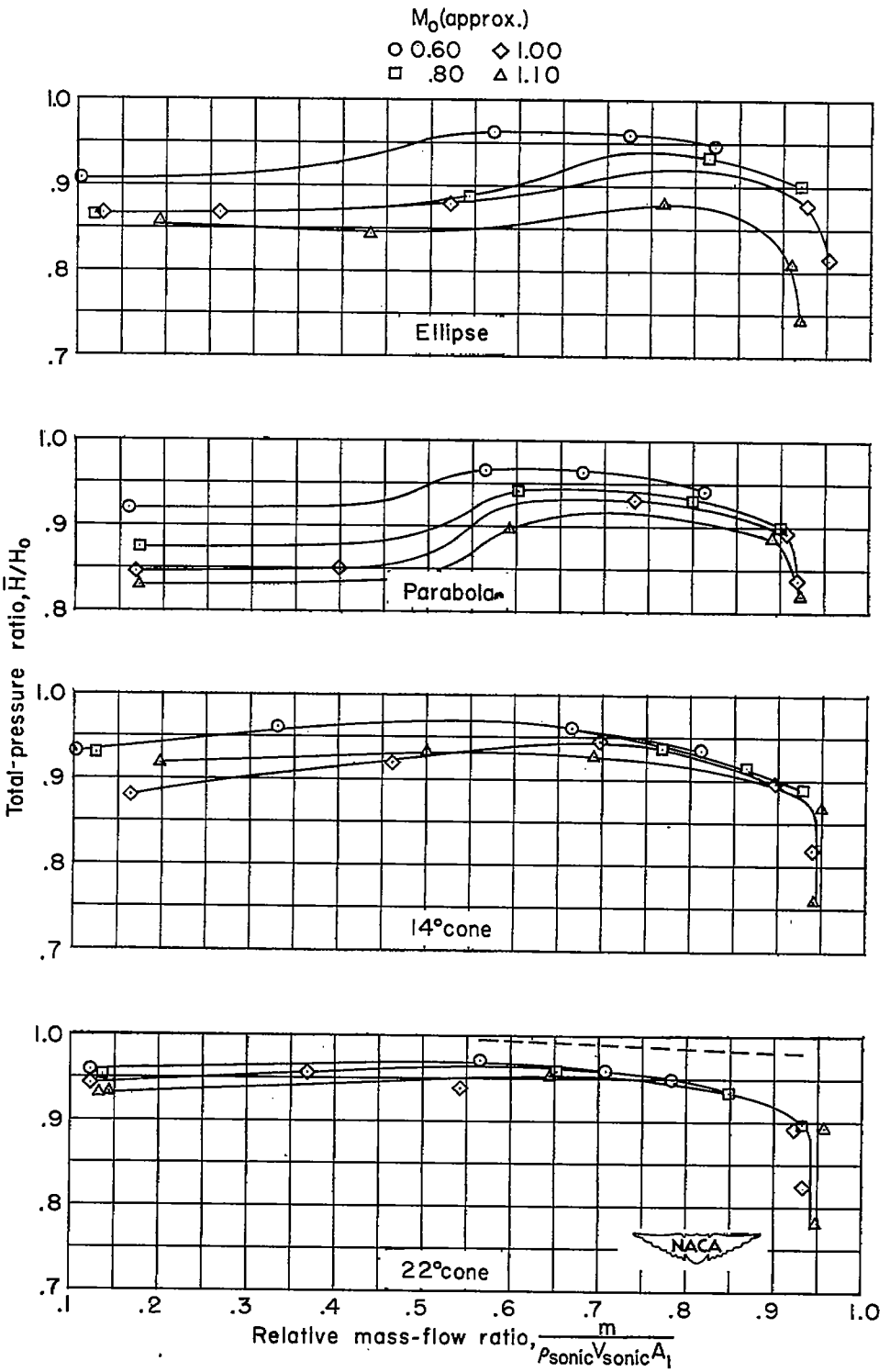

Figure 27.- Effects of relative mass-flow ratio and Mach number on total-pressure ratio. $\alpha = 0^\circ$.

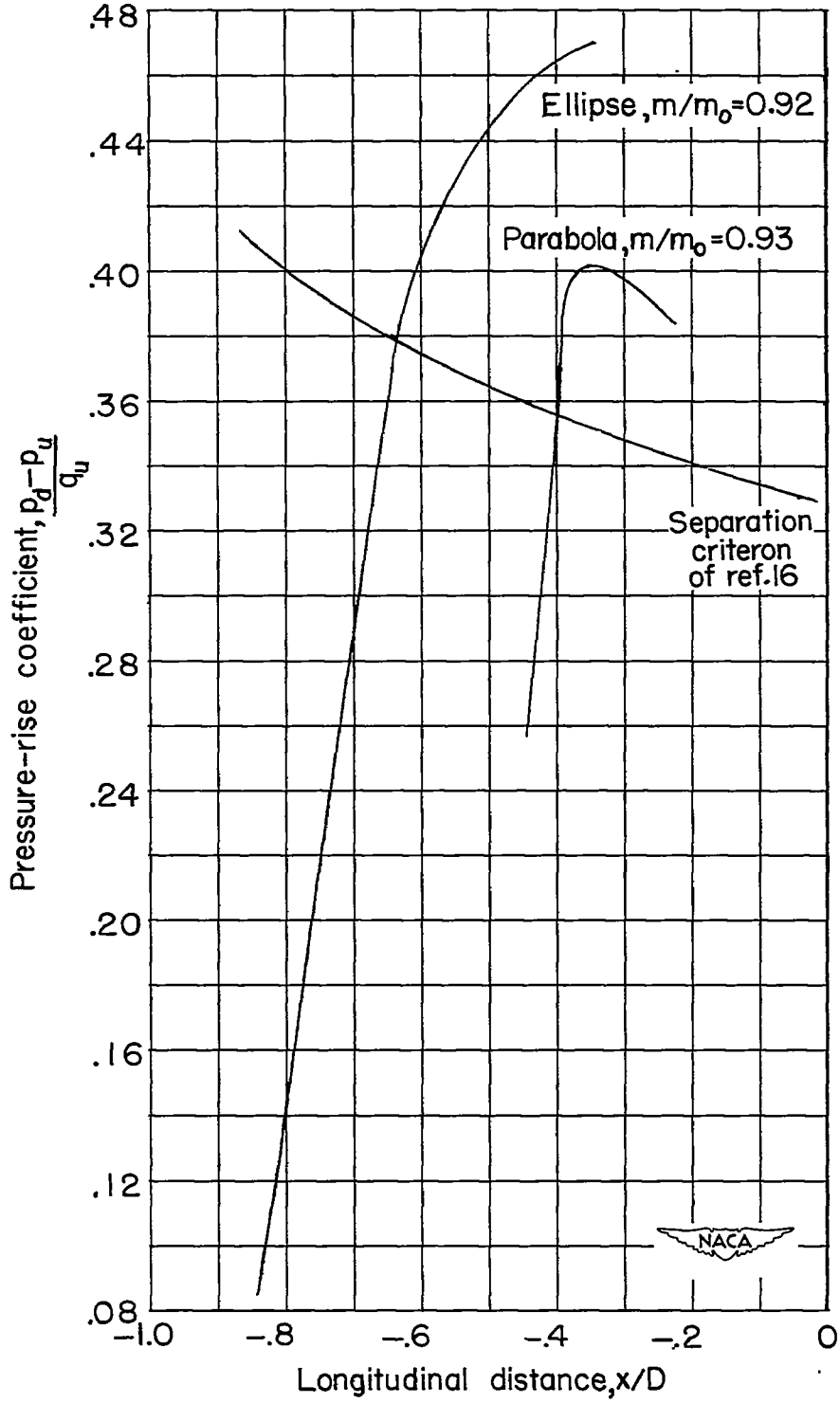

Figure 28.- Calculated pressure rise through a normal shock as a function of assumed shock position along the central body. $M_0 \approx 1.1$.

[redacted]

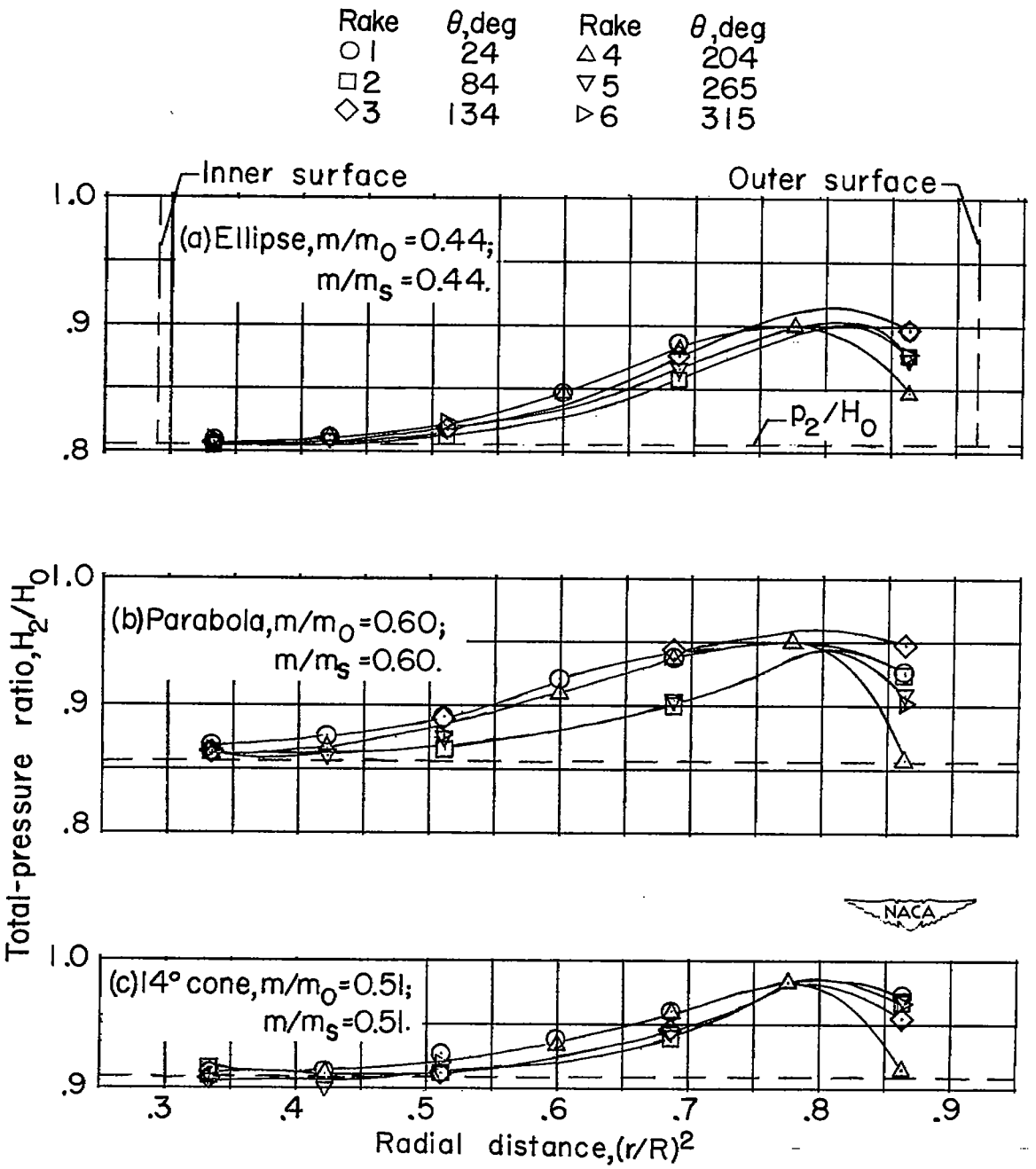

Figure 29.- Variation of total-pressure ratio with radial distance. $M_o \approx 1.10$; $\alpha = 0^\circ$.

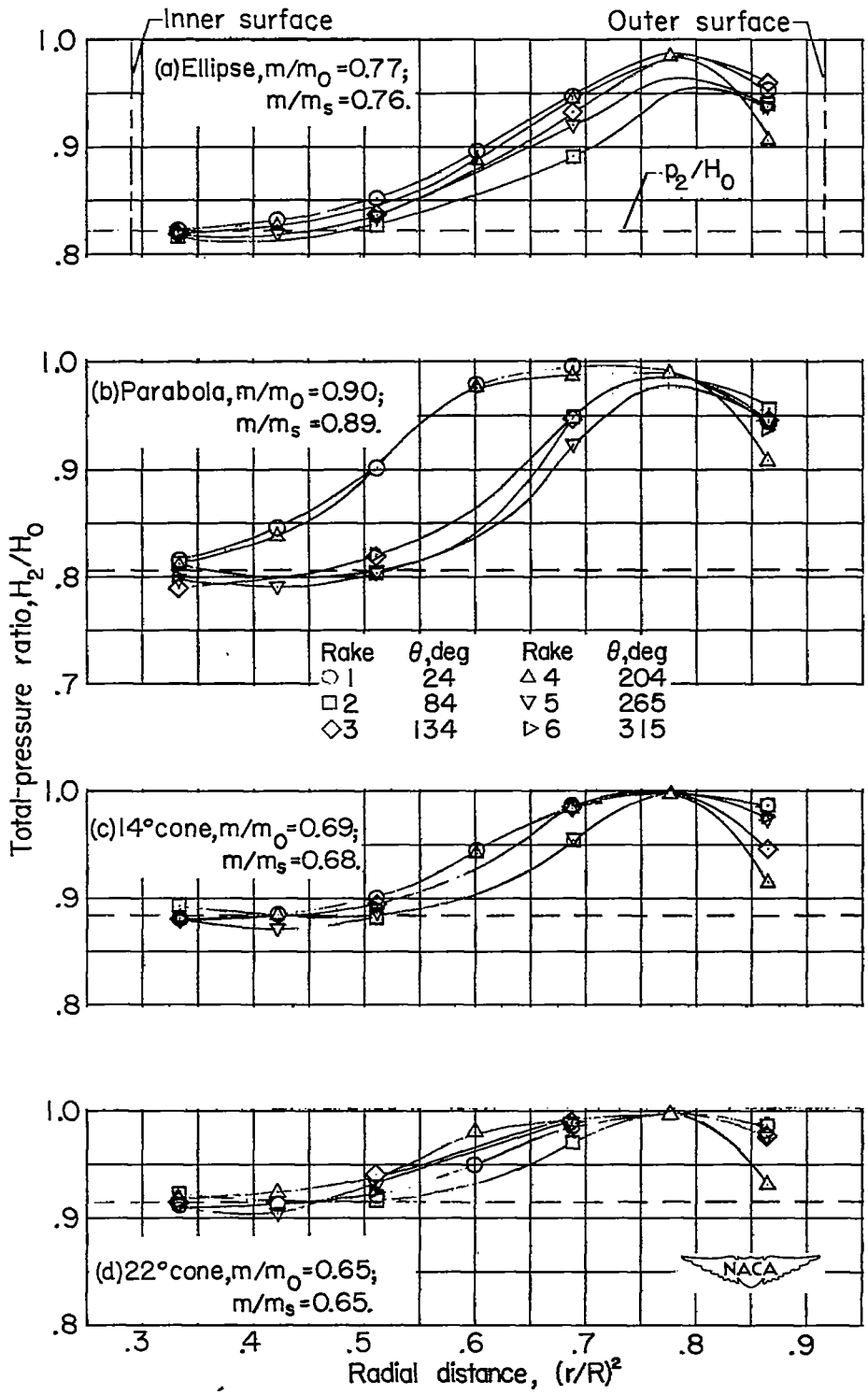

Figure 30.- Variation of total-pressure ratio with radial distance. $M_0 \approx 1.10$; $\alpha = 0^\circ$.

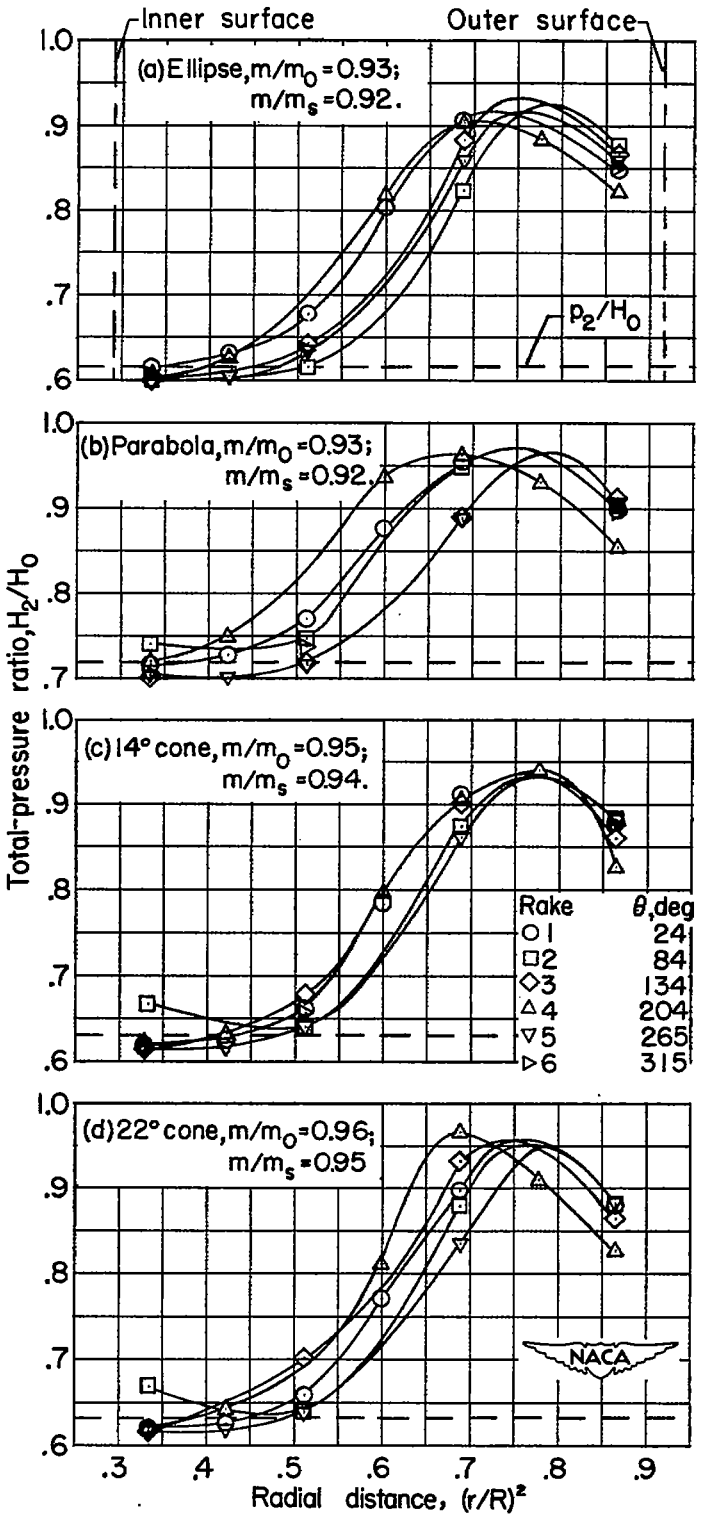

Figure 31.- Variation of total-pressure ratio with radial distance. $M_0 \approx 1.10$; $\alpha = 0°$.

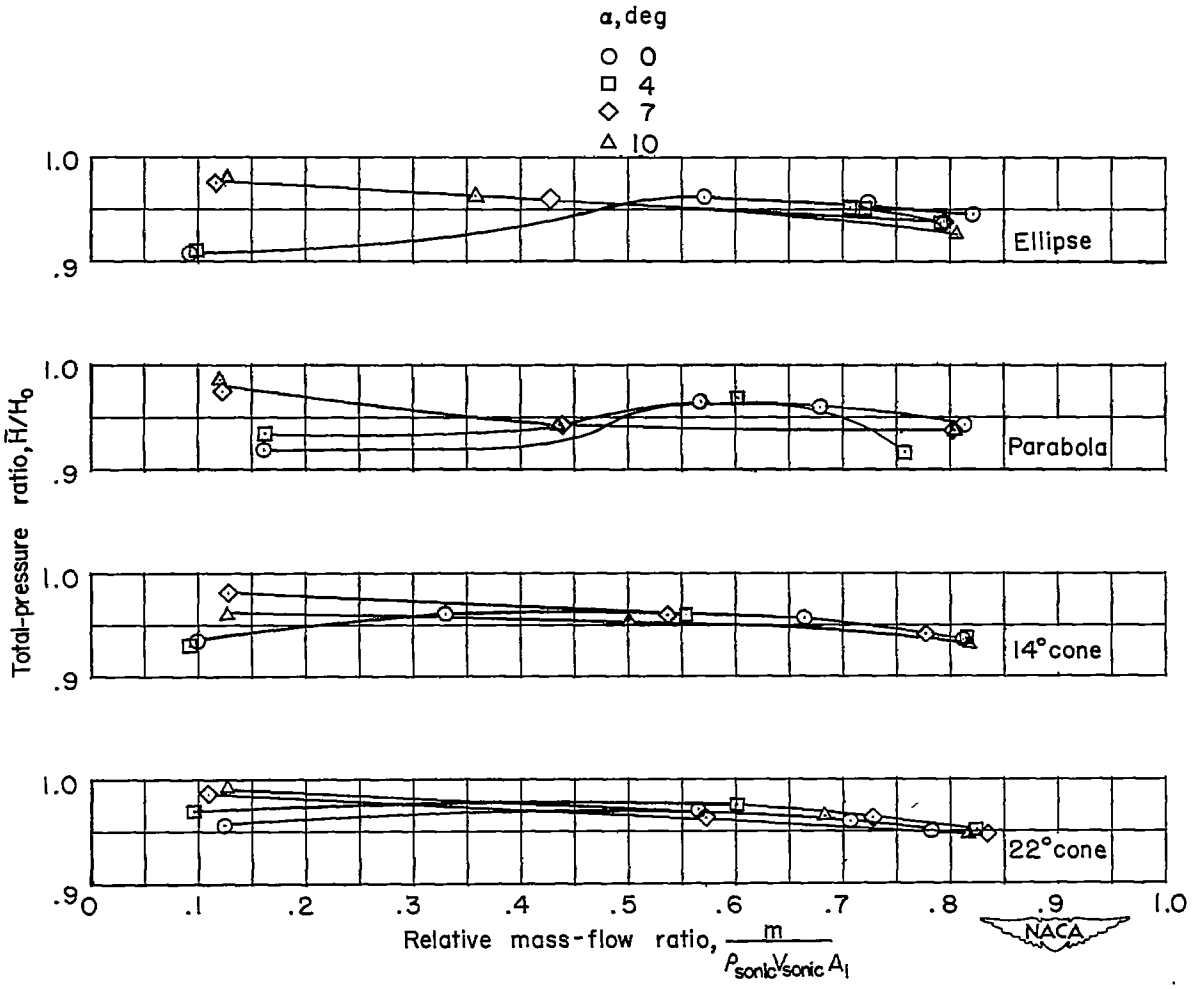

(a) $M_o \approx 0.60$.

Figure 32.- Effect of angle of attack on total-pressure ratio.

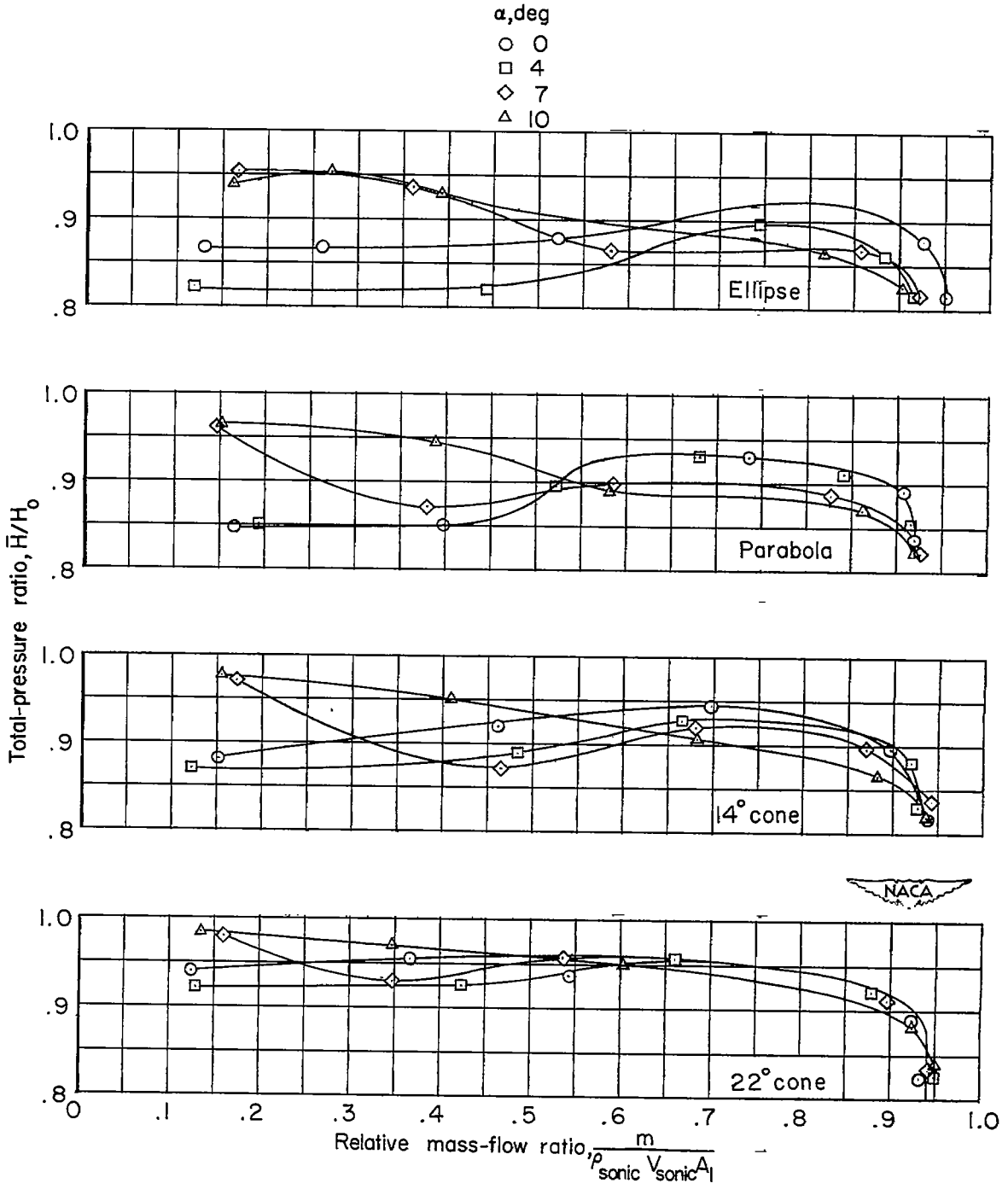

(b) $M_0 \approx 1.0$.

Figure 32.- Continued.

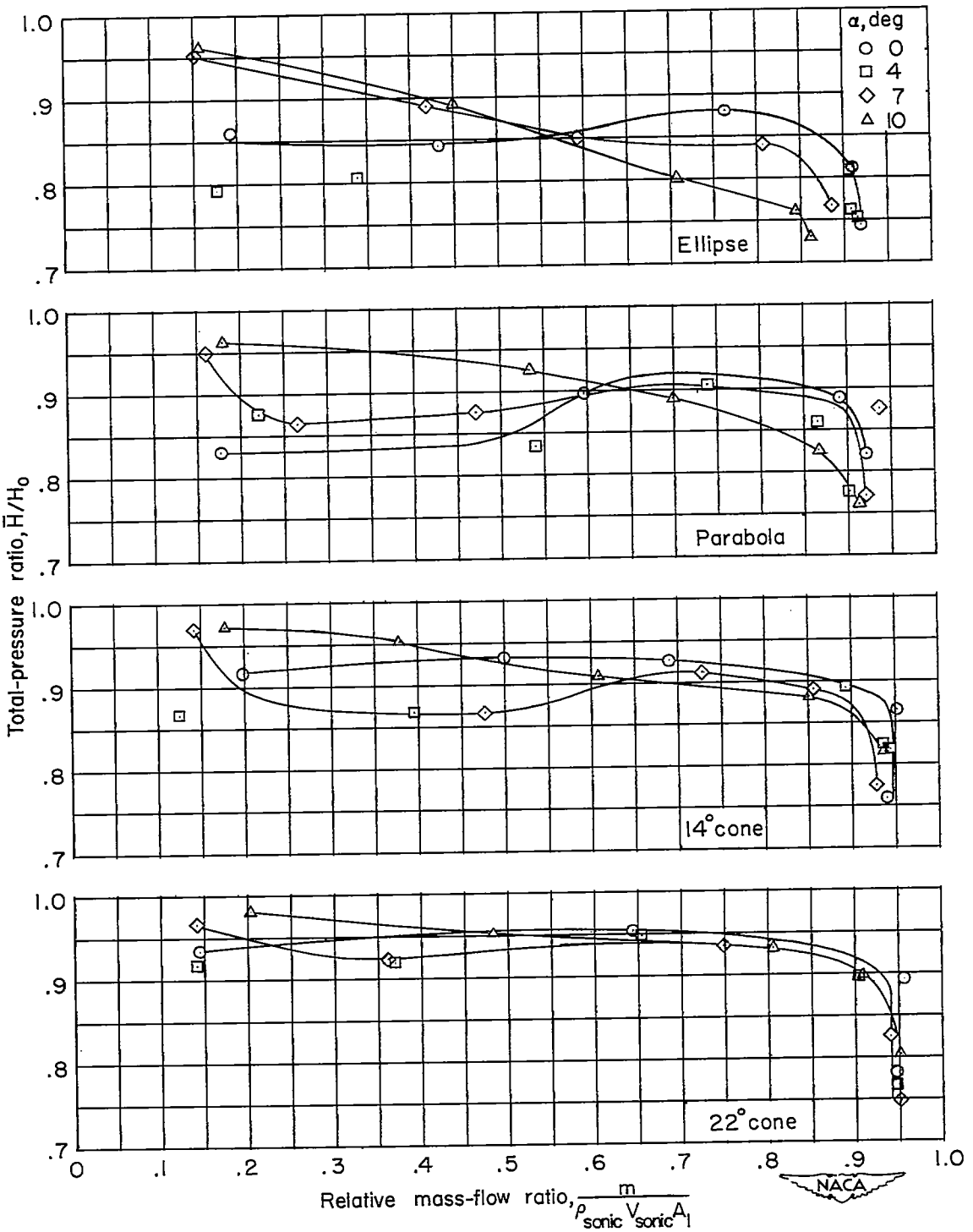

(c) $M_0 \approx 1.10$.

Figure 32.- Concluded.

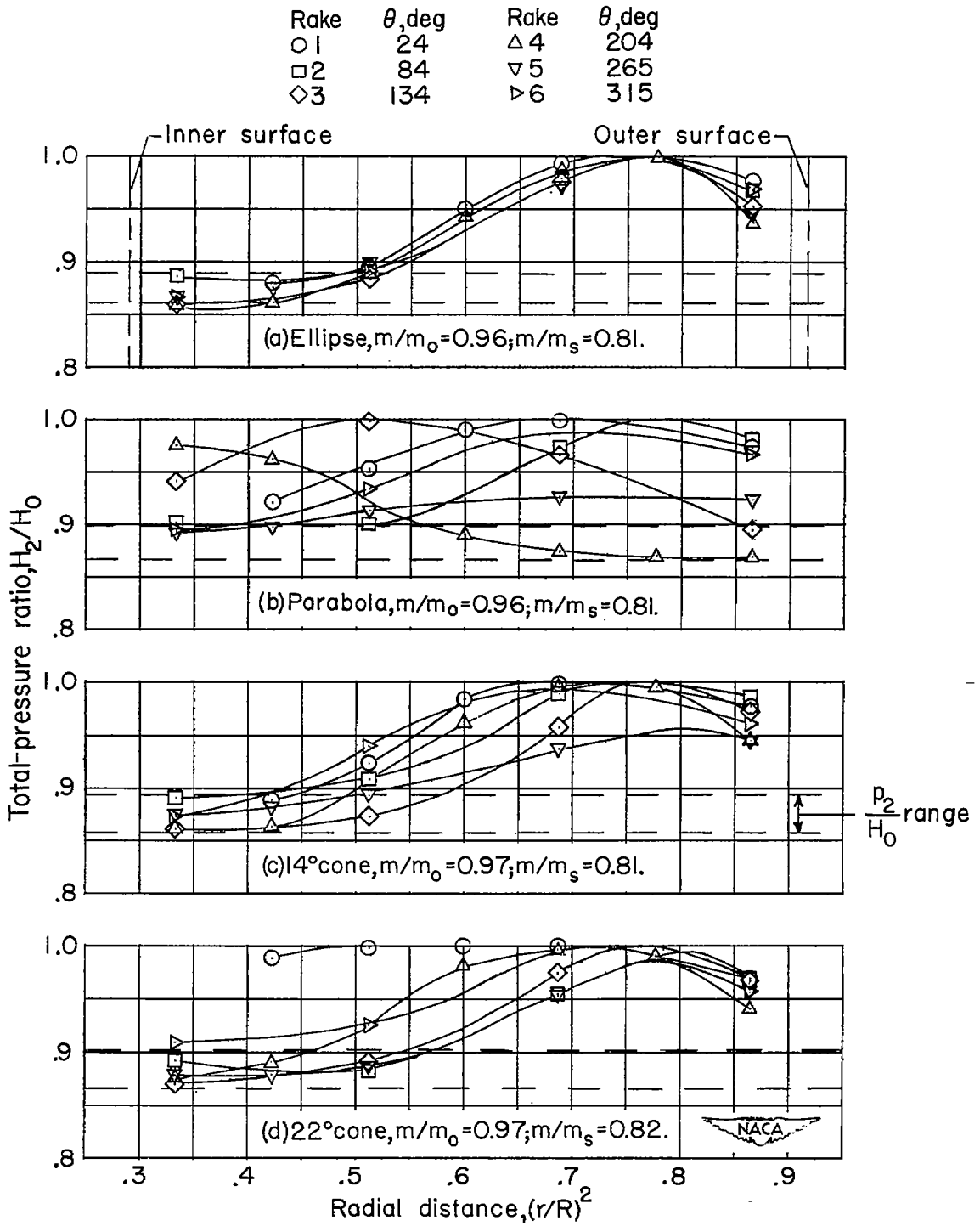

Figure 33.- Variation of total-pressure ratio with radial distance. $M_0 \approx 0.60$; $\alpha = 10°$; high mass-flow ratio.

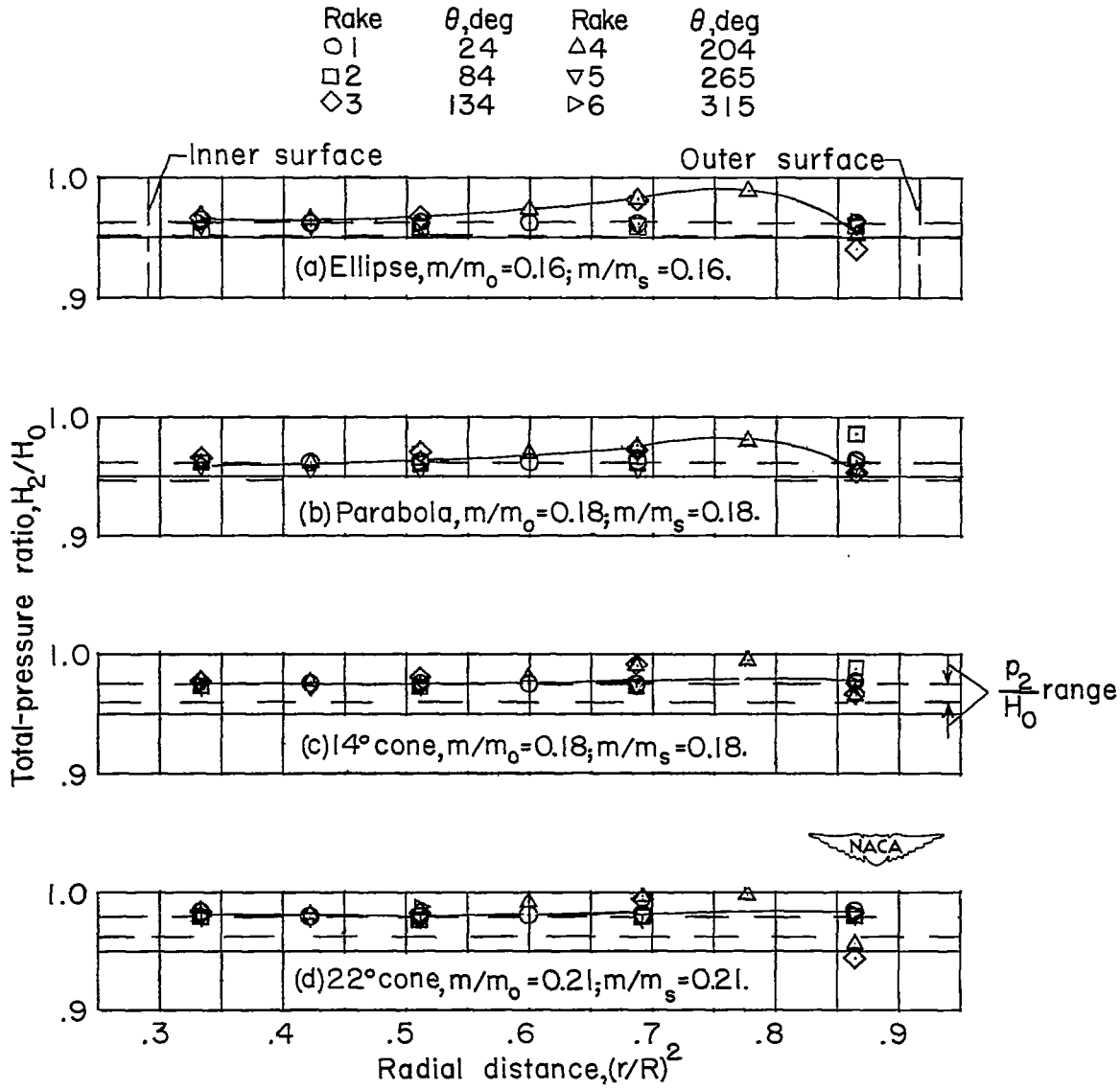

Figure 34.- Variation of total-pressure ratio with radial distance. $M_0 \approx 1.10$; $\alpha = 10^\circ$; low mass-flow ratio.

[redacted]

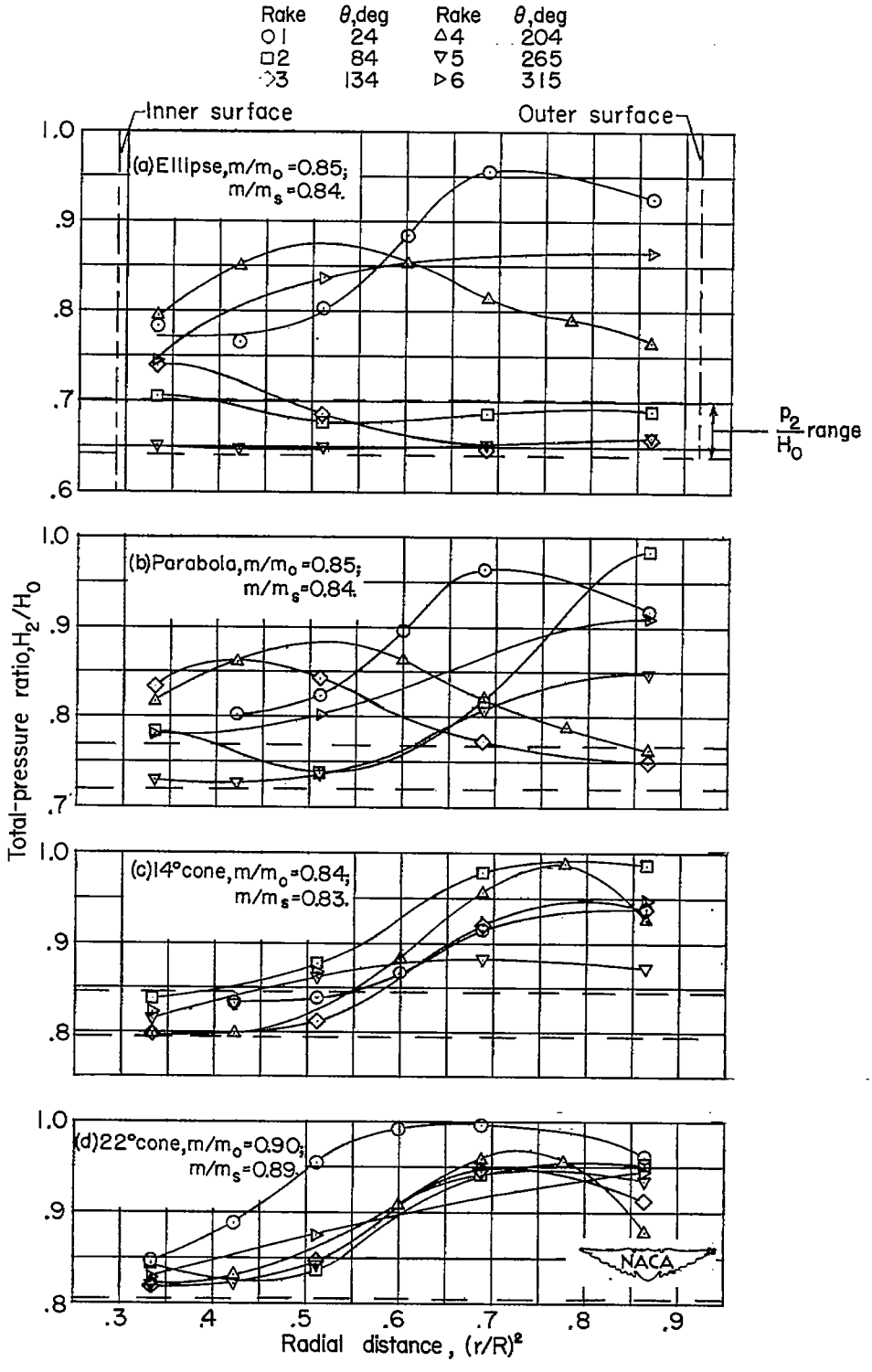

Figure 35.- Variation of total-pressure ratio with radial distance. $M_o \approx 1.10$; $\alpha = 10^\circ$; medium mass-flow ratio.

NACA-Langley - 8-19-53 - 325